Pulsed Laser Deposition of Eu-doped Multilayer Thin Films for Spectral Storage Applications

---

A Dissertation

Submitted

to the Temple University Graduate Board

---

in Partial Fulfillment

of the Requirements for the Degree of

Doctor of Philosophy

By

Francisco J. Bezares

January, 2009

ABSTRACT

Pulsed Laser Deposition of Eu-doped Multilayer Thin Films for Spectral Storage Applications

Francisco J. Bezares

Doctor of Philosophy

Temple University, 2010

Advisor: Dr. Zameer Hasan

This thesis studies different Eu optical centers in MgS:Eu and CaS:Eu thin films produced by Chemically Controlled Pulse Laser Deposition (CCPLD) and evaluates their suitability for the development of spectral storage devices of the future. The produced thin films consist of one or more optically active layer(s), MgS:Eu, CaS:Eu or a similar material, and a corresponding ZnS capping layer that functions as a protecting barrier for the other layers and preserves their composition and integrity. Given that the synthesis of the materials used to produce the multilayer structures in this work proved a great challenge, careful attention was given to the optimization of all fabrication parameters. Mass Spectrometry was used during the deposition of the thin films and the data obtained resulted on improvements and optimization of the deposition process. Scanning electron microscopy studies of these thin films were conducted to study degradation upon long-term

storage. Microscopy results show that the morphology of the produced thin films is correlated to the growth environment during deposition and deterioration of the deposited materials could be initiated by nano-gaps and cracks in the capping layer of the thin films.

In addition to optical centers in MgS:Eu and CaS:Eu, new centers were created by changing the thin film growth environment inside a hi-vacuum chamber, modifying the composition of the ablation target material, or both. For example, introducing O^{2-}, or alternatively HCl, inside the CCPLD chamber while producing MgS:Eu thin films results in the formation of impurity associated centers across lattice sites throughout the deposited structures. In another method of impurity doping studied, Cl^{-} and Na^{+} were introduced into the MgS:Eu and CaS:Eu lattices by mixing trace amounts of the impurity ions into these materials in polycrystalline form and making this mixture a deposition target by hi-pressure cold compression technique. The introduction of these impurity ions will alter the crystal field environment around the Eu ions thus creating new optical centers with a shift in energy of their characteristic Zero Phonon Line. After extensive characterization of the optical properties of the thin films produced, laser-induced fluorescence spectroscopy and absorption spectroscopy measurements confirm that they are suitable candidates to be used in conjunction with power-gated spectral holeburning technique and could potentially provide ultrahigh, terabits per square inch, storage densities.

ACKNOWLEDGEMENTS

I consider myself extremely lucky to have counted with the help and support from many individuals throughout my graduate endeavor at Temple University. Professors, technicians, administrative staff and fellow graduate students where always friendly and willing to offer their time and expertise when needed. I learned a great deal from them and will always be very grateful.

Firstly, I have to thank my advisor, Dr. Zameer Hasan, for his attentive mentoring and his guidance throughout the research portion of my graduate studies. He was always in the best disposition to offer advice and always went out of his way to make himself available for help, even when his schedule was not the most flexible. I truly appreciate his support.

Dr. Theodore Burkhardt, Dr. C. J. Martoff, Dr. Peter Riseborough as well as the rest of the professors who taught the required academic courses for the Ph.D. Program where instrumental in the completion of my degree. They very effectively helped me focus on academic weaknesses and helped develop my academic problem solving skills and critical thinking. They really made a difference.

Janis Zambrano and the rest of the administrative staff's assistance could not be overstated. Janis could not have been more helpful to me and always offer valuable advice with administrative actions and procedures. Evelyn's friendly attitude

could not have been more welcoming and approachable. I also have to mention the electronic and machine shop technicians, Richard Harris, William Stevenson, Ed Kazanovic and David Plasket for the technical support and advice in numerous occasions throughout my dissertation investigation.

Adam Adamzcic and Zhengle Qiu where always great fellow gradute students to work with in the lab. Undergraduate students Mike Campanell and Goral Patel helped me with some of the experiments conducted in support of this thesis. They where both very smart, independent and it was a pleasure for me to work with them as well. Thank you.

Michael Dion was always a good friend and I valued his good nature as well as his occasional personal advise very much. I thoroughly enjoyed our routine conversations and extracurricular activities. You can always count me as a friend, Mike.

I would also like to thank Joe Palma. His new approaches to coursework requirements and problem solving was always very insightful. His good humor and technical skills made working with him in the lab a very pleasant experience and his consistent disposition to join me for an occasional musical "jamming" session was priceless. Keep rocking Joe!

I am also very grateful to Chris Tillingast and Fred McCullough. Their efforts resulted in the donation of a Scanning Electron Microscope from Yale University's Electrical Engineering Department to our group. The instrument is today oprational and could be used for future studies conducted at Temple University. Fred McCullough's technical advice has always come in handy and very timely. As usual, thank you, Fred.

I cannot overstate how grateful I am to Dr. Johnattan Spanier and Ms. Jen-

nifer Atchison from Drexel University. Dr. Spanier very kindly and selflessly put his laboratory's scanning electron microscopy at my disposal allowing me to complete electron microscopy studies on some of the samples made during this work. Ms. Atchison unconditionally offered her scanning electron microscopy operation expertise to ensure that the best quality images where obtained for my samples. I hope they realize how significant to me and my work their help was and I hope that someday I get the chance to humbly return the favor.

And last but not least, to all my friends and family, thank you as well. Your support was always there and it always made me feel a very lucky person. I hope you all know how much that meant to me!

DEDICATION

To my mother and father.

TABLE OF CONTENTS

LIST OF FIGURES

LIST OF TABLES

CHAPTER 1

INTRODUCTION

Persistent Spectral Holeburning (PSHB) is a very powerful technique that not only can be used for obtaining valuable spectroscopical information about the local environment around optical centers in a solid-state lattice [1] but it also has inspired scientists to envision a wide range of application schemes that span a broad spectrum of many different scientific research areas. It comes to no surprise that it has been extensively studied by researchers all over the world for more than 30 years. In fact, many applications for PSHB with great potential for ground-breaking developments in optical storage, pulse shaping, optical signal processing and solid-state quantum information processing have been proposed as fruits of those efforts [2, 3, 4]. Although many of these schemes have presented very strong cases for the development of new technologies, only a few have been demonstrated in the laboratory as successfully as PSHB for frequency domain optical storage (FDOS) [5]. In this technique, optical information can be stored into and read from a solid-state material by burning holes into its optical spectrum. This is accomplished by exploiting the fact that the optical spectrum of certain solids

at low temperature, doped with an optically active ion, will generally show an inhomogeneously broadened Zero-Phonon Line (ZPL). The inhomogeneous broadening (Γ_{ih}) of this spectral feature reflects variations of the crystal field parameters around the optically active ion. That is, variations of the crystal field environment around the optically active ions will shift the energy level splittings throughout a grand ensemble of these ions in the solid usually resulting in the broadening of what would otherwise be a narrow homogeneously broadened (Γ_h) spectral line, see figure 1.1. These variations are usually caused by strains inherent to all crystals due to chemical impurities and other point defects in the lattice. Spectral holes can be burned independently on the optically active ions by photo-exciting them with narrow bandwidth laser light, thereby changing their optical properties. By selectively photo-exciting smaller ensembles of ions, spectral holes can be burned throughout the extension of the spectrum of an inhomogeneously broadened ZPL. The hole is a direct result of the reduction of absorbing optical centers at a particular frequency and appear as dips, or inverted peaks, in the optical spectrum of the material. The hole width will greatly depend on the bandwidth and intensity of the exciting laser beam as well as some other factors like temperature and oscillator strength of the optical center [6].

In PSHB, spectral holes can be modified for time periods longer than the lifetime of any excited state. This is due to the fact that in this process the photoionization of the the optical center is followed by the delocalization and subsequent capture of the excited electron by an electron vacancy in the lattice, or deep trap, within the energy gap of the material. This process permanently changes the optical spectrum of the solid. In FDOS, spectral holes are burned at a particular spacial and spectral location in a solid with the purpose of encoding

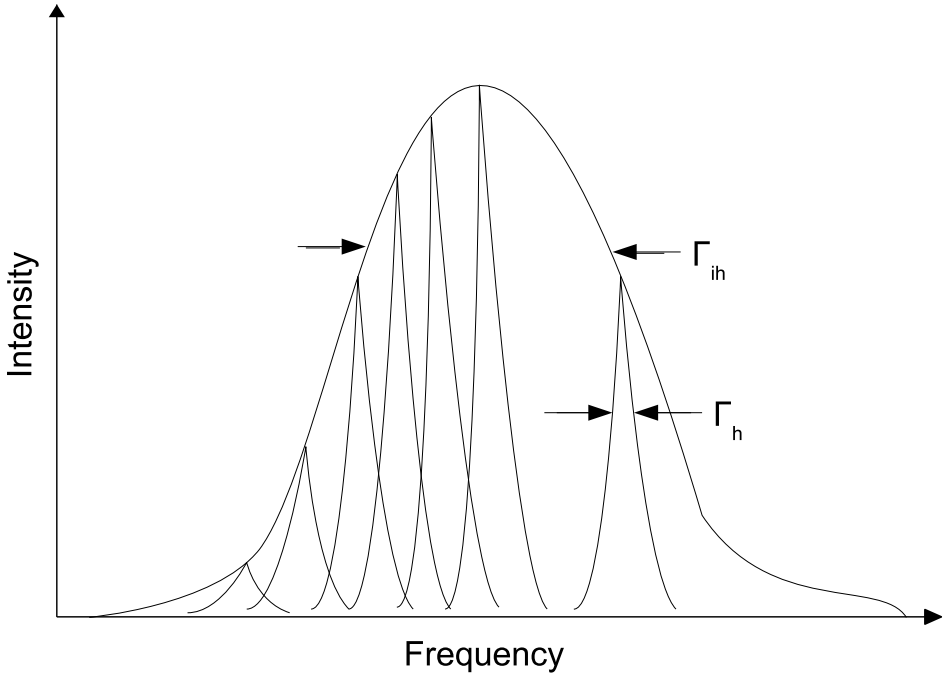

Figure 1.1: Inhomogeneously broadened ZPL diagram. The homogeneous linewidth Γ_h is smaller than the inhomogeneously broadened linewidth Γ_{ih} of the ZPL.

optical information. For example, the presence of a hole can be arbitrarily chosen to encode a digital 1 and its absence a 0. Figure 1.2 represents this encoding on the optical spectrum of a material for which spectral holes have been burned. Given that the optical information is stored on the frequency domain of the material, many bits can be stored into a volume determined by the dimensions of the writing laser spot therefore producing storage densities significantly higher than those for conventional optical and magnetic storage. The improvements of information storage capacities of these systems can be determined quantitatively by considering the width ratio between Γ_h and Γ_{ih} [7]. At liquid helium temperatures, where the broadening due to phonons and other excitations is minimized, Γ_h can become very close to the width of the optical transition itself. This width can generally be of the order of 1kHz - 100MHz for transitions in centers with weak electron-phonon coupling. Γ_{ih}, on the other hand, can have widths ranging from 0.1 - 10,000GHz for the same type of systems. Therefore, in theory, 10^7 - 10^8 spectral holes could be burned in a single inhomogeneously broadened ZPL line. Moreover, thousands of holes can be burned into the volume of a medium enclosed by a focused laser spot ($\approx 1\mu$m) thereby making storage capacities of terabits per square inch possible.

One of the most remarkable achievements in ultra-high density PSHB storage in recent years was reported by Hasan *et al* [8]. In those experiments, several hundreds of completely photo-erasable spectral holes were burned into a solid-state system, with no detectable erasure after several thousands of reading cycles and a thermal cycling temperature of up to 150K. Hasan's research group was able to obtain this results by doping low concentrations of Eu (0.01% mol) into MgS and CaS lattices in polycrystalline and thin film form to obtain ZPLs in the optical spectrum of these materials that were very suitable for PSHB-based FDOS.

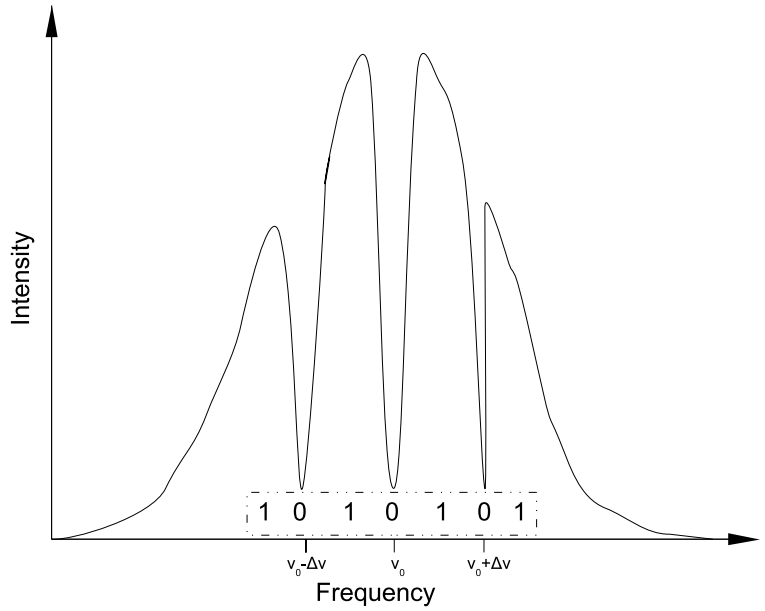

Figure 1.2: Holeburning digital encoding conceptual diagram. The spectral holes burned on a material can be used to encode optical information by assigning a binary value to the hole and no-hole states found at different frequencies.

The $4f^7$-$4f^6 5d$ transition of the Eu^{2+} ion in MgS and CaS lattices results in a inhomogeneously broadened ZPL ($\approx 6Thz$ wide) that lies approximately at $\lambda =$ 578nm and $\lambda = 625$nm for MgS:Eu and CaS:Eu, respectively. Further work by members of the group showed that adding oxygen impurities to a thin film lattice of MgS:Eu will shift the position of the ZPL to approximately $\lambda = 588$nm. They also showed that the changes in photo-luminescence intensity of the respective ZPLs were gradual. That is, the intensity of the Eu center will decrease and at the same time the intensity of the oxygen-associated Eu center will increase with increasing the oxygen impurities concentration while producing the thin films[9]. This is an important finding because it suggests the possibility of further creating additional new optical centers by simply slightly varying the crystal field environment around the Eu centers through the introduction of new dopants at specific concentrations. For example, introducing Cl^- or O^{2-} ions into the MgS:Eu lattice will result in variations of the crystal field parameters surrounding the Eu ion, see figure 1.3. The difference in size of the Cl^- or O^{2-} ions compared to the S^{2-}'s and, in the case of Cl^- its difference in charge, will cause the energy field distribution around the Eu^{2+} ion to change. This will, in turn, change the energy level splitting of the Eu^{2+} ion and therefore change the position of the electronic transitions in its emission spectrum. In the case of O^{2-}, the charge number remains unchanged and charge compensation considerations become negligible. For this reason, there might be a tendency for the O^{2-} ions to go into mainly substitutional sites within the MgS:Eu lattice. Cl^-, on the other hand, differs from S^{2-} in both charge and size. Therefore its effect on the crystal field parameters of MgS:Eu can be expected to be larger than O^{2-}'s at the same concentration. Given the similar nature of the MgS:Eu lattice structure to the structure of CaS:Eu , these considerations will also

apply for the case of CaS:Eu.

Another way of significantly increasing the storage densities attainable by PSHB-based FDOS is through the design of multilayer structures. Here, the optical information is stored in multilayer thin films. By choosing an appropriate combination of layer materials, one in which the ZPLs of the materials do not overlap at a particular spectral position, it may be possible to simultaneously read the information stored separately in each material. This technique results in a n-fold increase, n being the number of layers, of the storage capacity of a particular storage device. Figure 1.4 shows an example for a three layer thin film device. The ZPL of each material layer appears away from each other and at a different position in the spectrum of the device therefore each can be easily addressed and identified. As an example, in this case there are three ZPLs to which information can be written and from which it can be read resulting in a 3-fold increase in range of available frequencies for information storage.

One key aspect on the development of such an application will be finding the right materials that can provide the optimal spectral features for maximum storage capacities, at conveniently spaced spectral ranges. The larger the number of ZPLs that can be put together into a multilayer thin film and the larger their bandwidth Γ_{ih}, the bigger the storage density increase of such thin films. Therefore, in order to uncover the full potential of this technology, it is very important that special attention is given to the development of new materials with these characteristics and which at the same time will be suitable for multilayer spectral holeburning. Unfortunately, most research efforts devoted to the study of PSHB-based FDOS in the past have been focused on solid-state systems, crystalline as well as amorphous, with only a single type of optical center.

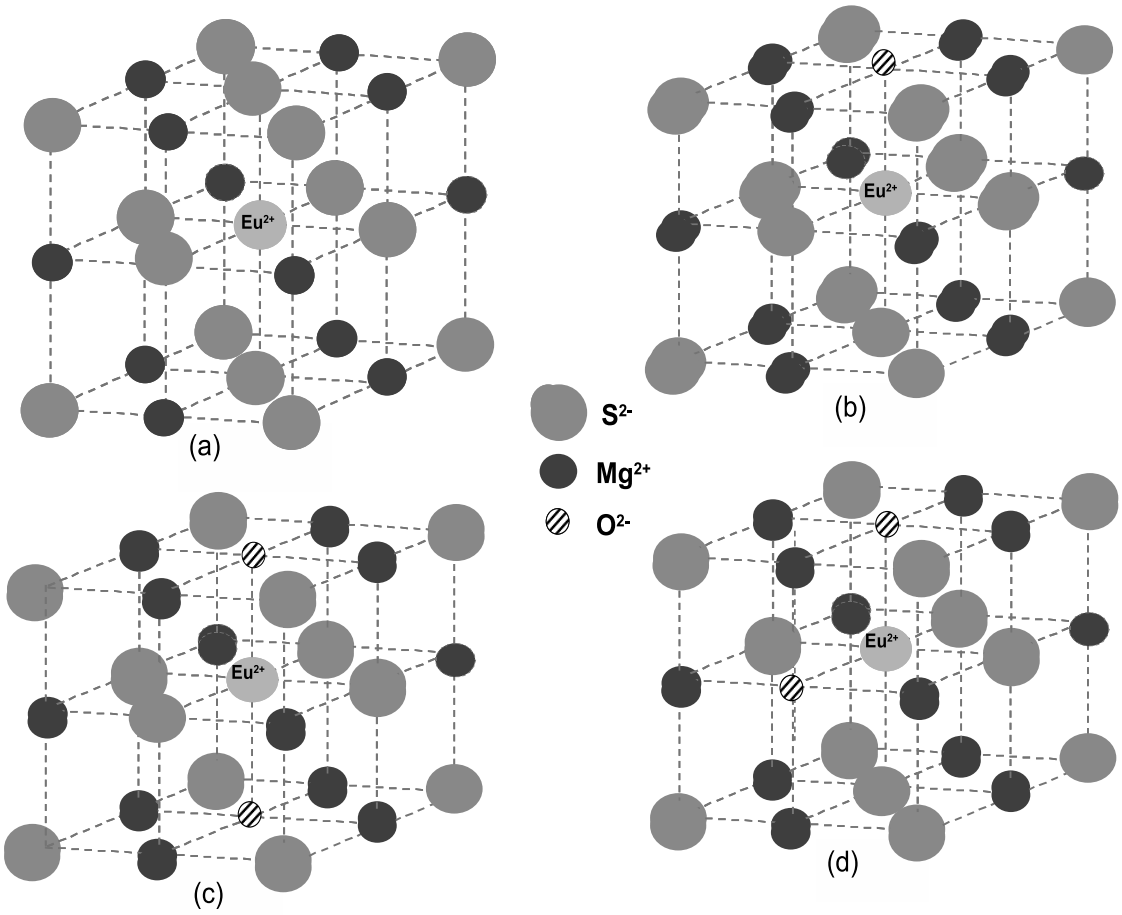

Figure 1.3: O^{2-} impurities in the MgS:Eu^{2+} lattice. The O^{2-} ion can go into S^{2-} substitutional sites in different combinations. Its location in the lattice and its size will change the crystal field environment surrounding the Eu^{2+} ion.

The purpose of this study was to look for new wide bandgap materials for increasing the optical information storage capacity of multilayer PSHB-based FDOS thin film devices. Particular focus was put into introducing new species into MgS:Eu and CaS:Eu thin films in an attempt to shift the Eu^{2+} transition energies inside the materials such that the new positions of their respective ZPLs can increase the available spectral range for PSHB. The following chapters of this thesis present a systematic study that encompasses the synthesis of new PSHB-capable materials, their production in the form of thin films and finally their optical and morphological characterization.

Chapter 2 covers some general theoretical considerations regarding the optical characteristics of PSHB materials. It outlines the optical spectrum features that make these systems suitable for holeburning and discusses some of the physical mechanisms that give them their exotic optical properties. For example, some important mathematical relationships will be presented in order to establish a link between the optical properties of the Eu^{2+} ion and its interaction with the crystal field matrix. Chapter 3 presents all aspects of the experimental techniques and methods followed in this study. It covers all steps of the experiments conducted, starting from the synthesis of the materials all the way up to the characterization of the optical properties of the thin films studied. In Chapters 4, 5, and 6 the experimental data and results are presented and discussed in detail. It outlines Laser-Induced Fluorescence and Absorption Spectroscopy results obtained from the different systems studied and establishes relationships between some of them by way of objective comparisons and detailed analysis. Chapter 7 focuses on the morphological studies performed on some of the thin films made for this work. It presents Scanning Electron Microscope (SEM) images of various thin films and

discusses some of the relationships between morphology and optical properties. Finally, Chapter 8 presents some conclusive remarks concerning the results of the experimental work conducted throughout this study and discusses some of the possible ways in which they can have some important significance in future development of PSHB-based FDOS technology.

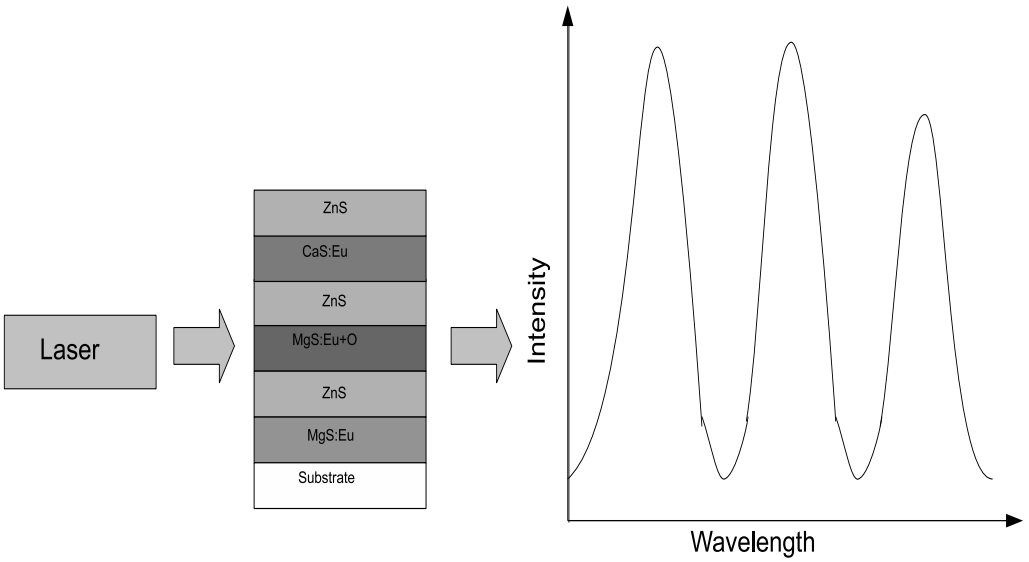

Figure 1.4: Multilayer FDOS diagram. The material of each layer can have a ZPL lying some spectral distance away from the others. The spectral storage capacity can be significantly increased this way.

CHAPTER 2

THEORETICAL BACKGROUND

2.1 Introduction

Before getting into a more detailed description of certain specific aspects to be discussed in further chapters it might be beneficial to make note of some important theoretical considerations about this investigation. This chapter will assist the reader in establishing a solid foundation for the ideas further developed and will offer the reader a more complete picture of the work to be presented. The theoretical points to be treated here will be specific to the solid-state systems under study, namely MgS:Eu and CaS:Eu, but will at the same time be developed in general without pursuing rigorous proof and/or derivation of the formulas presented. More detailed discussions of these aspects have been presented elsewhere and respective references to those studies will be offered as it becomes relevant.

It might be also worth noting before moving on that figure 1.3 on the previous

chapter used a crystalline structure model of the materials studied to describe some of the phenomena and characteristics exhibited by them when interacting with light. This chapter will use a similar approach as a starting point in further theoretical descriptions of these systems as well. This, however, shall not be taken by the reader as a statement of pure crystallinity of our materials. In fact, the thin films produced during this study can be categorized as amorphous solid-state systems. The simplest way to describe the structure of an amorphous material like the ones under study consists of considering that short-range coordination is preserved while the long-range atomic arrangement is random. That is, the values of the first nearest neighbor distance, coordination number, or binding energy remain more or less the same in the amorphous and crystalline phase. Although simplifications of the *Bloch Theorem* and the concept of wave vector $\mathbf{k}$ as a good quantum number in amorphous materials are not valid, the electronic density of states $N(E)$ and the imaginary part of the dielectric function ε still remain well defined quantities.

2.2 The Eu ion in the MgS and CaS Lattice

The Eu ion can be found inside solid-state lattices either as Eu^{2+} or Eu^{3+}. That means that their corresponding ground state configuration is $4f^7$ and $4f^6$, respectively. Due mainly to the screening effect of the $5s^2$ and $5p^6$ orbital electrons, the excited state $4f-4f$ transition of the Eu^{3+} ion remains largely unaltered by crystal field interactions and therefore its energy level splitting doesn't change much from one host to another. This $4f-4f$ transition is also forbidden under parity selection rules and as a result, its spectral line is usually very sharp. This

characteristic renders such transition rather impractical for spectral storage applications. The excited state $4f - 5d$ transition of the Eu^{2+} ion, on the other hand, is usually broad and strong. It is also parity allowed therefore has a higher oscillator strength. And although the ${}^8S_{\frac{7}{2}}$ ground state remains screened by the outer shell electrons, and consequently relatively unchanged, the excited $5d$ state interacts strongly with the crystal matrix and easily varies in energy in response to slight variations of the crystal field parameters [10]. These are the characteristics that create the broadening of the ZPL in the optical spectrum of MgS:Eu and CaS:Eu and make them very good candidates for spectral storage. For this reason, this chapter (and the rest of the thesis, for that matter) will only focus on the behavior of the Eu^{2+} ion in the MgS and CaS lattice and will only discuss Eu^{3+} ion effects when relevant to this purpose.

The energy level structure of a Eu^{2+} ion inside a MgS or CaS lattice is not only determined by the Hamiltonian of the free ion but also by its interaction with the crystal field environment around the ion [11]. Although other Hamiltonian terms arising from additional interactions could be present, they are of significantly smaller magnitude than the effects created by the free-ion, spin-orbit and crystal field and can be neglected during general purpose calculations. For example, the hyperfine, super-hyperfine and nuclear quadrapole interactions on the Eu^{2+} ion in a solid-state lattice are much smaller than the crystal field and spin-orbit interactions therefore do not affect much the energy level splittings of the ion. However, this is not true for the Eu^{3+} ion, given that its energy level splitting is very small, and therefore additional terms of the Hamiltonian cannot be neglected. The Hamiltonian for the case of the Eu^{2+} ion can then be described

by the equation [12, 13] ,

$$\mathcal{H} = \mathcal{H}_0 + \mathcal{H}_C + \mathcal{H}_{SO} + \mathcal{H}_{CF} \tag{2.1}$$

where

$$\mathcal{H}_0 = -\sum_i \frac{\hbar^2}{2m}\nabla_i^2 - \sum_i \frac{Ze^2}{r_i} \tag{2.2}$$

$$\mathcal{H}_C = \sum_{i<j} \frac{e^2}{r_{ij}} \tag{2.3}$$

$$\mathcal{H}_{SO} = \sum_i \xi(r_i)\boldsymbol{l}_i \cdot \mathbf{S}_i \tag{2.4}$$

$$\mathcal{H}_{CF} = \sum_{k,q,i} B_q^k C_q^{(k)}(i) \tag{2.5}$$

In Eq. 2.2, the first and second term are the electron kinetic and potential energy, respectively, in the field of the nucleus. This field is radial, therefore the energy shifts for all levels belonging to a configuration will be the same and will not affect the level structure of a configuration. The $\mathcal{H}_C$ term (Eq. 2.3) represents the inter-electron Coulomb repulsion between any two electrons at a distance r_{ij} and $\mathcal{H}_{SO}$ (Eq. 2.4) represents the spin-orbit coupling interactions due to the magnetic dipole-dipole moments of spin and angular momentum of the electron with spin-orbit constant $\xi(r_i)$. The last term ($\mathcal{H}_{CF}$) in Eq. 2.1 describes the optical center's interaction with the crystal field environment surrounding it. The B_q^ks are crystal field parameters that can be determined experimentally and the $C_q^{(k)}(i)$s are components of the tensor operator $\mathbf{C}^{(k)}$ that transforms like spherical harmonics. It is important to notice that the only part of the above Hamiltonian that will differ for MgS:$Eu^{2+}$when compared to CaS:Eu^{2+} is the crystal field interaction

term. The size difference between the Mg and Ca ions, and therefore the symmetry variations of the lattice, will result in variations of the crystal field parameters and consequently the energy level splittings of the optical centers.

It is important to note, however, that the Hamiltonian in Eq. 2.1 refers to situations where concentrations of the Eu^{2+} ion is small and inter-ion interactions do not become significant, *i.e.* 0.01-1% molar. Previous members of our group used Mössbauer spectroscopy and nuclear forward scattering techniques in an effort to determine the ratio of concentration between the Eu^{2+} and Eu^{3+} in samples prepared similarly to the ones prepared for this investigation [14]. They showed that although the ratio of concentration slightly varied from sample to sample, it is possible to produce samples with concentrations varying from 0% to relatively high concentrations.

One of the main goals of this work was to introduce doping species into the MgS:Eu and CaS:Eu lattice to study the effects this would have on the energy level structure of the Eu^{2+} ion. By introducing additional or substitutional species of different size and/or charge inside the lattice will result in slight variations of the crystal field surrounding the Eu^{2+} ion thereby shifting the position of the ZPL on the optical spectrum of the system.

2.3 Optical Spectrum and Electron-Phonon Interactions

In terms of spectral storage, the key feature in the optical spectrum of MgS:Eu and CaS:Eu is the ZPL. It is mostly there where PSHB is attained. In both cases, however, the intensity and bandwidth of the ZPL are closely related to the intensity and bandwidth of the vibronic spectral feature of their spectrum. In fact, the temperature dependance of their optical spectrum results in the transfer of integrated intensity from the Purely Electronic Line (PEL) to the phonon sideband.

To see this more clearly, let us consider the electronic transitions due to the creation and annihilation of phonons for an impurity center in the absence of local vibrations. Because the range of acoustic phonon frequencies begins from zero, the energy spectrum of the transitions will usually be broad and continuous. At $T = 0$, the PEL linewidth $\Gamma(0)$ will be determined by the electronic excited state decay time $T_1(0)$. That is,

$$\Gamma(0) = \frac{1}{2\pi c T_1(0)} \ (cm^{-1}) \tag{2.6}$$

The impurity center lies inside the significantly larger mass of the rest of the solid therefore there will not be an observable effect of *Doppler Broadening*. This shows that in theory, for allowed optical transitions $T_1(0)$ will be of the order of $10^{-7} - 10^{-8}$s giving a $\Gamma(0)$ value of approximately $10^{-4} - 10^{-3}\ cm^{-1}$, respectively. Even narrower values will be obtained for forbidden transitions.

At $T \neq 0$, thermal excitation-induced dephasing processes cause broadening of

the PEL. This processes, caused by electron-phonon interactions, can be regarded as quasi-elastic scattering between the phonon and the impurity [15]. For this reason, the phonon's direction of propagation can change during the scattering event while its change in energy remains small or equal to zero. Nevertheless, the phase of the electronic excited state wavefunction will experience significant changes. The electron will remain in the excited state but its wavefunction's time dependent part will change from $\exp\left(\frac{iE_e t}{\hbar}\right)$ to $\exp\left(\frac{iE_e t}{\hbar} + \delta\right)$, where E_e is the electronic energy level and δ is a random phase shift. In other words, the electronic excited state lifetime will shorten resulting in a new homogeneous linewidth that will be broader than the value obtained for the case with $T = 0$ above. When dealing with a grand ensemble of impurity ions, this will mean that the coherence time of the ensemble of excited state impurities will shorten as well. Consequently, PELs will experience temperature broadening due to increases in the density of thermal phonons as temperature increases. This will give a homogeneous linewidth that can be written as,

$$\Gamma(T) = \frac{1}{\pi c T_2(T)} = \frac{1}{\pi c}\left(\frac{1}{2T_1(T)} + \frac{1}{T_2^*(T)}\right) \ (cm^{-1}) \tag{2.7}$$

where T_1 and T_2^* are the energy relaxation and the phase relaxation times, respectively. It is important to note here that $\frac{1}{T_1} = \frac{1}{T_{1opt}} + \frac{1}{T_{1q}}$, where $\frac{1}{T_{1opt}}$ is related to the purely radiative decay and $\frac{1}{T_{1q}}$ is related to the non-radiative decay. T_{1q} and T_2^* depend strongly on temperature while T_{1opt} temperature dependance can usually be neglected. For this reason, the contribution of dephasing to the PELs linewidth increases significantly with temperature.

The vibronic band feature of the MgS:Eu and CaS:Eu optical spectrum, or

phonon sidebands, corresponds to transitions in which phonons are created and annihilated and depends on the local lattice dynamics at the impurity site, the local phonon density of states as well as the strength of the electron-phonon coupling.

In order to determine the predominant behavior of the spectral features it is necessary to begin by looking at the quantum mechanical formalism for electronic and lattice interactions. The probability of a transition from the electronic-vibrational state a, n to the electronic-vibrational state b, m is proportional to the square of the matrix element

$$\langle \psi_b(\mathbf{r}_i, q)\chi_b(m)|\mu|\psi_a(\mathbf{r}_i, q)\chi_a(n)\rangle \tag{2.8}$$

where ψ is an electronic state wavefunction, χ is a harmonic oscillator function and μ is the electric dipole operator, see Figure 2.1. Using the *Condon Approximation*, we can substitute the variables q in the above formula for an average value q_0 in the electronic wavefunctions [13]. Note that at very low temperatures the harmonic oscillator function $\chi_a(0)$ has a maximum amplitude at $q = q_0$. This reduces 2.8 to

$$\langle \psi_b(\mathbf{r}_i, q_0^a)|\mu|\psi_a(\mathbf{r}_i, q_0^a)\rangle\langle \chi_b(m)|\chi_a(n)\rangle \tag{2.9}$$

The transition probability is then

$$W_{an-bm} = P_{ab}|\langle \chi_b(m)|\chi_a(n)\rangle|^2 \tag{2.10}$$

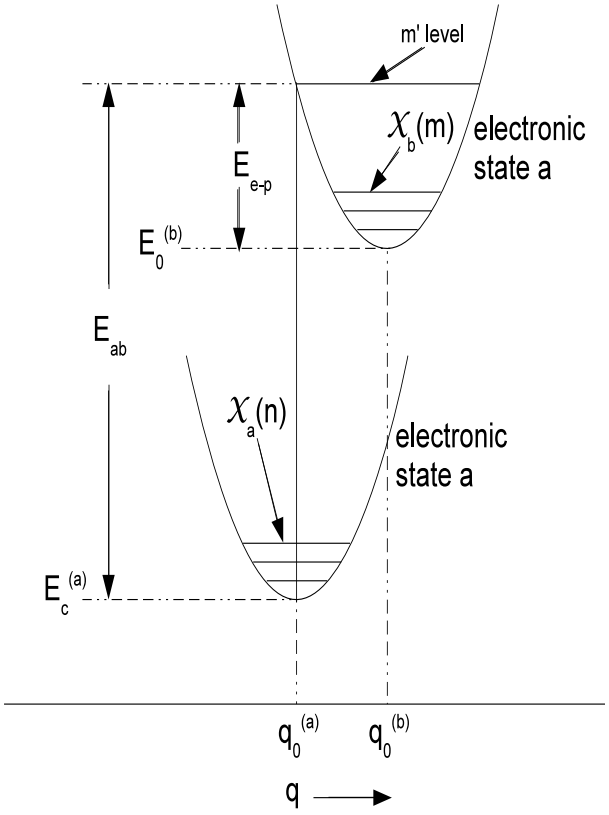

Figure 2.1: Configurational coordinate diagram. The ionic potential curve for the ground and excited states are represented by the electronic state parabolas a and b, respectively. The vibrational frequencies in states a and b are assumed to be the same and the peak of the absorption energy is represented by the length of the vertical line that goes from the bottom of the ground state to the intersection point with the excited state.

where P_{ab} is the purely electronic transition probability and is the same for all vibrational states n and m. Therefore, the vibronic band shape will be given by

$$I_{ab}(E) = I_0 A v_n \sum_m |\langle \chi_b(m)|\chi_a(n)\rangle|^2 \delta(E_{b,m} - E_{a,n} - E) \tag{2.11}$$

where Av_n represents the thermal average over the initial vibrational state n and $E_{a,n}$ is the energy of the nth vibrational state when the electronic center is in state a [17]. The graph of this expression consists of a series of delta functions at different energies separated by an interval equal to $\hbar w$. Since a lattice exhibits a wide spectrum of vibrational frequencies rather than a single breathing-mode, in practice the sideband features above the ZPL will appear as broadbands. In other words, the envelop of the individual intensities will give the predicted band shapes.

Furthermore, the overlap integral for vibrational states can be expressed in closed form as

$$\langle \chi_b(m)|\chi_a(n)\rangle = exp(-S)(n!/m!)^{\frac{1}{2}}(-\sqrt{S})^{m-n} L_n^{m-n}(S) \tag{2.12}$$

where L_n^{m-n} are associated Laguerre Polynomials with $L_0^m(x) = 1$ and

$$S = \frac{Mw}{2\hbar}(q_0^b - q_0^a)^2 \tag{2.13}$$

is the *Huang-Rhys Parameter* for an ion with oscillating mass M [18]. This parameter characterizes the difference in electron-phonon coupling between states a and b.

At T = 0, only the $n = 0$ vibrational state is occupied. This will give a

zero-temperature *Frank-Condon Factor* $F_m(0)$ of the form

$$F_m(0) = |\langle\chi_b(m)|\chi_a(0)\rangle|^2 = \frac{exp(-S)S^m}{m!} \tag{2.14}$$

The vibronic band shape will then become

$$I_{ab}(E) = I_0 \sum_m \frac{exp(-S)S^m}{m!}\delta(E_{b,m} - E_{a,0} - E) \tag{2.15}$$

$$= I_0 \sum_m \frac{exp(-S)S^m}{m!}\delta(E_0 + m\hbar w - E) \tag{2.16}$$

where $E_0 = E_{b,0} - E_{a,0}$ is the energy of the transition between the zero vibrational levels of the initial and final states; *i.e. Zero Phonon Transition.* Given that $\sum_m |\langle\chi_b(m)|\chi_a(n)\rangle|^2 = 1$, the intensity of the whole spectrum of the transitions is I_0 and is independent of the value of S and therefore independent of temperature. Since the intensity of the ZPL will be I_0exp(-S), at S = 0 all the intensity will come from the ZPL and there will be no lateral displacement of the harmonic oscillator parabola. By looking at Figure 2.1 the reader will see that in this case $q_0^a = q_0^b$, $\chi_a(n)$ and $\chi_b(m)$ will be identical sets of harmonic oscillator wavefunctions and $\langle\chi_b(m)|\chi_a(0)\rangle = \delta_{m0}$. As S increases the intensity of the ZPL decreases and vibronic sidebands begin to appear. At further increase in values of S the ZPL will start disappearing and the vibronic sideband will gain more and more intensity, see Figure 2.2.

In his 1965 publication, Thomas Keil derived an expression for the shape of the spectrum of an impurity ion's electronic transition in a solid state lattice by carrying out a thermal average over the initial vibronic states in Eqn. 2.11 [16].

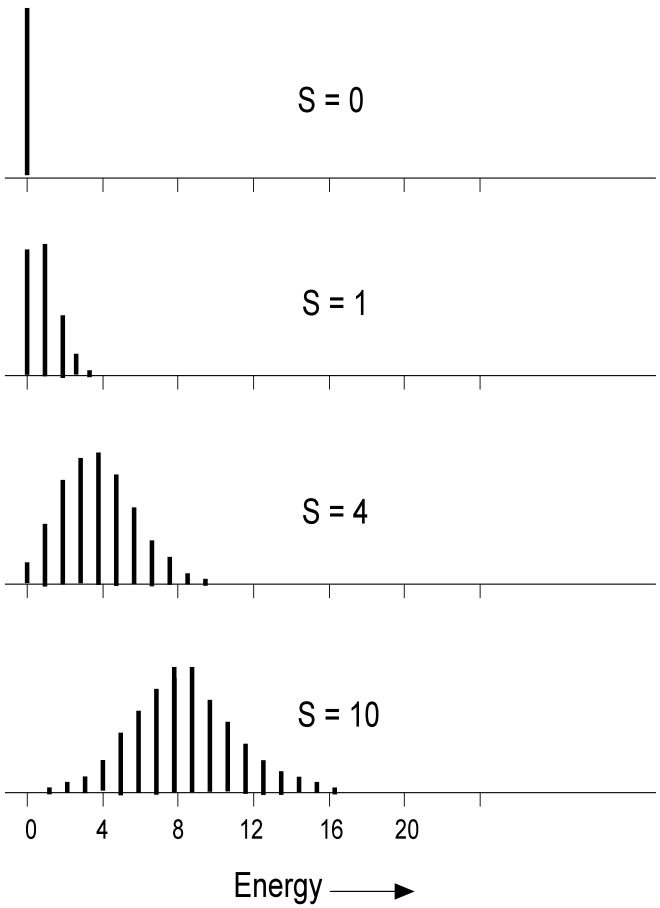

Figure 2.2: Huang-Rhys paramenter variation diagram. The bandshape of the emission spectrum of a particular system is determined by Equation 2.16 and depends on the strength of the coupling characterized by S. The envelope of the individual intensities gives the predicted bandshapes.

This expression is given by

$$I_{ab}(E) = I_0 \sum_{p=-\infty}^{\infty} exp\left(-Scoth\frac{\hbar w}{2kT} + \frac{p\hbar w}{2kT}\right) I_p\left(Scsch\frac{\hbar w}{2kT}\right) \delta(E_0 + p\hbar w - E) \tag{2.17}$$

$$= I_0 \sum_{p=-\infty}^{\infty} exp(-S(1+2n)) \left(\frac{1+n}{n}\right)^{\frac{p}{2}} I_p(2S\sqrt{n(n+1)})\delta(E_0 + p\hbar w - E) \tag{2.18}$$

where $n = [exp(\frac{\hbar w}{kT}) - 1]^{-1}$ represents the mean thermal occupancy in the vibrational mode and $I_p(z)$ is a modified Bessel function. The term $S(1+2n)$ in the exponential of Eqn. 2.18 is commonly referred to as the *Effective Huang-Rhys Parameter* at high temperatures. By carefully looking at this equation one can see that at T $>$ 0, it is possible for components of the band with negative values to exist. In other words, at higher temperatures sidebands with higher energies than the energies of the ZPL will begin to appear in the spectrum of the solid *i.e. anti-Stokes sidebands*.

Although Eqn. 2.18 provides a detailed description of the spectra of impurity in an ion, exact calculations using this formula can often be tedious and complex. However, one can reach to an approximate, simpler formula by noticing that the zero vibrational level of the system varies by $\pm\Delta_0$ about q_0. Assuming that $\Delta_0 \ll q_0^b - q_0^a$, at T = 0 we have

$$\Gamma(0) \simeq 2Mw^2(q_0^b - q_0^a)\Delta_0 \tag{2.19}$$

Similarly, the temperature dependence of the bandwidth can be taken into account by writting

$$\Gamma(T) \simeq 2Mw^2(q_0^b - q_0^a)(Av_n\Delta_n^2)^{\frac{1}{2}} \tag{2.20}$$

where Δ_n is the amplitude of the breathing mode oscillating in the vibrational level. Since $\frac{1}{2}Mw^2\Delta_n^2 \simeq \hbar w(n+\frac{1}{2})$ we find

$$\Delta_n^2 = \Delta_0^2(n+\frac{1}{2}) \tag{2.21}$$

therefore

$$Av_n\Delta_n^2 = \sum_n \frac{\Delta_n^2 exp(\frac{-n\hbar w}{kT})}{\sum_m exp(\frac{-m\hbar w}{kT})} \tag{2.22}$$

After some evaluation, Eqn. 2.22 can be reduced to

$$Av_n\Delta_n^2 = \Delta_0^2 coth\frac{\hbar w}{2kT} \tag{2.23}$$

Finally, substituting Eqns. 2.19 and 2.23 into 2.20 we get

$$\Gamma(T) \simeq \Gamma(0)\sqrt{coth\frac{\hbar w}{2kT}} \tag{2.24}$$

CHAPTER 3

EXPERIMENTAL TECHNIQUES

3.1 Introduction

The process of production of MgS:Eu and CaS:Eu thin films via Chemically Controlled Pulsed Laser Deposition (CCPLD) consisted of a series of steps and techniques that generally didn't change and were followed in the same way for all thin films studied. On the other hand, slight adjustments to some specific steps and techniques were made to accommodate for the additional doping of non-optically active species in thin films of materials such as MgS:Eu,O, MgS:Eu,HCl, CaS:Eu,O, CaS:Eu,$MgCl_2$, etc. For that reason, although this chapter will give a detailed description of the different experimental setups, methods and instrumentation used, some additional information about experimental techniques will also be provided in the following chapters when it becomes relevant to the description of specific results and/or data analysis. In addition, more information

on the experimental methodology and operation of the systems and instruments used throughout this investigation can be found elsewhere [21, 19, 20].

3.2 Material Fabrication

Most of the starting materials used for the thin films in this study were synthesized in our lab. Therefore, significant amount of effort was put into re-designing, re-building and optimizing the material fabrication setup used for making of the experimental materials studied. The setup is described in figure 3.1. It consists of an Argon gas cylinder, a liquid CS_2 reservoir, a mechanical pump, a hi-temperature tube furnace and a flow meter/ glycerin reservoir. The tube furnace consisted of a 1.52 m long, 70mm diameter quartz glass tube inside an oven manufactured by Blue M, Inc. The oven's temperature was controlled by a programable Omega CN2041 hi-temperature controller. One of the ends of the quartz tube had a removable stainless steel, disk-shaped cap with an o-ring on the inside of its capping surface (which, when installed, sits outside the quartz tube) to isolate the tube from the outside environment. This design allows for proper evacuation and at the same time allows for easy loading of the samples.

The inside surface of the stainless steel cap had to be completely coated with a few micrometers thick PFA Teflon© layer. This was done to lower its reactivity with CS_2 vapor. Without the coating, the high CS_2 flow rates necessary to promote complete reduction of the samples made could not be attained without producing anomalous results and/or ultimately damaging the samples. An uncoated cap would be prone to undesired chemical reactions between CS_2 and the cap surface's stainless steel inside the tube, particularly at high temperatures. This would ad-

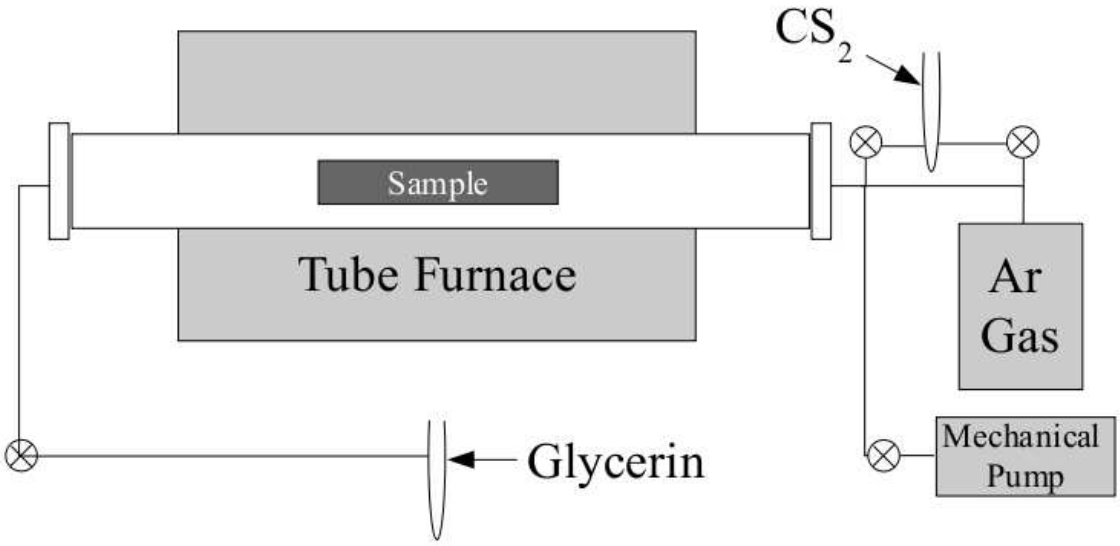

Figure 3.1: Material fabrication setup. The environment surrounding the samples can be controlled to promote the reduction of sulfates as well as hi-temperature diffusion doping. A glycerin reservoir at the end of the setup exhaust line prevents water molecules from diffusion inside the reaction tube.

versely affect the results of some of the experiments conducted. After such coating, we were able to increase the CS_2 flow to the desired rates and the reduction of sulfides became successful and consistently reproducible.

3.2.1 Sulfates Reduction and Hi-Temperature Doping

Tailoring the optical properties of the systems studied required experimenting with only the highest purity of materials possible, *i.e.* 99.99% purity or better. Unfortunately, MgS and CaS cannot be purchased commercially at that level of purity. For that reason, it was necessary to make all the MgS and CaS samples in-house. We were able to obtain very pure materials by purchasing hi-purity $MgSO_4$ and $CaSO_4$ and reducing both to MgS and CaS, respectively. The possible reactions of this processes has been previously discussed in detail elsewhere [19]. They can be written as,

$$MgSO_4 : (X)H_2O + 500^oC \longrightarrow MgSO_4 + (X)H_2O \tag{3.1}$$

$$3MgSO_4 + 4CS_2 \longrightarrow 3MgS + 4COS + 4SO_2 \tag{3.2}$$

$$MgSO_4 + CS_2 \longrightarrow MgS + CO_2 + SO_2 + S \tag{3.3}$$

Similarly, for the synthesis of CaS,

$$CaSO_4 : (X)H_2O + 500^oC \longrightarrow CaSO_4 + (X)H_2O \tag{3.4}$$

$$3CaSO_4 + 4CS_2 \longrightarrow 3CaS + 4COS + 4SO_2 \tag{3.5}$$

$$CaSO_4 + CS_2 \longrightarrow CaS + CO_2 + SO_2 + S \tag{3.6}$$

For the doping of Eu^{2+}/ $Eu^{3+}$and Cl^{-} we have,

$$MgS + (X\%mol)Eu_2O_3 + CS_2 \longrightarrow MgS : (2X\%mol)Eu + CO + SO_2 \quad (3.7)$$

$$MgS + Eu + (X\%mol)MgCl_2 + CS_2 \longrightarrow MgS : Eu, (2X\%mol)Cl + CO + SO_2 \quad (3.8)$$

respectively. Similar equations apply for the doping of CaS and can be obtained by simply substituting Ca^{2+} for Mg^{2+} in Equations 3.7 and 3.8.

To begin the reduction process, a mechanical vacuum pump is used to evacuate the tube furnace to a pressure of approximately 250x10^{-3}Torr. Argon used as a carrier buffer gas passes through the liquid CS_2 forming bubbles that will make their way across the tube, eventually pushing through the glycerin reservoir at the other end and is exhausted into a chemical hood. The appropriate amount of CS_2 and Argon needed depends on the type of sample material inside the tube, its size or amount and its shape. Generally, a higher flow rate would be required for complete reduction of the material. Typically, 10 grams of MgS will require a higher flow rate than 1 gram. We have found that 1 gram of CaS will tend to require a slightly higher flow rate than 1 gram of MgS. It is important to note that a lower flow rate of CS_2 is needed when sintering targets. Otherwise Sulfur deposits are formed on the surface of the targets.

After establishing the right CS_2 flow rate, the temperature of the furnace is gradually increased to 800^{o}C and the sample heated at that temperature for twelve consecutive hours. Then the sample is allowed to cool down to room temperature under the same flow of CS_2 before it is taken out of the tube and weighed in order to verify successful reduction.

The introduction of trace amounts of doping species into the materials studied was accomplished by either hi-temperature diffusion doping or by introducing trace amounts of vapor of a particular species into the chemically controlled environment of the Pulsed Laser Deposition (PLD) chamber. For example, the sulfides were doped with Eu using hi-temperature diffusion doping technique. That is, by mixing them with Eu_2O_3 (0.01% mol in most cases) and heating them at 980^oC under a constant CS_2 flow rate for 12 hours. Cl, on the other hand, was introduced by diffusion in some experiments or by introducing very low partial pressures of HCl for thin film deposition.

3.2.2 Powder Compression into Deposition Targets

The targets to be ablated for thin film deposition were made by hi-pressure cold compression technique. The instrument used for target compression was a Vega Enterprises Press. The materials in polycrystalline form were inserted into a cylindrically-shaped stainless steel fixture in which a piston was gradually compressed until the material was highly compacted into a disk-shaped deposition target. By slowly increasing the pressure at approximately 1000 psi/min, the material is allowed to relax and settle smoothly inside the target fixture. This avoided the formation of cracks or structural faults on the resulting target. The compression of targets was divided in three or four stages in which the pressure applied was systematically increased. At the end of each stage the pressure applied would be held constant for five minutes or longer thereby releasing some strain off the compacted material. Typically, for a maximum compression of 16000 psi, the procedure would be divided in the following four stages; 1) 0-4000psi 2) 4000-8000psi

3)8000-12000psi 4)12000-16000psi. This method proved to consistently produce targets with better structural integrity and durability.

3.2.3 Target Sintering

The technique of hi-pressure cold compression was able to produce disk-shaped solid units that were hard enough for gentle handling but that would tend to brake or crack when exposed to external stresses caused by routine handling or even ablation-induced stress during deposition. The fast, high energetic transfer from the pulsed laser beam into the atomic constituents of the targets creates structural stresses on them sometimes resulting in structural damage. For this reason, after the targets were compressed they would go through a sintering process that would produce a significantly denser and more durable target. This sintering consisted of heating the targets up to 800^oC for 12 hours inside the same hi-temperature furnace used for the fabrication of the material. Like with the material fabrication procedure, this was always done under a constant flow of CS_2 to avoid sulfur deficiency in the material while it was kept at high temperatures.

3.3 CCPLD Thin film Deposition

All thin films studied in this investigation were produced via CCPLD. A schematic diagram of the system used for this purpose is shown in figure 3.2. In this system, the beam of a Lambda Physik LPX 305I Eximer Laser ($\lambda = 350$nm) is focused into a material target inside a high vacuum chamber. The process of making this thin films via CCPLD generally consists of two phases [22]. In the first phase, all components, instruments and tools were cleaned, prepared and/or

installed to create the appropriate environment inside the vacuum chamber and ensure complete control of all relevant parameters responsible for the production of good quality thin films. The second phase consisted of the deposition of an optically active material onto MgO substrates followed by the deposition of a ZnS capping layer on top to protect the other sulfide thin film layers from the environment. After this, the samples were taken out of the vacuum chamber and were prepared for characterization. The different steps taken to produce the thin films are described in further detail in the next sections.

3.3.1 Cleaning of the Substrates

To begin with the CCPLD experiments, we first thoroughly cleaned a batch of new MgO substrates. The first step was to carefully rinse them with de-ionized water. After that, they were immersed into liquid (95% -98% purity) Hexanes, cleaned by ultrasound for 15 minutes, taken out of the solvent and left to dry for at least 5 minutes. Then, the substrates were immersed into a new solvent and the ultrasound cleaning step was repeated. The new solvents used were spectral grade purity or better Ethanol, Acetone and Methanol, in that order. Right after this cycle was completed and the substrates were completely dry, they were assembled in the substrate holder of the vacuum chamber and the substrate holder was in turn installed in the chamber. From this point on, the chamber pressure was lowered to approximately $5\text{x}10^{-2}$Torr or better using a mechanical pump and subsequently to approximately $5.0\text{x}10^{-7}$Torr or better with a turbo-molecular pump. This procedure ensured that only a minimal amount of contaminants could come in contact

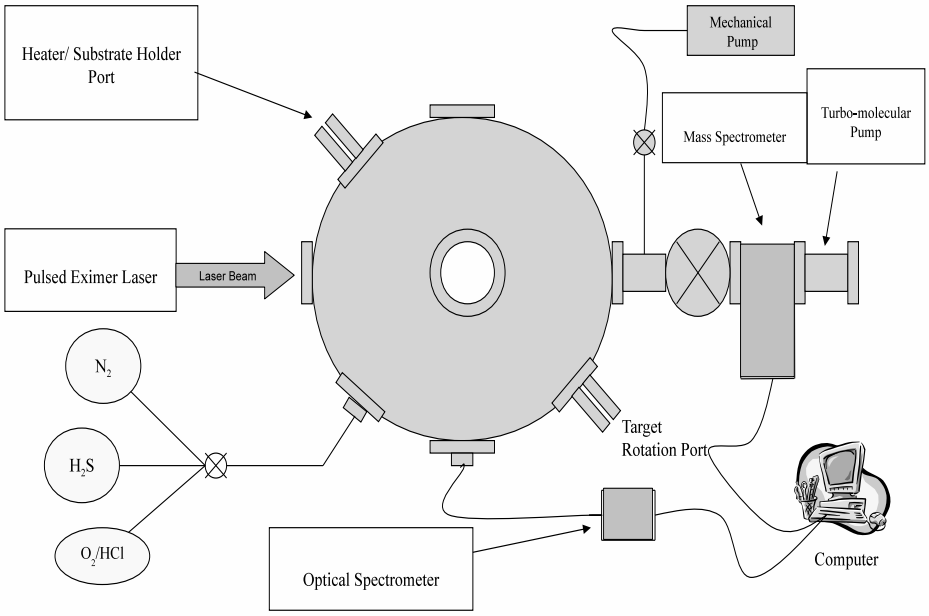

Figure 3.2: CCPLD system schematic diagram. Gas inlets allow different gases to be added inside the vacuum chamber to establish the appropriate thin film growth conditions. A mass spectrometer and an optical spectrophotometer monitor the chamber environment composition and laser plume emission, respectively.

with the substrate surface, plume or eventually the condensed ablated material. It promoted the cleanest in-chamber environment possible and consistently produced good results.

3.3.2 Establishing the Right Growth Environment

The same way that it was very important to have absolutely clean parts inside the vacuum chamber during our experiments, it was critical to create the right growth environment during thin film deposition as well. It meant having a chamber totally free of contaminants and also ensuring that the right amount of sulfur was present in the environment during deposition of thin films. Otherwise, the films would show sulfur deficiency in their structure hence resulting in undesirable optical properties [23]. Pure N_2 gas was used to create inert, contaminant-free conditions inside the chamber before and after thin film deposition and also to flush off the contaminants from the system whenever needed. Given that a reducing and sulfur rich atmosphere is necessary for appropriate thin film growth, pure H_2S was added to the chamber during deposition. As the H_2S gas interacts with the laser plume, it will dissociate into hydrogen and sulfur ions. The hydrogen will produce locally reducing conditions and sulfur will promote vacancy-free stiochiometry of the thin films.

Right after the substrates and chamber, along with its components, had been thoroughly cleaned, all parts were properly assembled and the vacuum chamber was sealed. For the purpose of ridding the inside of the CCPLD chamber of trace contaminants, a turbo pump would bring the pressure inside the chamber down to a baseline pressure, 1.0x10^{-7}Torr - 5.0x10^{-7}Torr. The pressure was monitored

at all times using a Kurt J. Lesker IG4400 Ionization Gauge Controller.

In addition, to monitor the contaminants in the chamber during and before thin film growth a mass spectrometer was used. An Inficon TSP2 Quadrapole Mass Spectrometer was used for this purpose. Conventionally, this type of systems are designed to monitor trace species at very low baseline pressures ($1x10^{-4}$Torr or better). We designed our mass spectrometry system to be able to operate at higher pressures as well (approximately $5x^{-3}$Torr). Thus, it was a very powerful tool that provided the capability of quantitatively documenting the environmental profile inside the chamber before, when the pressure is low, and during deposition when the pressure is high. The TSP2 Mass Spectrometer is connected to a computer via an RS232 cable providing complete automation for this application. Mass Spectrometry allowed us to study the growth conditions both qualitatively as well as quantitatively and make comparisons between different phases of the same experiment and between experiments conducted at different times. Therefore, this addition to our growth chamber resulted in far better control over deposition parameters and a deeper understanding of the effects of variation of conditions.

One important aspect was that our residual gas analysis made it possible to determine quantitatively the effects of flushing the inside of the vacuum chamber with N_2 gas during the chamber evacuation phase of the CCPLD deposition experiments. Figure 3.3 shows the effect of flushing. Successive scans of the mass spectrometer reveal by how much the amount of contaminant species in the chamber decreased and how much the overall cleanliness of the growth environment improved after conducting a certain amount of N_2 flushes. The top-left graph on figure 3.3 shows a scan of chamber conditions 90 minutes after opening the gate valve to the turbomolecular pump and before flushing the system with N_2 gas.

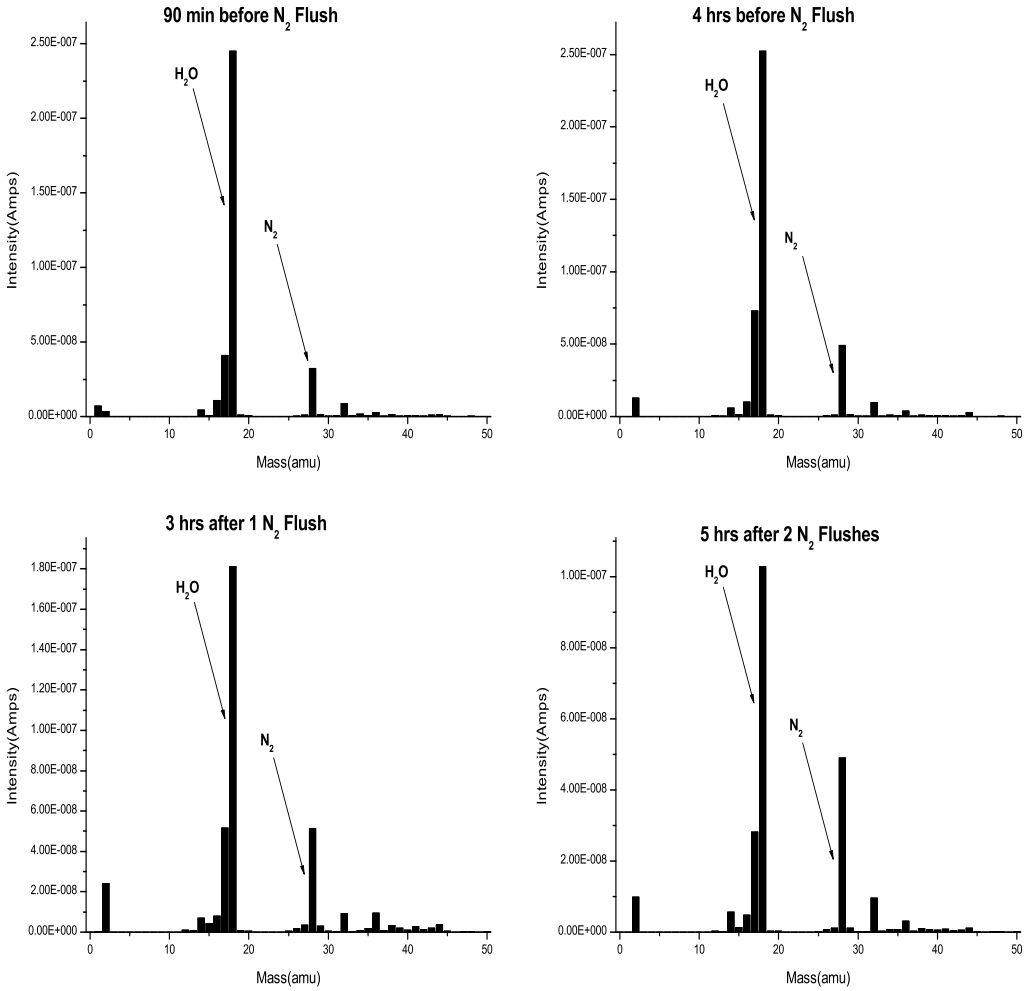

Figure 3.3: N_2 flush comparison. The top-left and top-right graphs show the environmental species concentration 90 minutes and 4 hours, respectively, before flushing the vacuum chamber with N_2. The bottom-left graph corresponds to a chamber species scan 3 hours after an N_2 flush. The bottom-right graph corresponds to a scan 5 hours after 2 consecutive N_2 flushes. The bottom graphs show evidence of over a 72% reduction in chamber contamination after at least 1 N_2 flush.

Taking the H_2O peak as reference, it can be seen that the peak lies just below the 2.5x10^{-7}Amps mark on the intensity axis. Here, the amount of contaminants is determined by amount current produced by ionized species. After 4 hours of opening the gate valve, the top-right graph shows that this peak has barely changed in intensity and is located just below the 2.5x10^{-7}Amps mark. Right after that, N_2 gas was introduced inside the chamber gradually increasing the chamber pressure up to a value slightly above atmospheric pressure. This N_2 was then flushed by our ultra-high vacuum system. The bottom-left graph in figure 3.3, scanned 3 hours after the first N_2 flush, shows that the intensity of the H_2O peak was significantly decreased to 1.8x10^{-7}Amps. This is a 72% improvement over the conditions before the flush. Finally, the flushing procedure was conducted once more in an attempt to establish a limit on the number of N_2 flushes that would make this procedure a practical one. On the bottom-right graph, the H_2O peak reached a minimal value of 1.0x10^{-7}Amps (a 55% improvement) but only after 5 hours of continuos pumping down by the turbomolecular pump. Further increments in flushing cycles did not produce significant improvements in the level of contaminants inside the chamber.

In a different experiment, comparison studies were made on differences between performing a single N_2 gas flush against 3 or more consecutive flushes. As ultra-high vacuum requires a very long time to achieve, around 6 hours or more, such experiments are necessary to minimize the chamber's cleaning time requirements. Figure 3.4 suggests very marked improvements in the scanned data for chamber conditions between a first single N_2 flush and 3 consecutive flushes. It should be noted that both data were acquired after 3 hours of evacuation following the flushing. The H_2O peak in the left graph, single flush, lies at an intensity around

2.5x10^{-11}Amps whereas the same peak appears at around 5.0x10^{-12}Amps for the three flushes graph on the right. This amounts to a 2.5-fold improvement. Furthermore, the ratio of H_2O peak intensity to H_2O peak intensity improved from 1 to 4 on a first, single flush experiment described in figure 3.3 to approximately 1 to 1 on the subsequent 3 consecutive N_2 flushes as shown in figure 3.4. For this reasons, it was decided that two N_2 flushing cycles were to be performed for thin film deposition experiments. The first flushing cycle consisted of a single N_2 flush at the time when the chamber reached a vacuum of 5x10^{-6}Torr. After the first flushing cycle, the chamber was evacuated down to 1x10^{-6}Torr. A second flushing cycle consisted of 3 consecutive flushes followed by evacuation. At this stage, evacuation is relatively faster and a pressure of around 5x10^{-6}Torr can be reached after approximately two hours. This ensured the cleanest growth environment inside the chamber throughout our investigation. It should be noted that there is significant difference between the intensity of the peaks in the graphs on figure 3.3 and the intensity of the peaks in the graphs on figure 3.4. This difference mainly corresponds to a more sensitive mass spectrometer scanning mode in figure 3.3. The actual intensity on both figures appears relatively similar when this scanning feature is turned off.

Once a desired contaminant-free environment was achieved, H_2S gas up to a partial pressure of 5.0X10^{-3}Torr was slowly introduced inside the chamber. This pressure provided optimal conditions for MgS:Eu thin film growth as previously established [19]. This completes the process of achieving appropriate growth conditions and therefore the second phase of PLD experiments will be discussed in the following section.

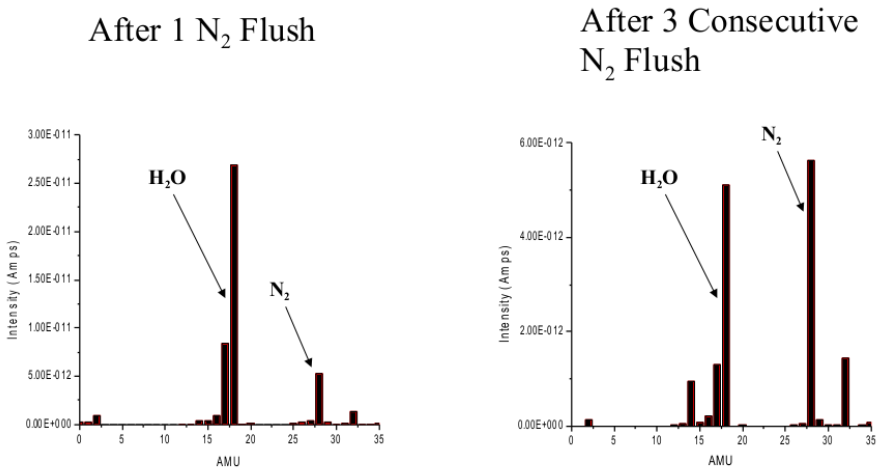

Figure 3.4: N_2 consecutive flushes comparison. The data on both graphs were scanned 3 hours after the beginning of turbo pump evacuation. The left graph corresponds to the case for only 1 N_2 flush and the right graph to the case for 3 consecutive flushes. There is a 5-fold decrease in the H_2 peak intensity after 3 consecutive flushes.

3.3.3 Multilayer Thinfilm Deposition

The first step is to set up the Eximer laser for operation with the right parameters such as intensity, repetition rate and the right wavelength of radiation. For the depositions during our experiments the Eximer laser wavelength was always set to $\lambda = 350$nm. The second step is to establish uniform ablation of the target by the Eximer laser pulse. For this purpose, the target is placed on a rotating disk-shaped mount in the target holder and is set to rotate at approximately $\frac{1}{10}$ rev/s, see figure 3.5. This also allows for a more uniform deposition of thin films. The rotating disk mount is itself mounted on a revolver type feedthrough that allows for the target material to be changed without the need to open the vacuum chamber. The designed of our chamber allows for up to four targets to be mounted onto the target holder. By simply manually rotating the target holder in increments of 90 degrees, a target inside the chamber can be moved out of the focal point of the laser beam and a new target would then be in position for ablation.

Thin films substrates are placed on the substrate holder facing opposite to the direction of the plume generated by the laser beam's ablation of the target. During deposition, the substrate is heated to temperatures ranging from 200-800^{o}C. This is accomplished by a ceramic heater. The substrates sit on a thermocouple that measures deposition temperatures controllable to values of 800^{o}C. These substrates were of crystalline MgO <100> plates, typically 10x10x1mm, and were purchased from Semiconductors Engineering, Inc. All MgO, MgS, and CaS have cubic crystalline structure and very very similar lattice constants as shown in table 3.1 [19, 24]. Therefore using MgO as a substrate will promote uniform MgS or CaS thin film layer growth. It is also transparent to visible wavelengths therefore it

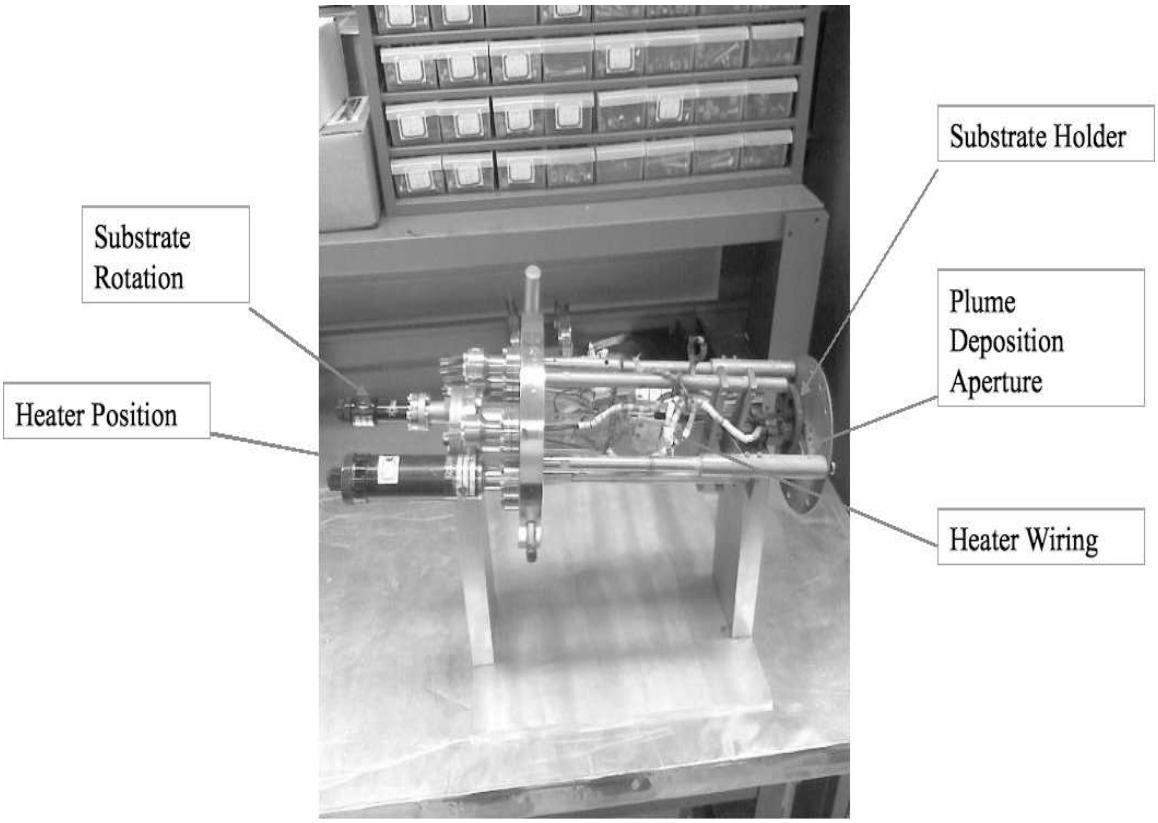

Figure 3.5: Substrate holder with heater assembly. The MgO substrates are installed into the substrate holder where they can be rotated in and out of the laser plume path while the vacuum chamber is sealed. A temperature controller regulated the temperature of the substrates during deposition.

Material	Crystal Structure	Lattice Parameter (A^o)	Melting Points (^oC)
MgS	Cubic	5.2	2227
CaS	Cubic	5.7	2525
SrS	Cubic	6.02	~2000
MgO	Cubic	4.2	2826
ZnS	Zinc-blend Cubic Wurtzite Hex.	5.41 (3.8, 6.3)	1700
Al_2O_3	Hex.	4.8, 12.9	2045

Table 3.1: Structural and thermal properties of various sulfides [19, 24]

is very convenient for use in the characterization of thin films with special spectral properties like MgS:Eu. The MgO offers a base that supports the active optical layers with no spectroscopic interference.

The CCPLD chamber has several quartz windows that allow for real-time visual inspection as well as spectroscopic measurements of the thin film deposition process. Using such windows we performed spectroscopy of the laser plume. Being able to monitor the plume emission is a very valuable tool for various reasons. First, it helps in keeping track of various deposition parameters like plume intensity and to some degree, deposition rate. Second, it provided a spectral fingerprint

for every target used during the experiments conducted. Therefore, not only could a particular target be compared to the others but its spectrum itself could be monitored as a function of time to detect variations like material degradation due to chemical reactions and other undesired effects related to the reactive environment inside the chamber during thin film deposition.

For real-time spectroscopic laser plume monitoring, a Ocean Optics HR4000 Optical Spectrometer was used. This instrument consists of a focusing lens assembly connected to a fiber optics cable which is in turn connected to a photodiode array spectrometer with spectral range of 200nm-1100nm. The HR4000 is connected to a computer via a USB cable making its data collection fully automated. The collection lens of the spectrometer sits just outside the quartz window of the chamber at approximately 18 inches from the center of the target plume. Some integration of the data was necessary for low intensity emission lines. Typical integration time was between 1-2 seconds. The emission spectra are shown in figures 3.6, 3.7 and 3.8. The spectra of the different plumes are dominated by singly and doubly ionized Ca, Mg, and Zn ions. These lines can be identified by comparing the data to NIST's Atomic Spectra Database. Figure 3.6 shows the MgS:Eu plume spectrum collected during the deposition of that type of thin film. The three most intense emission peaks correspond to the eximer laser line at $\lambda =$ 350nm and two of the electronic transitions of the singly-ionized Mg atom at $\lambda =$ 383nm and $\lambda = 517$nm. A similar graph is shown in figures 3.7 and 3.8 for the spectrum collected during the deposition of CaS:Eu thin films and ZnS capping layers, respectively. In these graphs it is clear that the CaS:Eu plume spectrum is significantly richer than the other spectra collected. This is due to the relatively more complex electronic structure of the Ca ion.

The chamber has several additional ports to which different types of gaseous sources can be connected to. In the experiments conducted as part of this investigation H_2S, N_2, O_2 and HCl were the gases connected to these gas ports. Once a baseline ultra-high vacuum (UHV) pressure was reached inside the chamber H_2S was added inside the chamber up to a partial pressure of $5.0x10^{-3}$Torr. The eximer laser was then turned on and the beam is carefully directed and focused onto the target. The pulse repetition rate used was 20Hz and the energy per pulse set to 200mJ on constant energy mode. Ablation of the target would then start taking place against a dummy substrate inside the chamber. This was performed for approximately 5 minutes to clean off any possible contamination that might otherwise lay at the surface of the target. After this, an MgO substrate was rotated into position and locked in contact with a heater in the back of the substrate holder assembly. The heater slowly increased the temperature of the substrate up to 550^oC. At that point, the laser beam would again be turned on and the ablation of the target would result in the deposition of the optically active layer onto the substrate. Active layer deposition was usually 1 hour and the thickness of the films would result in approximately 2μm, giving a deposition rate of approximately $30\mathring{A}$/min. Then, the chamber was evacuated one more time and fresh H_2S gas was let inside again, up to a pressure of $5.0X10^{-3}$Torr. This time, the ZnS target would be cleaned off against a dummy substrate for approximately 5 minutes before the MgS:Eu deposited substrate was locked in position and heated up to 275^oC. Finally, the ZnS capping layer would be deposited for 45 minutes. Then, the substrate was left to cool down while the inside of the chamber was evacuated for the last time to perform an N_2 gas flush before opening the chamber

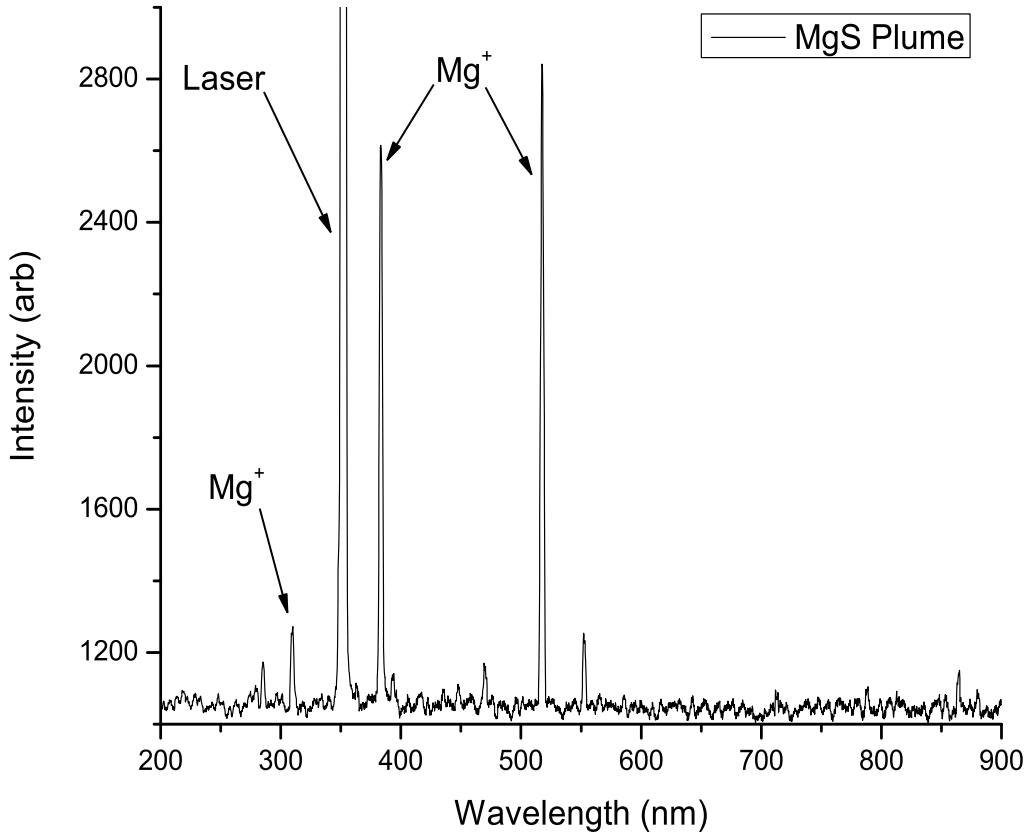

Figure 3.6: MgS:Eu plume emission spectrum. Several singly-ionized Mg emission peaks can be identified in the spectrum.

for the removal of the thin films.

3.4 Characterization of Samples

A significant effort during this work was given to characterizing the thin film produced in the lab. This included their physical characterization as well as their atomic scale characterization revealing the potential of the thin films for spectral storage and related applications. Therefore, during this phase, thickness measurements and scanning electron microscopy were performed to determine the physical properties and, on the other hand, Laser-induced Fluorescence Spectroscopy (LIFS), Absorption Spectroscopy were performed to study the optical centers relevant to spectral storage and related applications. All these characterization experiments, with the exception of electron microscopy for most of the samples described in the next chapter, were always performed in-house. For this reason, most samples studied by LIFS, Absorption Spectroscopy and profilometry were characterized immediately after fabrication but were not looked at under the electron microscope for a time ranging between 2 to 10 months after fabrication, depending on the sample. Therefore, the length of time after fabrication was only considered when analyzing the data presented in the SEM section of this chapter.

3.4.1 Emission Spectroscopy

Generally, the first characterization step was performing LIFS. Figure 3.9 shows the LIFS experimental setup. It consists of an Coherent Innova Sabre Ar Ion

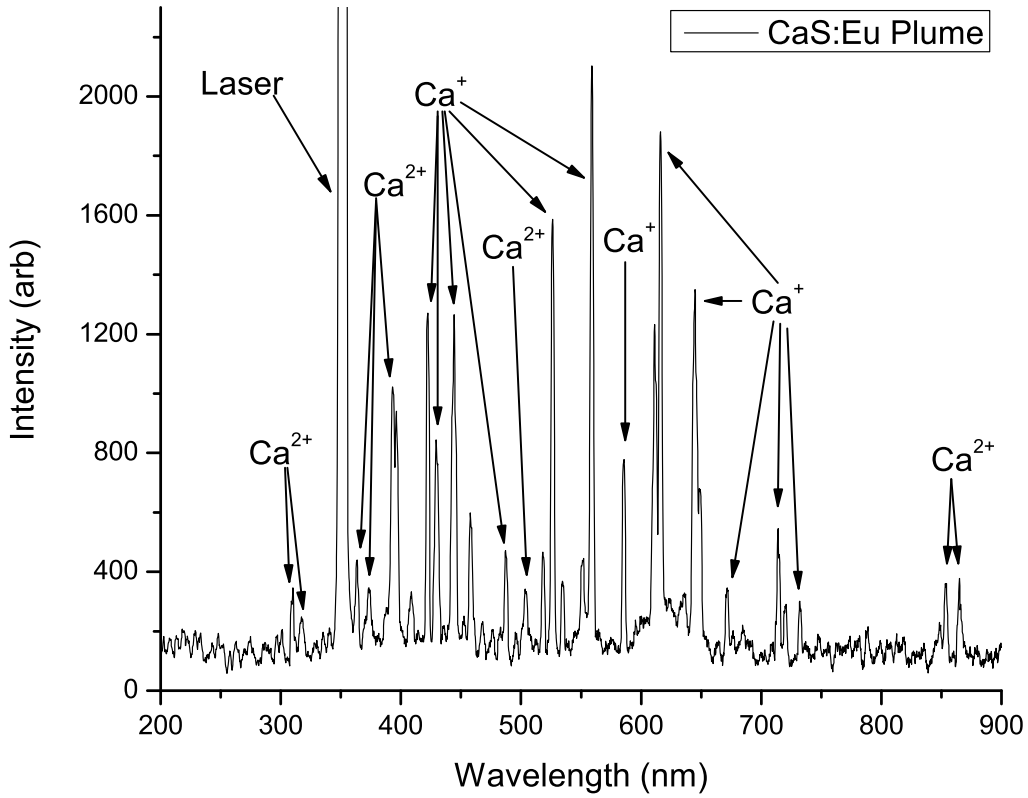

Figure 3.7: CaS:Eu plume emission spectrum. The Ca spectrum is very rich and shows a large number of emission peaks belonging to singly-ionized as well as doubly-ionized Ca ions.

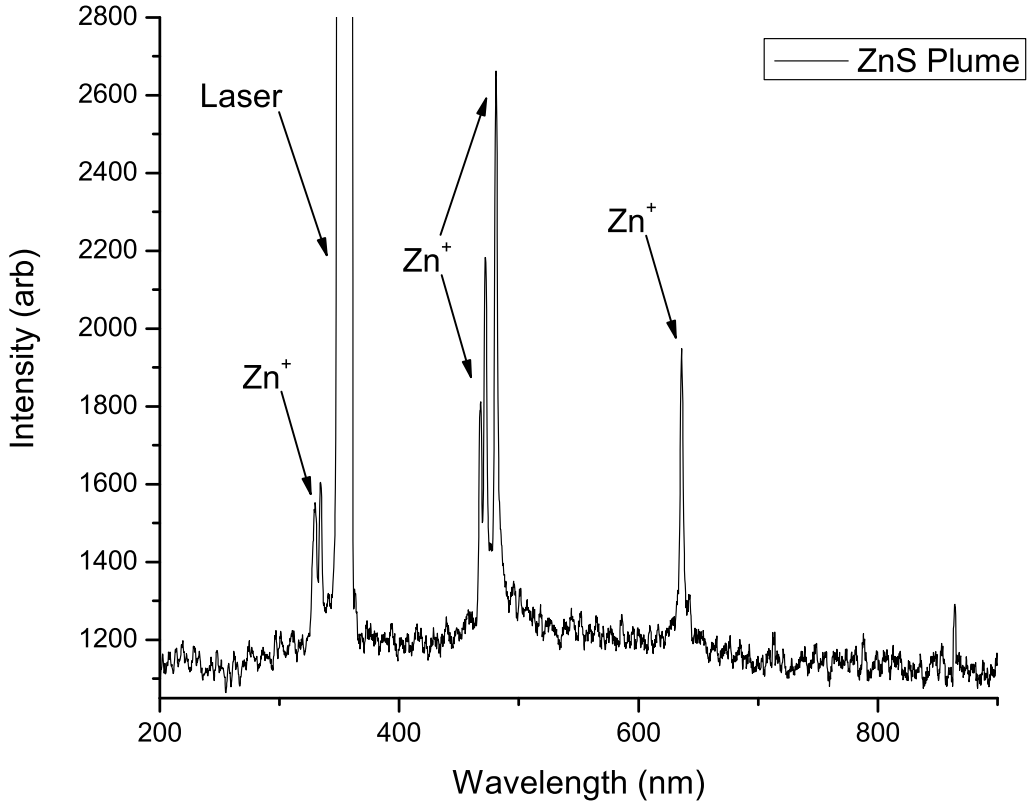

Figure 3.8: ZnS plume emission spectrum. Several singly-ionized Zn emission peaks can be identified in the spectrum.

laser (λ = 514nm), an ADP Cryogenics Displex DE-202 He Closed-cycle Refrigerator, a SPEX 750M Monochromator, a Photo-multiplier Tube (PMT), a computer interfaced via a National Instruments BNC-2080 Interface Card controlled by LabView© software and optical components used to re-direct the laser beam. The samples were attached to a oxygen-free copper "cold finger" inside the refrigeration chamber and cooled down to approximately 11K. The laser power was set between 1mW-5mW. The beam is then focused onto the sample through a quartz window in the closed-cycle refrigerator and all reflected light was similarly collected and focused onto the monochromator slit. The reflected light was filtered using a 540nm high pass filter and the monochromator slit width was usually set to values ranging from 200μm- 400μm. The computer drives a stepper motor that controls the monochromator. Light from the monochromator goes through a PMT connected to a Stanford Research Systems SR830 DSP Lock-in Amplifier that sends a voltage signal to the computer and the spectrum of the sample emission is recorded for analysis.

3.4.2 Absorption Spectroscopy

A Varian Carry 500 Spectrophotometer was used to perform absorption spectroscopy of the thin films produced during this work. It provided valuable spectral information on MgS:Eu as well as ZnS thin films. The nature of studies on those two samples is very different. In ZnS, we studied the bandgap of the bulk material whereas in MgS:Eu and CaS:Eu we studied trace amounts of Eu. Therefore, although a significant amount of time was spent performing absorption experiments

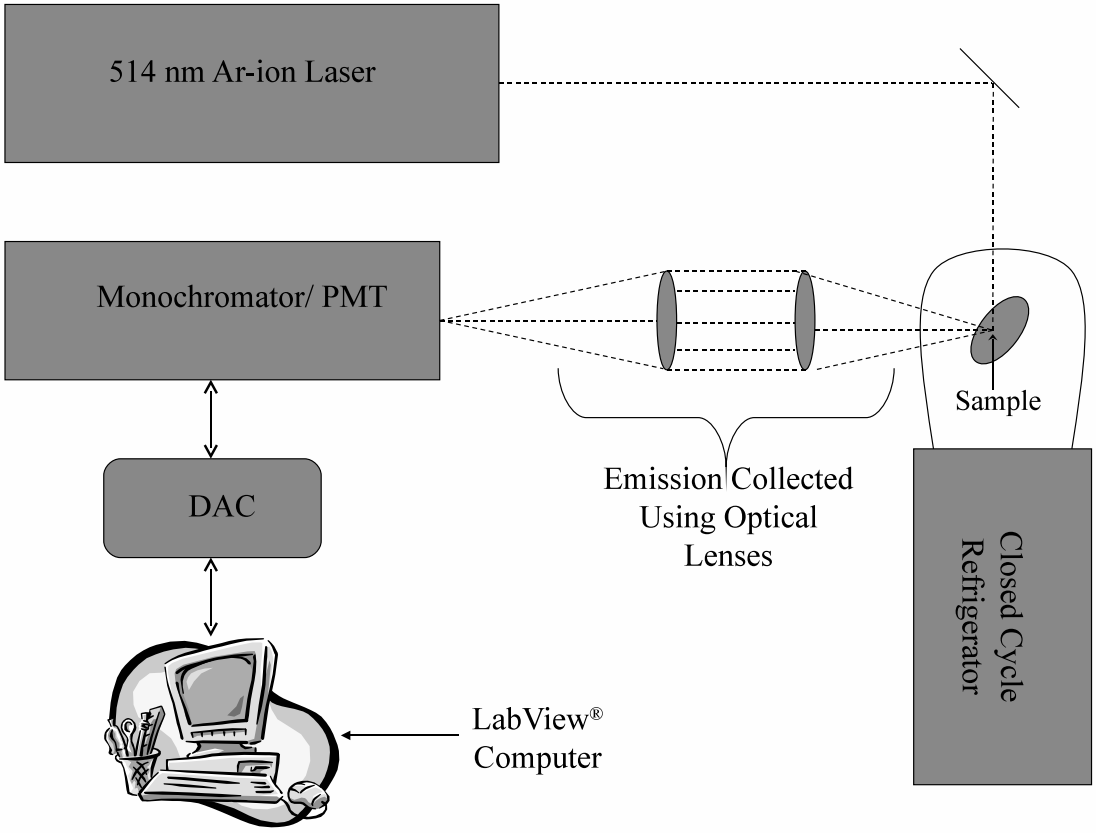

Figure 3.9: Laser-Induced Fluorescence Spectroscopy (LIFS) schematic diagram. During LIFS, an Ar-ion laser excites a cryo-cooled sample and the fluorescence signal is filtered into a monochromator. A Photomultiplier Tube (PMT) amplifies the signal before it goes into a lock-in amplifier. Finally, the signal is converted to digital format and recorded on a computer.

on both, most of the obtained data came from the ZnS thin film experiments. This is due to the fact that the optical properties of the ZnS thin films are generally more easily detectable and less specific. The optical spectrum of Eu^{2+}in the MgS:Eu thin films required a very difficult experimental procedure due to very small absorption cross sections. At low temperatures the spectral lines are narrowed therefore the MgS:Eu absorption must be performed at low temperatures. This added to the difficulty of experiments. In addition, the small thickness of the thin films made the detection of the expected spectral features on the absorption spectrum of Eu^{2+} in thin films very time consuming and difficult. To achieve the required low temperatures of the samples, the MgS:Eu thin films were attached to a copper "cold finger" inside the refrigeration chamber of the He closed-cycle refrigerator described in the preceding section. To overcome the obstacle of low signal due to low concentration of Eu^{2+}, several different techniques had to be attempted. First, the angle of incidence of the light beam hitting the sample was varied and a grazing incidence geometry was tried in order to increase the optical thickness of the films. Second, the physical thickness of the thin films was increased by extending the time of CCPLD. The thickness of the films cannot be arbitrarily increased this way as thicker films tend to peel off from the substrate as they weigh becomes larger. Therefore, thin film thickness larger than 2μm are very difficult to achieve. A third approach tried was comparing the output signal from the samples to a reference signal coming from an alternate sample bay in the spectrometer. It should be mentioned that it was not possible to do this ideally since it was largely impractical to install a second closed-cycle refrigerator to the reference sample bay of the spectrometer and only one sample could be cooled per experimental run.

A fourth approach was to cut thin films into smaller pieces and stack over each other, thereby increasing the thickness of the samples by up to a six-fold. For example, the area of the thin films substrates were usually about 10mmx10mm and usually one substrate was cut into two or three pieces with equal dimensions to make two or three different thin films. However, given that the light source aperture of the spectrophotometer sample holder was approximately 2mm in diameter, effectively only that sample area was necessary to conduct the absorption measurements. Therefore, the procedure was changed to use a whole substrate per thin film to produce larger samples. After some tests were done to ensure good results, they where cut into smaller squared pieces of approximately 3mm in area by using a diamond dicing saw. The idea was to stack many films, one in front of the other, accross the spectrophotometer light beam path. Several different fixtures were then attached to a closed-cycle refrigerator sample mount and this itself was installed inside the spectrophotometer sample bay in order to accommodate for re-positioning of the thin films or the stacking of each thin film behind the other. To do this, pieces of thin Cu plates were cut, bent and/ or molded into a desired size and shape of the array of thin films. The stack of films was then covered with the Cu thin plate and it was attached to the sample mount, perpendicular to the light beam, by using a fast-drying silver paste. Finally the closed-cycle refrigerator chamber was sealed, pumped down to hi-vacuum with a diffusion pump system and the whole system was cooled down to approximately 11K before conducting the absorption mesurement.

In the end, all these techniques, although some more effective than others, resulted in bad signal-to-noise ratio. The best results were obtained for high quality single thin films with better morphology and less scattering. It might be beneficial

to look into other options to improve the efficiency of absorption measurements of low Eu concentrations MgS:Eu thin films that incorporate sample preparation and thin film production techniques into the experimental procedures of future investigations.

3.4.3 Thickness Measurements

As our system does not have *in-situ* thickness measurement capabilities, all thickness measurements were performed after deposition. For this purpose, a Mahr Federal 5400 Surfananlyzer Profilometer was setup to sweep the contours of the thin films. The diamond tip of the profilometer's cantilever was positioned at the left edge of the thin film substrate, where a Substrate Holder holding washer had allowed no material to be deposited onto that part of the substrate, and made to move horizontally across the thin film thereby measuring the displacement of the cantilever in the z-axis direction. This displacement is displayed on a digital screen and can be printed out for a complete graph of the contour of a thin film along a given horizontal swept of the instrument. This contour would consistently result in an low flat area, namely the contour of the substrate with no material deposited on it, followed by a sudden vertical step and another high area relatively flat along the swept direction. The height of the sudden step is then used as a measurement of the thickness of the thin films [25]. The profilometer's cantilever is very sensitive and it was designed for measurements of resolution up to ± 1.6nm. Because of this, extreme care must be taken to ensure that the samples are positioned straight in an absolutely flat surface and completely free of vibrations prior to taking the desired measurements. It is very important also that the calibration steps of the

instrument are performed very carefully before every measurement so the user can make sure that the sample and the cantilever are perfectly leveled relative to each other.

3.4.4 Scanning Electron Microscope

Scanning Electron Microscopy (SEM) can be a very powerful tool in the characterization of thin films in virtually any material science scientific experiment. This investigation was not an exception. The electron microscopy performed on the samples provided very valuable information. The electron microscopy of the samples presented in this dissertation were made possible by the help of Dr. Spanier Research Group at Drexel University's Electrical Engineering Department in Philadelphia, PA. This group made their facilities and equipment available to us for the analysis of the samples and its staff provided valuable expertise in SEM operation.

The analysis of the samples was conducted using an Amray 1850 Scanning Electron Microscope. The samples studied were ZnS single layer as well as ZnS-capped MgS:Eu thin films. The length of time passed from thin film production to microscopy ranged from approximately 2 months to approximately 10 months. The microscopy was performed with the samples at room temperature.

Nevertheless, it is perhaps worth mentioning that a significant amount of efforts throughout this investigation was put into establishing internal electron microscopy capabilities in our laboratory. Through combined efforts, our research group was able to acquire a non-operational Amray 1200C SEM and move it to a new location in our laboratory for repairs, see figure 3.10. The acquisition of

this microscope was made possible due to a kind donation by Yale University's Electrical Engineering Department. The microscope was soon brought into operational status and ongoing efforts are being put forward into optimizing its image quality, resolution and decreasing its signal-to-noise ratio by making adjustments to its electron-optic elements and using video editing software. The rest of this section will discuss the progress made on the repairs of this SEM and documents its operational status for further work in the upgrade of this system.

The SEM was installed shortly after it was moved into the lab and the necessary water and electrical connections were made. Upon installation, it soon became obvious that the microscope was having a defective hi-vacuum system and could not achieve the low pressures necessary for proper functioning. Its automatic electrically-driven roughing valves were malfunctioning. To fix this, the hi-vacuum system was re-designed and rebuilt. Figure 3.11 presents an after re-build schematic diagram of the system. As a result, SEM specimen chamber pressures of $1X10^{-5}$Torr were easily achieved and an electron gun filament was installed. After arduous work, the SEM became operational and noisy images of various test samples were being captured on the instrument's display screen. A process for operating the SEM and systematically bringing it to this stage was documented and displayed by the instrument. After examining the images captured on the instrument's screen it became evident that; 1) electronic image recording capabilities were not available and 2) some improvements in image clarity and resolution were going to be necessary.

For this reason, a computer as well as Pinnacle Studio^{TM} Plus editing software were purchased. The software was installed in the computer and the computer connected to the video signal output of the microscope. This not only gives the SEM

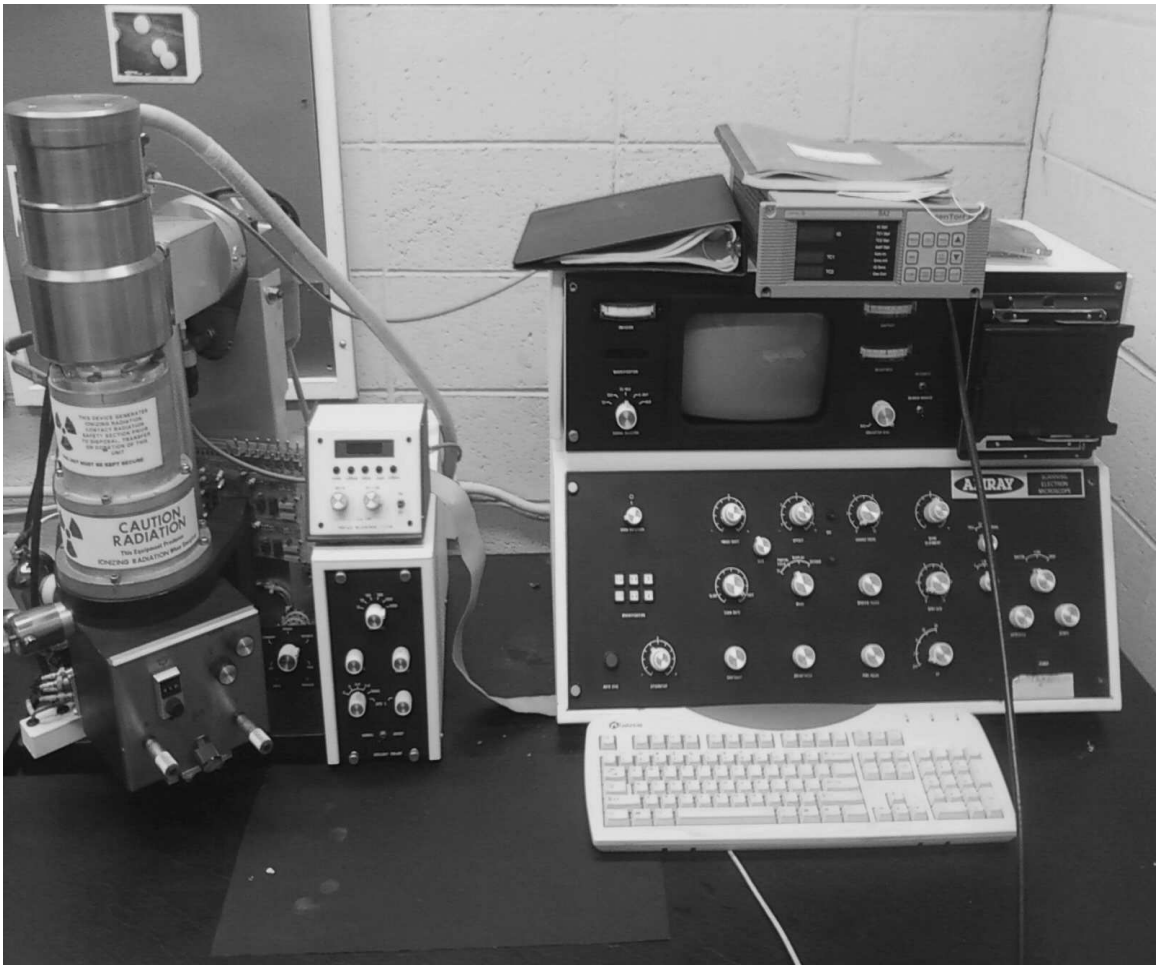

Figure 3.10: Amray 1200C SEM picture.

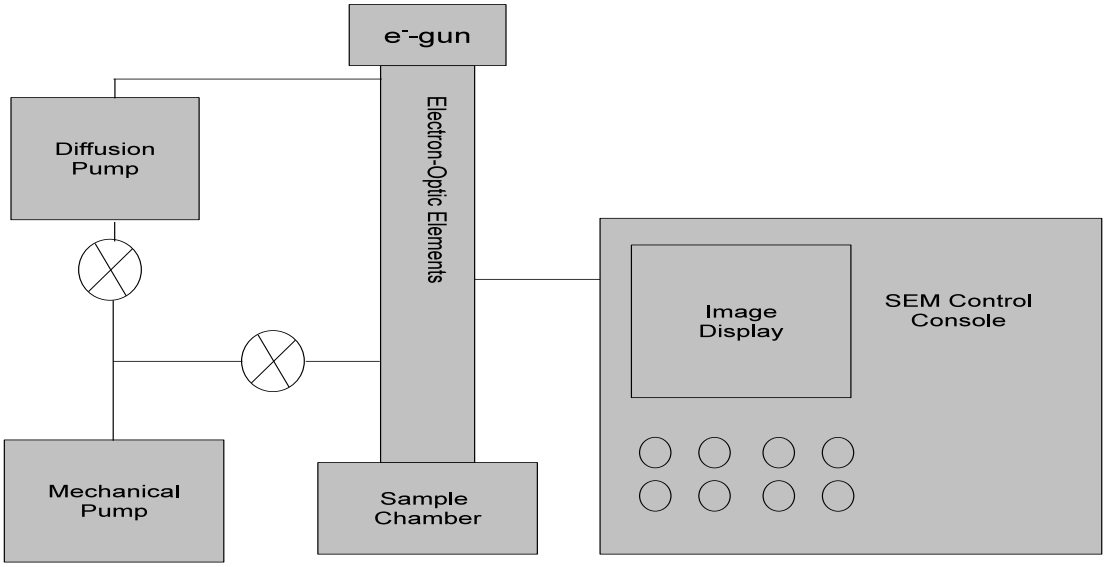

Figure 3.11: Amray 1200C SEM schematic diagram. The vacuum pumps ensure the establishment of the appropriate conditions for the electrom beam operation. The electronic signal of the images are received by the SEM console and processed for display.

users the capability of viewing sample images on a computer screen but also a way to store this images in various electronic information formats. Unfortunately, the images reproduced on the computer screen are usually a little noisier than the images obtained in the SEM screen. The contrast and brightness displayed in the computer was also usually different from the contrast and brightness observed in the SEM screen. Although the editing software was used in an attempt to improve the quality of the images, so far its noise reduction features have proven to be not very effective in improving the signal-to-noise ratio of the type of video images captured by the microscope. For example, figure 3.12 shows four images of the same ZnS thin film obtained at different magnifications. The magnification of the image in figure 3.12a was 65X. This image corresponds to a top view of the thin film where the electron beam has been focused onto one of its edges therefore the background of the image appears black. Some morphological features can be identified and evidence of chiped-off layers of material can be seen. These same features can be defined a little bit better against the background in figure 3.12b where the magnification of the image has been increased to 80X. Similar features can be seen at higher magnifications on other areas of the thin film. Figure 3.12c presents a different edge of the same thin film at a magnification of 130X. The highest magnifications achieved on thin films with identifiable morphological features up to the publication date of this thesis where near the 2000X range. However, focusing this images becomes more and more challenging as the magnification increases and obtaining quality images in this range is often a difficult task. To see this a little better, the reader can refer to figure 3.12d where at 600X morphological features are present and somewhat identifiable but the contrast and resolution of this features in not good enough to render an image in which meaningful information

about the morphology of the thin films can be obtained.

Another approach to upgrading the SEM resolution and therefore the quality of its images was to try to optimize its electron-optic elements. This is very important because if the electron beam is not aligned or focused properly the resolution of the obtained images will be adversely affected significantly. For this reason, the electron gun of the instrument was re-aligned by re-positioning the gun emission filament and adjusting the four screws located on the outside of the gun on top of the microscope electron-optic elements column. Also, the the various electron-optic apertures and their assemblies were taken out, thoroughly cleaned and re-installed. This things resulted in some minor improvements to the magnifications achievable with the microscope but the overall image quality usually lacks definition and the resolution and magnifications achieved remain well below desired values.

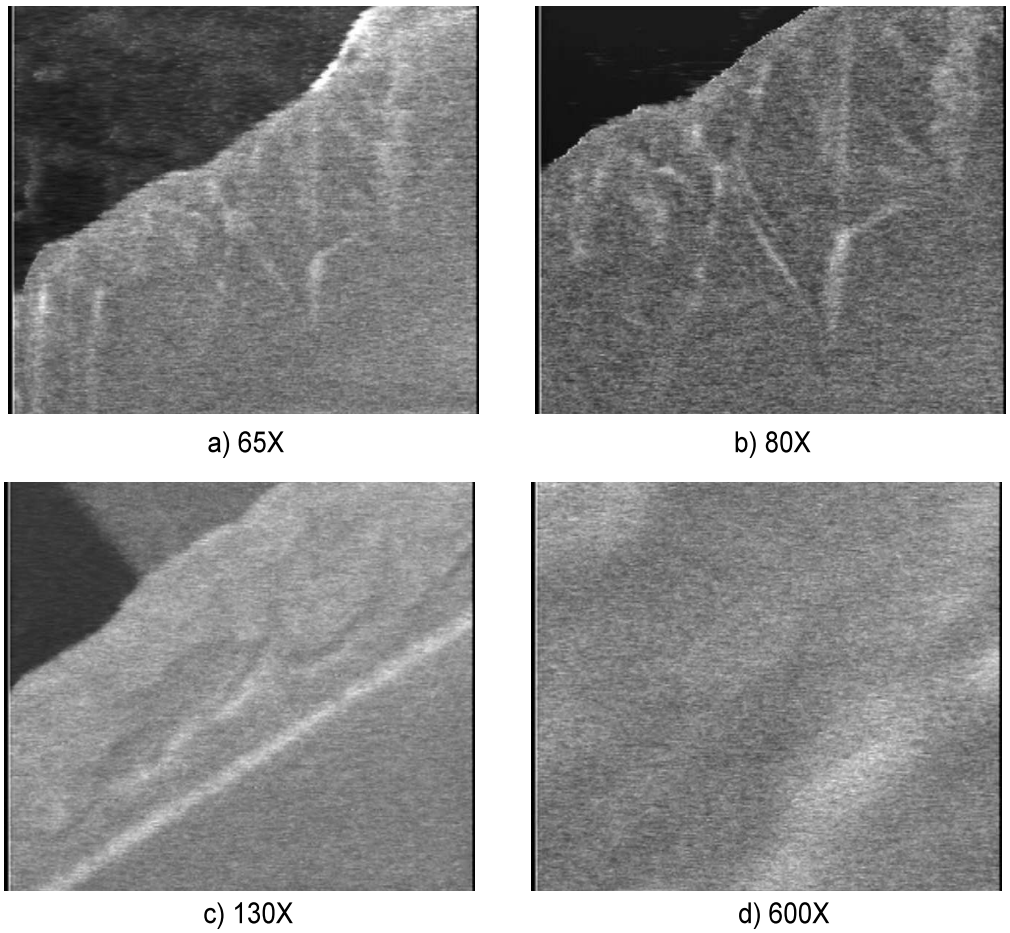

Figure 3.12: Amray 1200C SEM images at different magnifications. The images in a) and b) correspond to a top view of a ZnS thin film at 65X and 80X, respectively. A different area near the edge of the film can be seen in c) with a magnification of 130X. Features in the sample can be identified up magnifications of 600X, although the clarity and sharpness of the images is reduced a little.

CHAPTER 4

OPTICAL STUDIES OF MgS:Eu

4.1 Introduction

The MgS:Eu samples studied here were fabricated in-house, in polycrystalline form, before they were made into ablation targets and ultimately thin films. Right after the samples were produced, they were carefully prepared for the characterization of their optical properties. The characterization of their optical properties was conducted immediately after production by performing Laser-induced Fluorescence Spectroscopy (LIFS) on every sample and Absorption Spectroscopy on some.

LIFS was usually the first test performed immediately after the samples were produced. It was a very powerful tool that allowed us to obtain the optical spectrum of our materials. Given that LIFS provides a measure of the intensity of electromagnetic radiation emitted by a sample as a function of wavelength, it was very effective in determining the suitability of our samples for PSHB applications. In fact, a very likely approach to be used in the retrieval of optical information

stored in a spectral storage device in the future is by incorporating LIFS into the architecture of the device. It is important to note that the intensity measurements displayed on the LIFS graphs throughout this chapter are not absolute. In order to accommodate for the wide range of variation in the emission intensities from samples produced under different conditions throughout this investigation, it was necessary to make adjustments to the amplification factors in the signal amplifiers of the LIFS setup as well as the scaling on the display graphs.

In addition to LIFS, Absorption Spectroscopy was performed on most of the samples first made for this investigation. However, given the low concentrations of Eu in the materials made and the technical difficulties that make absorption measurements of thin films a rather challenging task, only in a limited number of the attempted measurements provided significant results.

This chapter will describe the results of all optical studies conducted and will offer a careful analysis of the experimental data obtained from them. Although in the previous chapter we introduced the methodology and equipment used during the experimental phase of this work, additional information on experimental procedures specific to particular results to be discussed will be given in this as they become relevant.

4.2 MgS:Eu Thin Films

Figure 4.1 shows the emission spectroscopy spectrum of an MgS:Eu thin film taken at a temperature of 15K. The spectrum reveals a clearly defined inhomogeneously broadened ZPL with a peak at $\lambda = 578$nm. The graph also shows a

vibronic band lying at lower wavelengths with it's maximum intensity approximately 10nm away from the ZPL. This kind of spectrum is ideal for spectral holeburning at low temperatures for two main reasons; 1) it exhibits a relatively broad ZPL and clearly defined features 2) its Debye-Waller factor, the ratio of the integrated intensity of the ZPL to the sum of the integrated intensities of the ZPL and vibronic band, is relatively large given the slightly less-than-cubic nature of the MgS lattice. In fact, previous members of our group have shown the burning of hundreds of spectral holes in an MgS:Eu sample of very similar optical spectrum [8]. This material was one of the most basic systems we studied and we used it as a point of reference when trying to tailor and develop new systems with spectral holeburning potential.

4.3 MgS:Eu,HCl Thin Films

As mentioned in chapter 1, previous member of our group conducted experiments that studied the effects on the optical properties of introducing partial pressures of O_2 during the deposition MgS:Eu thin films [9]. They were able to show that increasing the O_2 pressure during deposition promotes the creation of O-associated centers in the thin films. That is, they produced thin films under different O_2 partial pressures, ranging from 0mT to 100mT, and found that increases in pressure gradually reduces the intensity of the Eu center at λ =578nm and increases the intensity of the O-associated Eu center at λ =588nm (also seen in figures 4.2, 4.3 and 4.4). Similar experiments were conducted during this investigation. HCl impurities were introduced inside the deposition chamber followed by a careful study of the effects of these variations on the optical properties of the

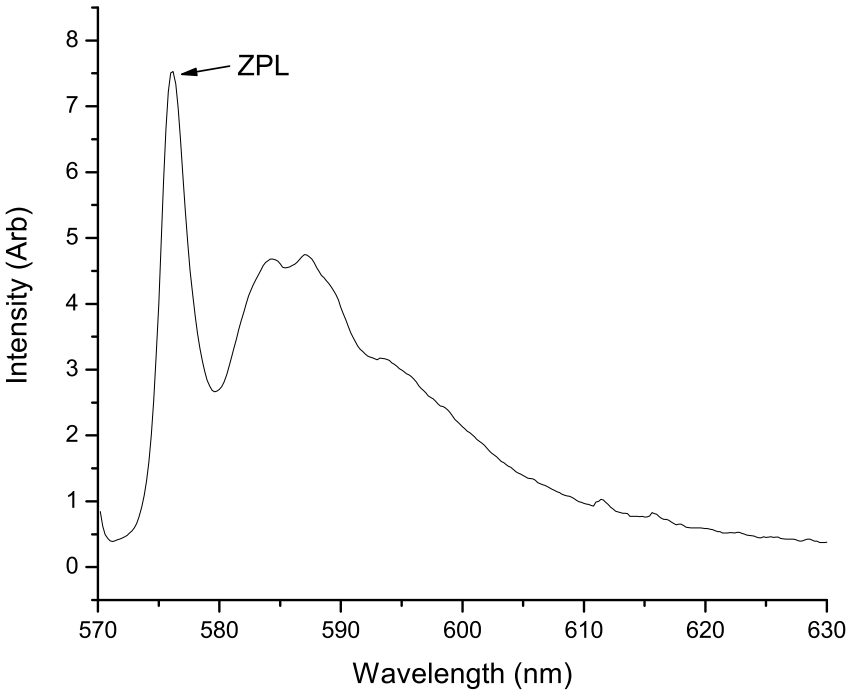

Figure 4.1: MgS:Eu thin film LIFS spectrum. The peak of the ZPL lies at around $\lambda = 577$nm and its vibronic band usually lies approximately 10nm at lower energies.

MgS:Eu thin films.

Variations in the optical properties of the produced thin films were observed even when only relatively low partial pressures of HCl were added during their growth process. In fact, partial pressures as low as 5mTorr resulted in significant changes to the emission spectrum of the thin films, see figure 4.2. This figure corresponds to the LIFS spectrum of an MgS:Eu thin film that was made by adding 5mTorr of HCl inside the deposition chamber right before the start of deposition. The figure shows a strong emission peak at $\lambda = 588$nm that is characteristic of the O-associated Eu center. Furthermore, increasing the partial pressure of HCl on following samples resulted in a systematical decrease in the intensity of the Eu center ZPL and a corresponding increase in the intensity of the O-associated Eu ZPL. Figure 4.3 shows that by adding 20mTorr of O_2 the Eu center ZPL has completely disappeared and the only discernible feature in the spectrum is the ZPL corresponding to the O-associated Eu center. Moreover, increasing the partial pressure of HCl even further seemed to increase the intensity of the 588nm emission line. This pattern seemed to continue until about 40mTorr where the creation of O-associated Eu centers seems to saturate and the overall emission intensity from the thin films begins to decrease gradually after that point. It is important to notice also that increasing the HCl pressure seemed to broaden the width of the O-associated Eu center's ZPL suggesting that films becomes less homogeneous as O^{2-}, and possibly Cl^{-}, impurities are incorporated in large concentrations.

Figure 4.4 shows a comparison between three spectra of MgS:Eu thin films grown under different partial pressures of HCl. The graph establishes a clear pattern in which increases in concentration of HCl during deposition gets rid of the Eu center emission peak and creates a new O-associated Eu center with its energy

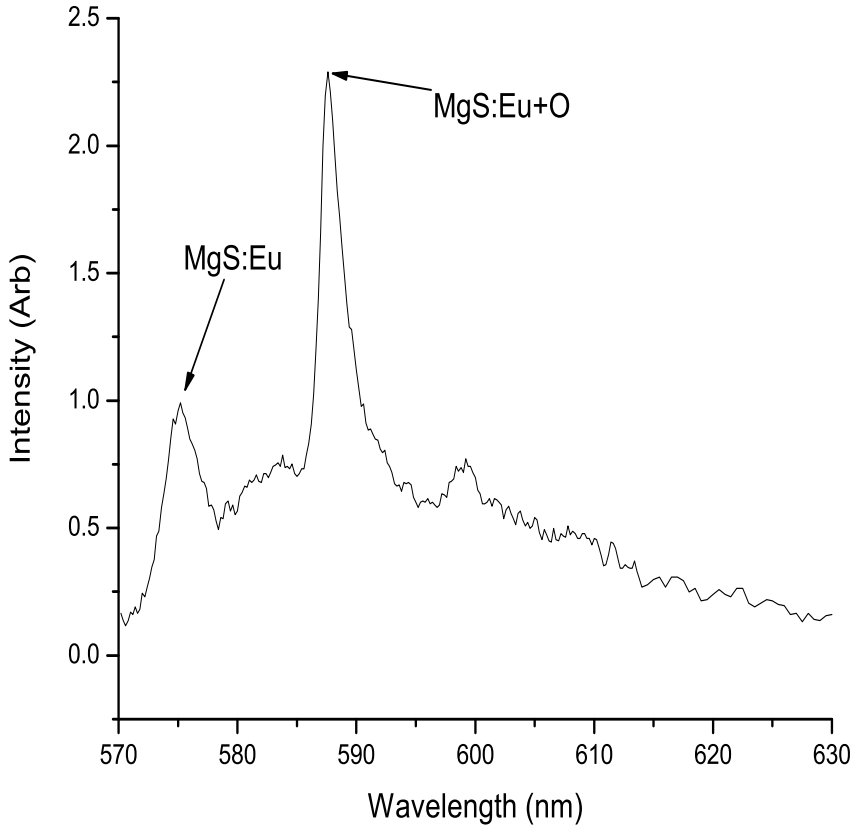

Figure 4.2: MgS:Eu, HCl thin film LIFS spectrum. An Eu center ZPL can be seen at $\lambda = 578$nm as well as an O-associated ZPL at $\lambda = 588$nm. The O-associated center is a direct result of the addition of HCl in the thin film growth environment during deposition.

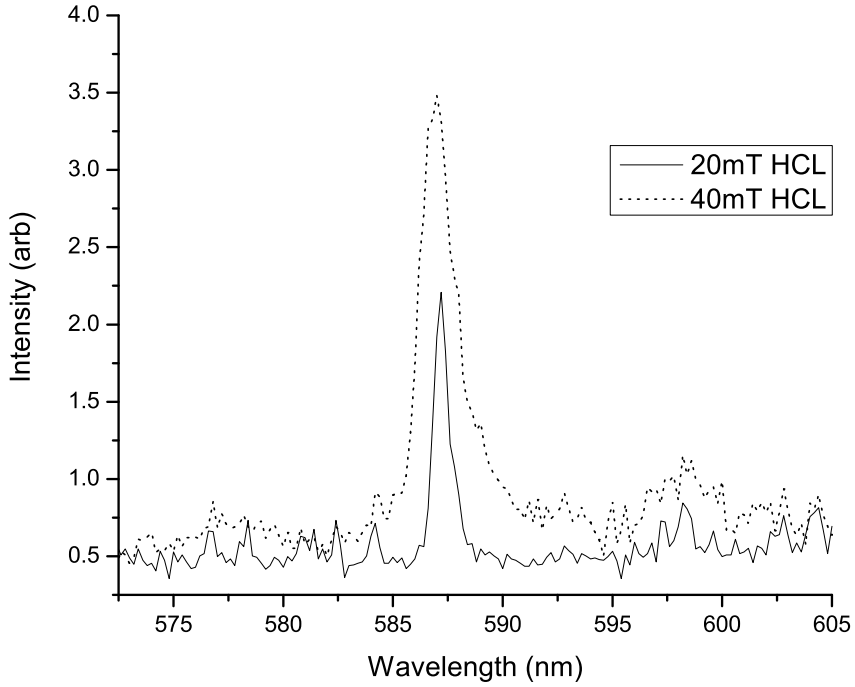

Figure 4.3: MgS:Eu,HCl thin film LIFS spectrum. The only ZPL in these spectra corresponds to the O-associated ZPL at $\lambda = 588$nm. Larger concentrations of HCl appear to broaden the ZPL of the material suggesting higher degree of inhomogeneities in the lattice due to impurities and/ or point defects.

shifted towards lower values. These results are very similar to the outcome of the oxygen partial pressure variation studies conducted previously by other members of our group. In those studies they were able to establish that the ZPL at $\lambda = 588$nm in the emission spectra of MgS:Eu thin films corresponded to the creation of O-associated Eu centers throughout the films. For that reason, the data obtained for MgS:Eu,HCl thin films during this study suggests that the introduction of HCl during deposition of the thin films promotes the desorption of trace water from the deposition chamber creating molecules of chloridic acid. It is then very possible that O^{2-} from these molecules dissociates and eventually migrates to the samples and diffuses throughout the thin films.

It is well known that O^{2-} very efficiently diffuses into MgS:Eu replacing S^{2-} as both are stable in doubly-ionized form. Furthermore, this diffusion and substitution is more dramatically seen in our experiments where we studied the environment around the individual Eu^{2+} ions. O^{2-} has particular tendency to diffuse to sites close to Eu^{2+}. This way, very small O^{2-} contents of the sample will be dramatically seen by studying the effects on the Eu^{2+}spectrum. The shift of 10nm, from 578-588nm, on the energy of the ZPL comes from the substitution of one lattice S^{2-} by O^{2-}, nearest neighbors to Eu^{2+}. The creation of O-associated Eu centers also changes the intensity distribution on the ZPL and the vibronic spectrum, Debye-Waller factor. In this case, the relative intensity of the ZPL at 588nm increase is equally dramatic as when we created the O-associated Eu center by simply introducing O^{2-} into the chamber. However, the broadening of the ZPL at 40mT is very striking. We believe that at 20mT almost all Eu centers are converted to O-associated Eu centers and further increase in HCl partial pressure results in Cl^{-} and H^{+} being incorporated into the films occupying the substitu-

tional as well as interstitial sites. This will result in overall inhomogeneity of the crystal field around O-associated Eu centers and enhance a large inhomogenous broadening of the ZPL.

Another dramatic effect is the comparison of the Debye-Waller factor between normal and O-associated Eu center. The substitution of nearest neighbor S^{2-} by O^{2-} lowers the (roughly) cubic symmetry of the Eu^{2+} site to axial symmetry thus making the otherwise cubic crystal field forbidden transition more allowed in axial symmetry. The ZPL gains intensity due to this effect and the vibronic intensity that depicts the forbidden nature of the transition decreases by a factor of almost 20 or more. Before concluding this section we must mention that a clear Cl-associated Eu center could not be observed in the form of a single ZPL. This we attribute to the high probability of the formation of O-associated Eu centers and O^{2-} affinity to go in the vicinity of Eu^{2+} selectively. For the low Eu concentration samples (0.01% molar or lower) that are needed for spectral storage there are not enough Eu left to form the Cl-associated Eu center even with non-removebable traces of O^{2-} in the chamber in the form of water molecules. Any attempt to see such Cl-associated Eu centers in the future should incorporate a mechanism of ridding the chamber atmosphere of any trace amounts of O^{2-} in any form, including H_2O.

4.4 MgS:Eu,HCl Thin Film Absorption Spectroscopy

The absorption spectrum of MgS:Eu was calculated in 1979 by S. Asano and Y. Nakao and the excitation spectrum of MgS:Eu with similar concentrations of Eu

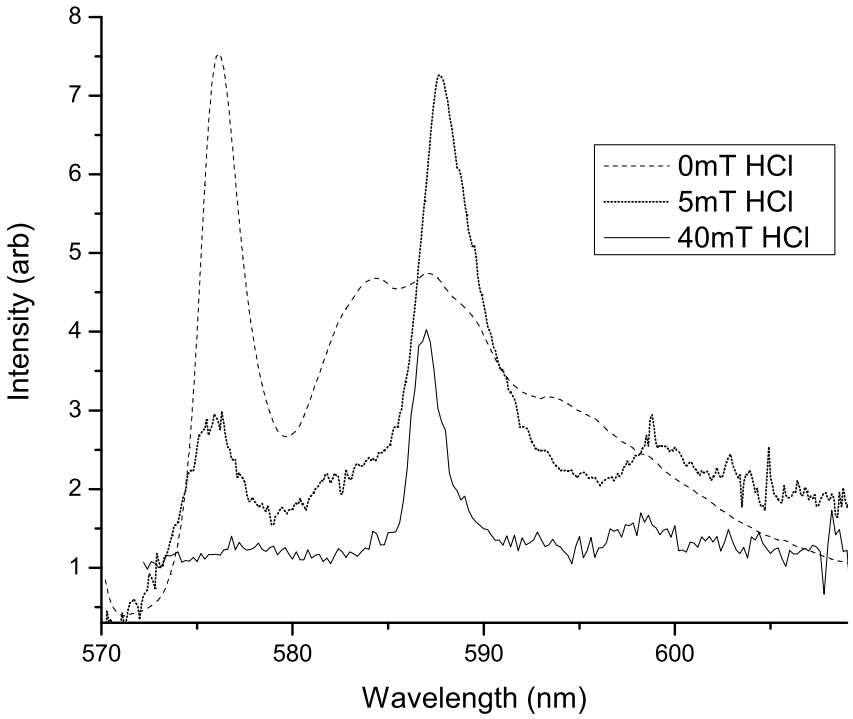

Figure 4.4: MgS:Eu/ MgS:Eu,HCl thin film LIFS spectrum comparison. Increasing the HCl concentration up to a partial pressure of 40mT during thin film growth will increase the intensity of the O-associated center's ZPL and will reduce the intensity of the Eu center's ZPL at $\lambda = 578$nm until it is no longer visible in the spectrum of the material. Note that the baseline has been shifted to clearly depict the spectrum for the case of 40mT HCl pressure.

as the ones studied here was measure by Y. Nakao in 1978 [10, 26]. Unfortunately, as mentioned in the previous chapter, due to the low concentrations of optically active species in the samples the attempts of measuring the absorption spectrum of most of the produced thin films in this study were unsuccessful. The samples made under low partial pressures of HCl were one of the handful of which their absorption spectra was successfully taken. One reason for this might be that these thin films were grown under slightly higher pressures of HCl as an additional gas in the environment of the chamber. This seemed to consistently produce thin films of very good quality. The deposition appeared very uniform and their surfaces very smooth. Furthermore, they appeared more transparent and less yellowish-hazy than the MgS:Eu thin films. Figure 4.5 shows the absorption spectrum of a MgS:Eu thin film produced under a 5mT partial pressure of HCl. The different traces of the graph represent the absorption spectrum of the same sample taken at different temperatures. It is worth noting that the intensity of the absorption signal was very weak and the signal-to-noise ration rather high. The graph shows a small absorption peak at $\lambda = 576$nm and another one at $\lambda = 574$nm corresponding to the ZPL and a vibronic replica, respectively. It can be seen from this graph that the spectrum does not vary significantly as the temperature changes from 11K to 100K. On the other hand, as the temperature increases to 120K, the ZPL peak intensity and its vibronic replica decrease to where they hardly show up in the spectrum of the sample anymore and eventually disappear shortly after the temperature was increased further.

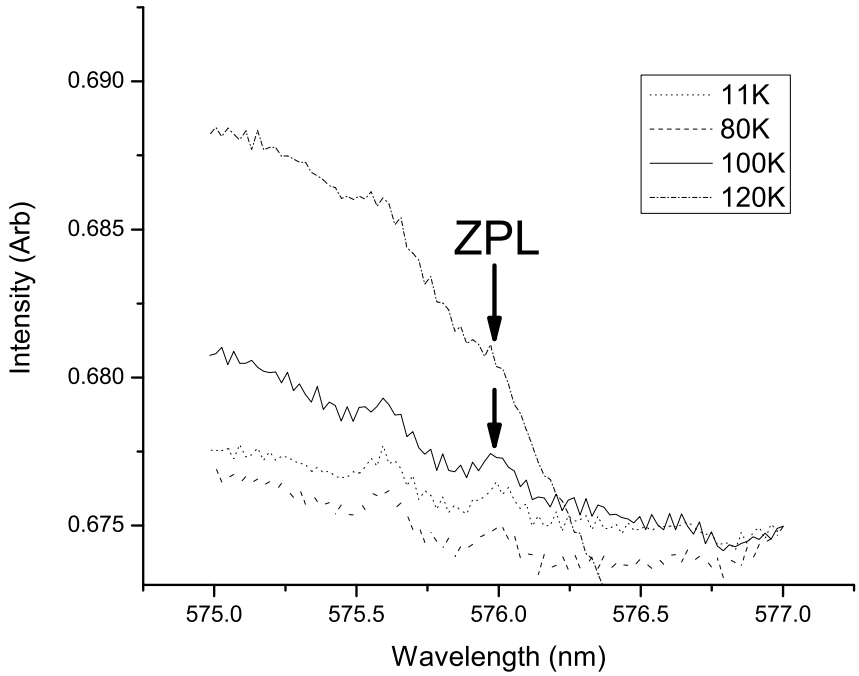

Figure 4.5: MgS:Eu,HCl thin film absorption spectrum comparison. The spectra shows a ZPL near $\lambda = 576$nm and its phonon replica at higher energies. The features remain as the temperature is increased up to 100K. After that temperature, the features slowly begin to disappear and at around 120K the intensity of the features becomes practically undetectable.

4.5 MgS:Eu,$MgCl_2$ Microparticles

Another way of incorporating Cl into the MgS:Eu thin films is to start with a target material and try to include Cl, in one form or the other, as trace amounts in the starting material. This is a lengthy process, requires material preparation and characterization at the very basic level and steps should be completed in a very careful manner for the fabrication of successful target material. However, this method has the advantage of not dealing with HCl gas which is highly reactive and posses significant safety hazards. Therefore, it soon became clear to us that the best choice in this regard was making target materials with a mixture of $MgCl_2$ in MgS:Eu.

We noted that after a period of time of adding HCl inside the deposition chamber with the purpose of doping Cl^- into MgS:Eu, the deposition target began degrading suggesting that HCl was causing unwanted reactions with the MgS:Eu material. In particular, the color of the surface of the target changed. At this stage the intensity of the laser plume became significantly less intense suggesting that significant surface transformation took place as time went on to the extent that we could not produce any films. This could be due to two reasons. First, the absorption characteristics of the target may have changed. Second, the chemistry of the surface may have being transformed. This reactivity of HCl in the chamber did not cause much damage to the rest of the deposition components near the plume as it had been coated with a thin protective layer of SiC. However, this is not possible for the deposition target. Thus, it always remains exposed to the environment and therefore vulnerable to chemical deterioration during thin film growth.

To overcome this unforeseen obstacle, a new technique for Cl^- doping was implemented. A method of hi-temperature diffusion doping for Cl^- was then established in the lab and, subsequently, different samples of MgS:Eu,$MgCl_2$ in polycrystalline form were made with varying concentrations of $MgCl_2$. The samples synthesized ranged from 0% to 1% molar concentration. This materials were synthesized prior to coating the capping stainless steel plate of the tube furnace with teflon and therefore high temperature reactions, specially in the prescence of $MgCl_2$, were evident by blackening of the stainless steel plate. As mentioned in the previous chapter, higher values of $MgCl_2$ concentrations would alter the synthesis reaction dynamics, *i.e.* cause unkown reactions, and ultimately result in unsuccessful sample fabrication on most attempts made during this time. The product of most of these trials would be a powdery solid with a different color that ranged from light gray to black. It is worth mentioning that most of these samples, although not the intended compounds, would still fluoresce yellow under UV illumination in a similar manner that MgS:Eu samples typically did.

At this stage we coated the stainless steel end plate of our hi-temperature tube furnace with teflon and subsequently observed that the color of the samples thus produced changed dramatically indicating that the hot gases in the environment of the furnace were not reacting chemically with the plate. The effect of the doping of Cl^- into the samples did not seem to produce any significant effects on the optical spectrum of the microparticles. This is evident from figure 4.6. This figure documents the LIFS spectrum taken from four samples of MgS:Eu with different concentrations of $MgCl_2$. For clarity, the spectra of only two samples is shown in figure 4.6a and two more are added in figure 4.6b. Figure 4.6a presents the optical spectra of samples with concentrations of 0.1% and 1% $MgCl_2$. From this

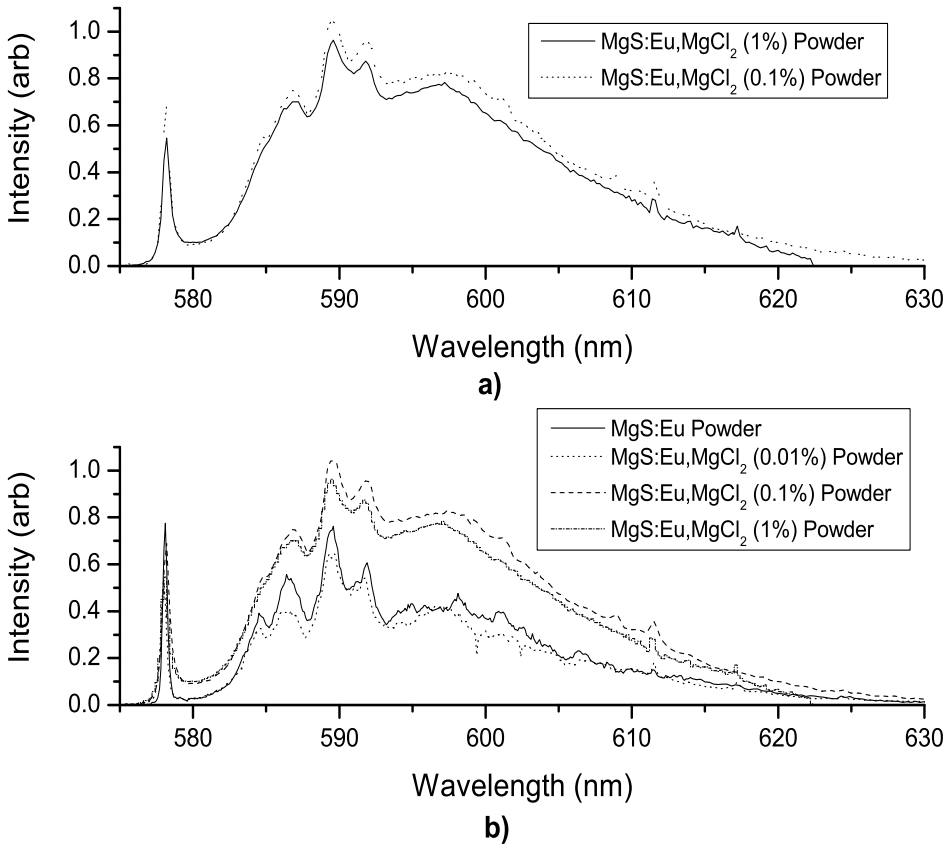

Figure 4.6: MgS:Eu,$MgCl_2$ microparticle LIFS spectrum comparison. a) Comparison graph for two samples with $MgCl_2$ concentration of 0.1% and 1% mol. b) Comparison graph for four sample with $MgCl_2$ concentration of 0%, 0.01%, 0.1% and 1% mol. No significant differences in the optical spectrum of all four samples can be observed suggesting that Cl ions do not go near Eu^{2+}lattice sites.

graph, it can be seen that there is not much variation in their optical spectrum and both exhibit basically the same spectral signatures. Figure 4.6b shows the optical spectra of samples with concentrations of 0%, 0.01%, 0.1% and 1% $MgCl_2$. Even though there is a variation of two orders of magnitude in the concentration of $MgCl_2$, the variations in the optical spectra is minimal. Their spectral properties are essentially the same. Worthy of noticing is the fact that all four spectra in the graph show very similar vibronic peaks as well as broadening of their ZPLs. This is strongly suggests that the Cl ion is not favored to go inside the MgS:Eu lattice, especially at lattice sites near the Eu^{2+} ion, by hi-temperature diffusion doping.

4.6 MgS:Eu,$MgCl_2$ Thin Films

After the doping of $MgCl_2$ at various concentrations in MgS:Eu microparticles produced no noticeable effects in their optical spectra, the materials were made into PLD ablation targets by hi-pressure cold-compression technique. Even though hi-temperature diffusion doping did not seem to produced the desired outcome of altering the energy level splitting of the 4f-5d transition of the Eu^{2+} ion, the chance of this being possible under PLD could not be ruled out. That is, the highly energetic dynamics of PLD growth still offered some potential for the technique to promote the growth of Cl-doped MgS:Eu thin films.

The procedure for producing the MgS:Eu,$MgCl_2$ thin films via CCPLD were exactly the same as for the production of MgS:Eu thin films. The results of this experiments are presented in figure 4.7. Aside from the fact that the optical spectrum of the 0.05% $MgCl_2$ thin film exhibited more intense fluorescence emission than the

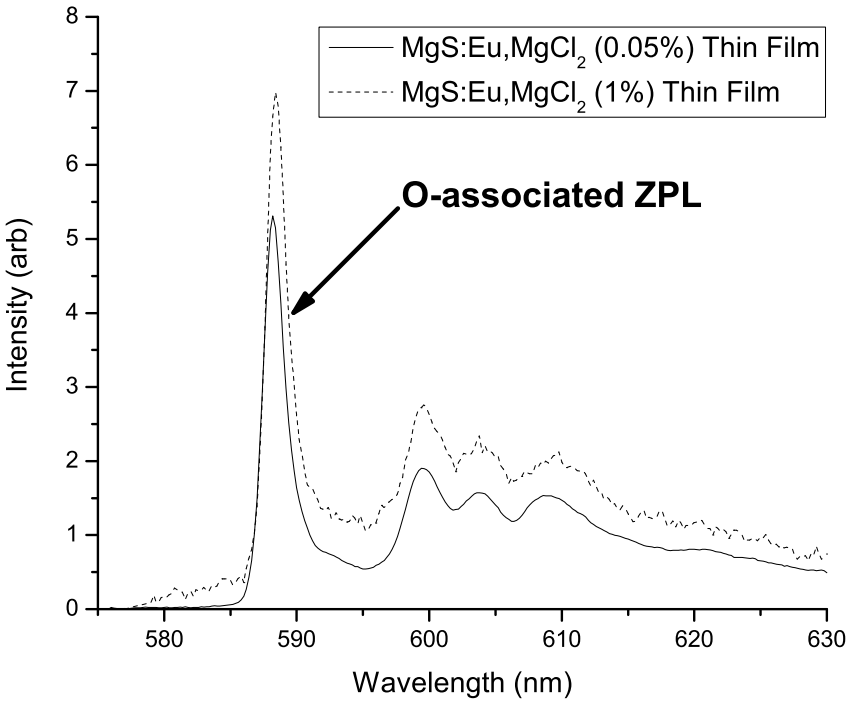

Figure 4.7: $MgS:Eu,MgCl_2$ thin film LIFS spectrum comparison. The solid line spectrum corresponds to a 0.05% mol $MgCl_2$ thin film and the dashed line to a 1% mol $MgCl_2$ thin film. Both spectra show a relatively intense O-associated ZPL peak as well as their corresponding vibronic bands shifted towards lower energies when compared to the spectra of microparticles of the same material.

1%, their optical features are almost identical. However, when these spectra are compared to the spectra of their polycrystalline counterpart discussed in the previous section, major difference between the spectra of these samples can be observed. The spectra of the MgS:Eu,$MgCl_2$ microparticles is very similar to the spectra commonly seen in MgS:Eu's but the spectra of the MgS:Eu,$MgCl_2$ thin films appears to be completely shifted, to lower energies, when compared to MgS:Eu's. In the MgS:Eu,$MgCl_2$ thin films, a very well-defined ZPL can be found at $\lambda = 588$nm followed by their respective vibronic bands, also shifted approximately 10nm in energies.

It was previously established in this work that this 588nm ZPL is attributed to an O-associated Eu center in MgS:Eu thin films. The creation of this center in the MgS:Eu,$MgCl_2$ thin films was a very unexpected result. In the absence of $MgCl_2$ it is not possible to have any O-associated Eu center in MgS:Eu thin films and we checked by thoroughly cleaning the chamber of any trace amounts of water or oxygen. The only two ways that this can happen is that; 1) $MgCl_2$ is able to liberate oxygen traces after ablation more efficiently from the chamber as has been described in earlier sections when thin film growth in trace HCl environments were described. 2) the hot plume containing Cl ions is able to liberate oxygen from the MgO substrate creating the chemical reaction given below. Although a comprehensive explanation of this results has not been developed, a few ideas that offer some insight into this phenomena have been proposed. We propose that the reaction of Cl^- ions shortly after target ablation with the surface of the MgO substrate creates new compounds that then are incorporated into the growth of the thin films. For example, one of these possible reactions can be described by

the equation,

$$2Cl + H_2S + MgO \longrightarrow 2HCl + O + MgS \tag{4.1}$$

4.7 MgS:Eu,NaCl Microparticles

Adding NaCl traces had the double advantage that it can introduce two substitutional impurities, Cl^- and Na^+. We therefore tried incorporating small traces of NaCl into the MgS:Eu taget material right from the begininng of its synthesis. The purpose of this step was two-fold; 1) the addition of a new doping element, *i.e.* Na^+, to the lattice that could interact with the Eu^{2+} ion to possibly form a Na-associated Eu center. 2) the creation of a Cl-associated Eu center in a less homogeneous system given that a rather more homogeneous system, *i.e.* MgS:Eu,$MgCl_2$, failed to show any evidence of the creation of a new center.

We were able to synthesize the desired materials in polycrystalline form. The resulting material was white in color and did not differ in any significant way from MgS:Eu in appearance. Needless to say is that the steps taken in this synthesis were exactly the same as for MgS:Eu with the exception that we added NaCl to the MgS:Eu. The LIFS spectrum in figure 4.8 belongs to a MgS:Eu microparticles doped with 0.05% mol NaCl. The spectrum shows a ZPL peaking at $\lambda = 578$nm followed by a significantly broader and more intense vibronic band at lower energies. It is worth noticing that the ZPL peak of this spectrum appears significantly broader than the ZPLs commonly found in MgS:Eu samples. This suggests that the Na^+ ion, the Cl^- or both diffused inside the MgS:Eu lattice. Given that the attempts to accomplish this with $MgCl_2$ were not successful, it might be safe to assume that in this case only the Na^+ diffuses into the lattice and not Cl^-. In

fact, looking at the results previously presented in this chapter a good amount of evidence can be seen suggesting that the Cl^- ion is not favored to diffuse inside the MgS:Eu lattice and might be released away from the chemical processes occurring during hi-temperature diffusion and thin film PLD.

Another big difference between the MgS:Eu,NaCl Microparticle spectrum and the common spectrum of MgS:Eu is that the MgS:Eu,NaCl spectrum evidences a much smaller Debye-Waller factor, therefore suggesting that its corresponding lattice is significantly more cubic than in MgS:Eu. This can be explained by the fact that the atomic radius of Na is larger than Mg's and closer to the size of Eu's. From this, we can conclude that the Na ion was diffused into the MgS:Eu lattice and has more affinity for crystal sites near Eu ions. However, charge compensations would require the symmetry to be lower and ZPL energies significantly shifted for this to happen. One possibility is that trace impurity ions are occupying the available sites more homegenously thus reducing the overall axial crystal field component. More detailed investigations are necessary to support these interpretations.

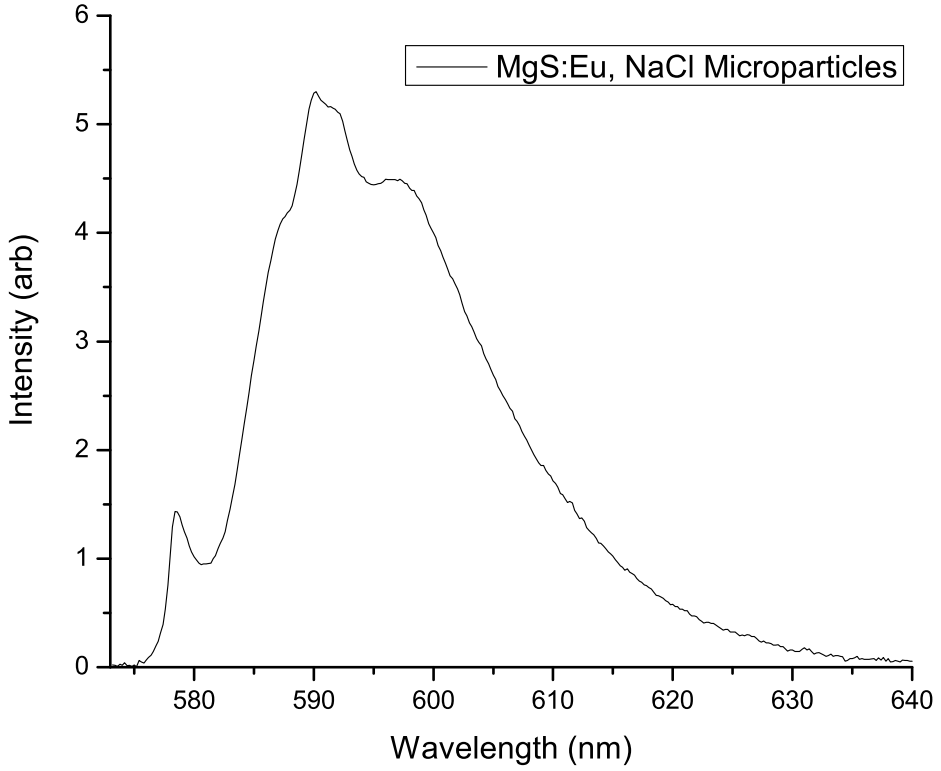

Figure 4.8: MgS:Eu,NaCl microparticles LIFS spectrum. The ZPL of the Eu optical center appears significantly broader in this sample indicating a more inhomogeneities near the Eu^{2+} site in the lattice. The significant increase on the integrated intensity of the vibronic band relative to the integrated intensity of the ZPL suggests an increase in the cubic character of the system.

CHAPTER 5

OPTICAL STUDIES OF CaS:Eu

Another major material system studied in this thesis was CaS:Eu. Despite the fact that the atomic radius of Ca^{2+} is larger than Mg^{2+}'s, CaS:Eu and MgS:Eu have very similar lattice structure and optical properties. Our investigations of CaS:Eu were prompted by our studies of producing optical centers in MgS:Eu. In fact, in previous members of our group were able to burn hundreds of spectral holes on both systems in the past [7, 27]. The material fabrication and PLD growth procedures of CaS:Eu and CaS:Eu,$MgCl_2$ were the same as the procedures followed for the fabrication of MgS:Eu and MgS:Eu,$MgCl_2$ and therefore have already been discussed in previous chapters. The optical characterization methods followed were also the same. This chapter will focus on the results of these optical characterization experiments and will present a detailed analysis of the most important findings of these studies.

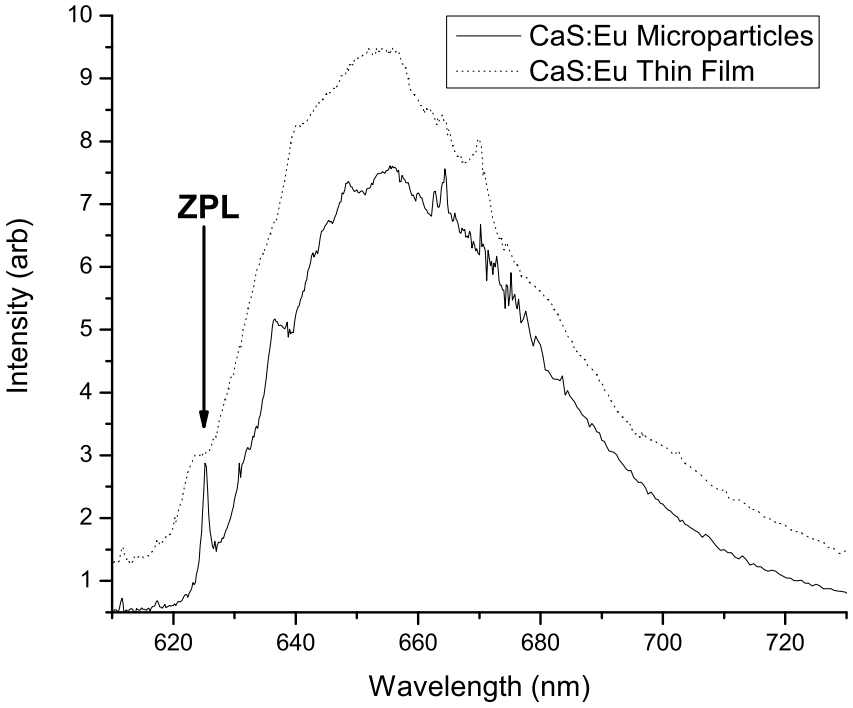

Figure 5.1: CaS:Eu LIFS spectrum comparison. The solid line corresponds to the spectrum of microparticles and the dotted line to thin films. Although the vibronic bands in both spectra are similar, the ZPL is largely sharper and well defined in the microparticles sample.

5.1 CaS:Eu Thin Films

The optical spectrum of MgS:Eu microparticles shares similarities to the spectrum of MgS:Eu but at the same time exhibits some minor differences, see figure 5.1. Like MgS:Eu, it has a inhomogeneously broadened ZPL followed by a vibronic band at lower energies. CaS:Eu's ZPL, however, usually lies around $\lambda = 625$nm. Its vibronic spectrum is also broader and more intense than its respective ZPL giving a smaller Debye-Waller factor and at the same time suggesting a stronger electron-phonon coupling. This is a direct consequence of the more cubic nature of the CaS lattice relative to MgS's. It is worth mentioning that the ZPL of CaS:Eu broadens significantly in PLD grown thin films and its intensity frequently gets re-distributed significantly relative to its vibronic intensity. For spectral storage specially, a broader ZPL is desirable where a larger number of spectral holes can be burned. But in some other applications a sharper, well defined electronic transition require a narrow ZPL. The ZPL broadening in these thin films can be greatly reduced for these applications. This can be done by simply annealing the thin films at 800^oC under H_2S partial pressures for four or more hours. In microparticles, a narrow ZPL is the consequence of the slow process of synthesis where CaS:Eu is fabricated and diffusion doping is performed at around 1000^oC for more than 20 hours. This ensure a homogenous environment around Eu therefore also sharp ZPL lines.

5.2 CaS:Eu,O Thin Films

Given that MgS:Eu thin films grown under partial pressures of O_2 promotes the creation of an O-associated Eu centers in its lattice, an experiment was conducted during this investigation in which thin films of CaS:Eu were grown under partial pressures of O_2 in an attempt to find out whether the CaS:Eu experiences a similar shift in energy of Eu^{2+}'s $4f^7$ - $4f^6$5d electronic transition. The purpose of these experiments was to quantitatively and qualitatively study the effects that the addition of O_2 impurities would have in producing the O-associated Eu center, similar to that in MgS:Eu.

To produce the CaS:Eu,O thin films, CaS:Eu was synthesized in polycrystalline form, as described in chapter 3, and made into a PLD target. The only difference between the process of making CaS:Eu,O thin films as opposed to CaS:Eu was that relatively low partial pressures of O_2 were added into the deposition chamber right before starting depositing the thin films onto the MgO substrates. In contrast to MgS:Eu,O, where ZPL was by far the dominant feature of its optical spectrum after the addition of 100mTorr of O_2, no noticeable changes were observed in the optical spectrum of CaS:Eu at O_2 partial pressures below 100mTorr. However, the optical spectrum of CaS:Eu started showing a shift towards lower energies for the added O_2 partial pressures of around 200mTorr, see figure 5.2.

Figure 5.2 shows the variation in the optical spectrum of CaS:Eu thin films as the O^{2-} partial pressure was varied from 0mTorr to 1000mTorr. It can be seen how there is a gradual shift towards lower energies of the vibronic bands as the O^{2-} pressure is increased. Significant shifts in energy can be observed as the partial pressure is increased up to 500mTorr and seems to saturate after that point. That

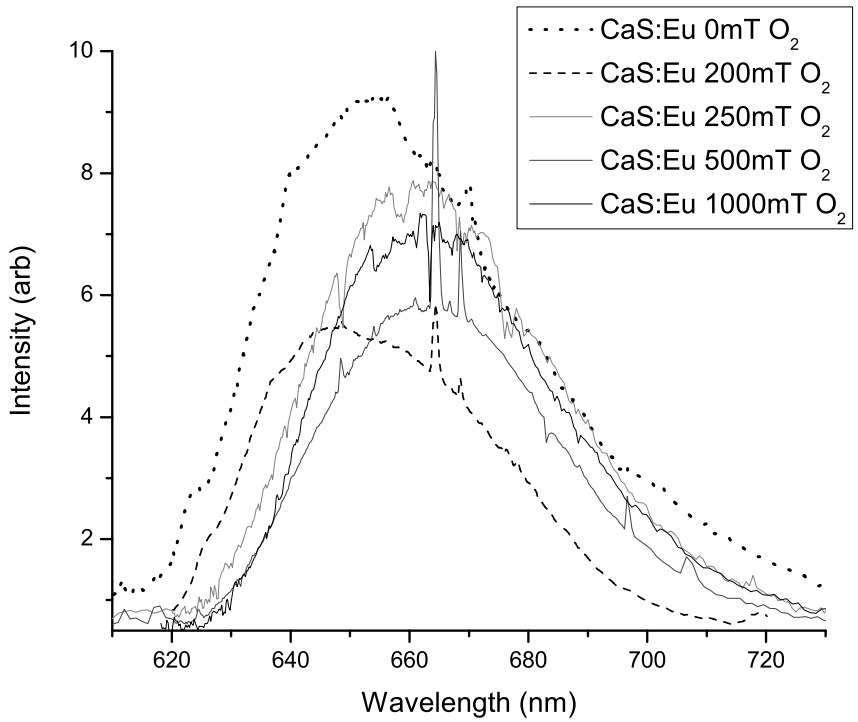

Figure 5.2: CaS:Eu,O_2 thin films LIFS spectrum comparison. As the concentration of O_2 increases to a partial pressure of 200mT the optical spectrum shifts towards lower energies. The shift gradually continues up to a partial pressure of 500mT. For partial pressure increases after that point no significant shift is observed.

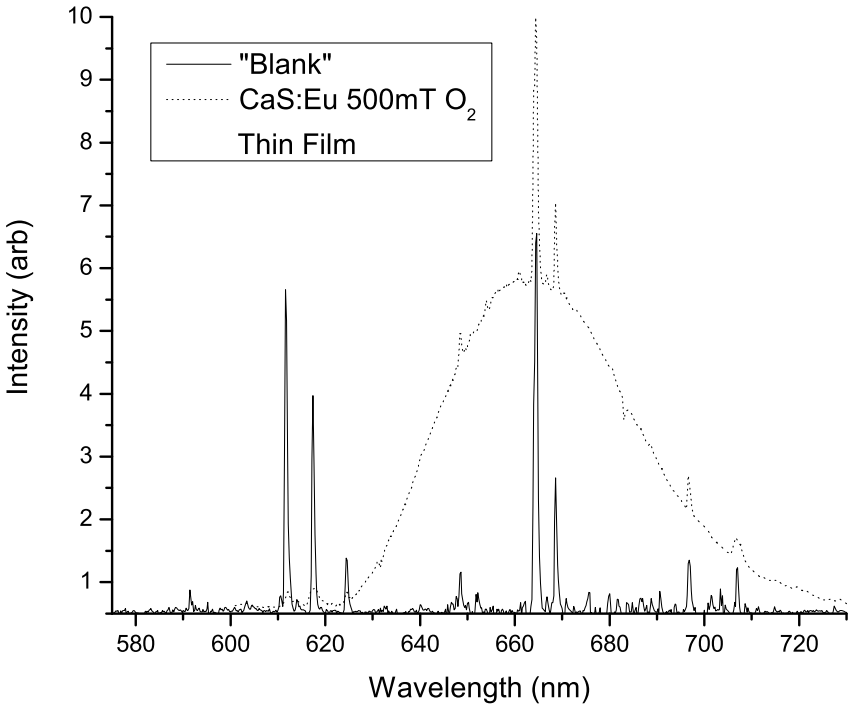

Figure 5.3: Blank (No sample) LIFS spectrum: laser plasma lines. The sharp lines on the spectrum of some CaS:Eu thin films can be correlated to laser plasma lines that also appear on the spectrum taken with no sample in the beam path.

is, no significant energy shifts were observed between increases from 500mTorr and 1000mTorr. It is important to note that the intensity of the Eu^{2+} ZPL is very low and therefore it is not very pronounced in some samples and not observable in others. Therefore, we cannot use the shift of the ZPL, which is otherwise a better standard, as a measure of energy shift. On the other hand, using the peak of the vibronic band on each sample as a reference point, the total shift of the spectral features can be measured to be as much as 10nm. It is also important to notice that the spectral intensity of each sample displayed on the graph can not be compared from sample to sample. The integrated intensity of the optical spectrum decrease with increasing the O^{2-} partial presure. That is the reason for the appearance of some sharp spectral peaks in the spectrum of some of the thin films, particularly the intense peak shown at $\lambda = 664$nm. These emission lines correspond to laser plasma emission lines and are usually very low in intensity therefore get buried in the relatively more intense vibronic features of CaS:Eu. But given that the addition of O^{2-} impurities to the lattice lowered its fluorescence intensity significantly, the laser plasma lines then tend to show up and, as they lie in the same spectral range of interest, are rather difficult to eliminate.

Figure 5.3 is given to establish a spectral fingerprint for this laser plasma lines. The figure corresponds to a blank spectrum, taken with no samples across the optical path of the laser beam at room temperature. In the graph, a series of sharp peaks throughout CaS:Eu's fluorescence emission spectral range can be observed. Particular attention should be given to the spectral peak appearing at $\lambda = 664$nm since this feature is one of the more intense and therefore shows up very near the maxima of the vibronic band in some samples. A definitive correlation between the sharp peaks of the thin films in figure 5.2 and the laser plasma lines

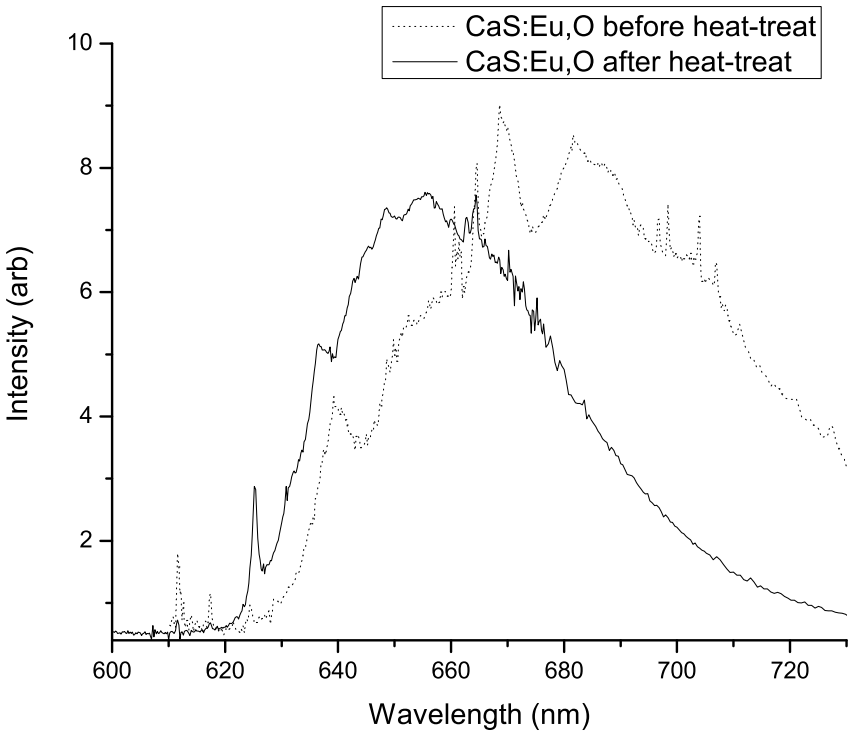

Figure 5.4: CaS:Eu,O microparticles heat treatment LIFS spectrum comparison. The shift in energy of the Cas:Eu spectrum can be reversed by appropriate heat treatment of the sample.

can be made by comparing the blank spectrum to the spectrum of the 1000mTorr O_2 CaS:Eu thin film shown in figure 5.3.

The spectral shift of the O-associated Eu center in the CaS:Eu optical spectrum was reversible. To show this, the spectrum of CaS:Eu,O microparticles was taken. This sample was then heat treated (annealed at 800^oC) under CS_2 flow for 8 hours. The LIFS spectrum of the sample was then recorded again and compared to the spectrum taken before heat treatment. The difference between the two spectra can be readily seen by looking at figure 5.4. Although the Eu^{2+} ZPL was usually more noticeable in other CaS:Eu microparticles samples previously made, this after-heat-treatment CaS:Eu spectrum still shows a remarkable shift in its spectral features when compared to the before-heat treatment spectrum. This proves that O^{2-} can be incorporated in large amounts in the the samples and it can be annealed out by heating them. This would not have been possible had the O^{2-} ion associated chemically with the Eu center.

5.3 CaS:Eu,$MgCl_2$ Thin Films

Studies on the optical properties of CaS:Eu,$MgCl_2$ thin films were also conducted during this investigation. Given that some of the experiments already described in the previous chapter had established that the the doping of Cl^- promoted the creation of O-associated Eu centers in MgS:Eu thin films, there was reason to believe that similar effects could be observed for the case of CaS:Eu,$MgCl_2$ thin films. Moreover, it was believed that the addition of the Mg^{2+} ion into the growth dynamics of the thin films could play a favorable role in the doping of Cl^-

into the CaS:Eu lattice. The introduction of an acceptor into CaS:Eu's lattice can induce the formation of native defects, like vacancies at the cation site, and this could in turn favor the doping of Cl^- under the right growth conditions [28].

The CaS:Eu,$MgCl_2$ thin films production techniques used were essentially the same as the ones used for the growth of MgS:Eu,$MgCl_2$ thin films. $MgCl_2$ was doped into CaS:Eu via hi-temperature diffusion and the resulting microparticles were compressed into PLD ablation targets. This targets were then installed inside the PLD chamber for thin film deposition.

Figure 5.5 compares the optical spectra from CaS:Eu thin films doped with 0.06% and 1% mol $MgCl_2$. In the graph, both spectra show similar features. They both show the characteristic CaS:Eu vibronic band, shifted in energy, with a maximum at around $\lambda = 655$nm. The difference in energies of the vibronic band may be seen more clearly by comparing the spectrum of MgS:Eu,$MgCl_2$ microparticles to the spectrum of MgS:Eu,$MgCl_2$ thin films, see figure 5.6. This shift in energy has similar magnitude to the shift in energy observed during the CaS:Eu,O experiments and correlates to the findings for MgS:Eu,$MgCl_2$ thin films in which the ablation of $MgCl_2$-doped MgS:Eu produced thin films with O-associated centers. A very weak CaS:Eu ZPL can also be observed on both spectra. In addition, they both show an interesting spectral feature to the high energy side of $\lambda =$ 620nm that can be attributed to the creation of MgS:Eu optical centers within the CaS:Eu structure, *i.e.* MgS:Eu in a slightly distorted CaS crystal field environment. It should be noted that although the integrated emission intensity of the vibronic bands differs by over a factor of two for CaS:Eu and MgS:Eu, the relative intensity of different features within the MgS:Eu spectrum is essentially the same. This is an important point because it reveals a tendency of the Mg^{2+}

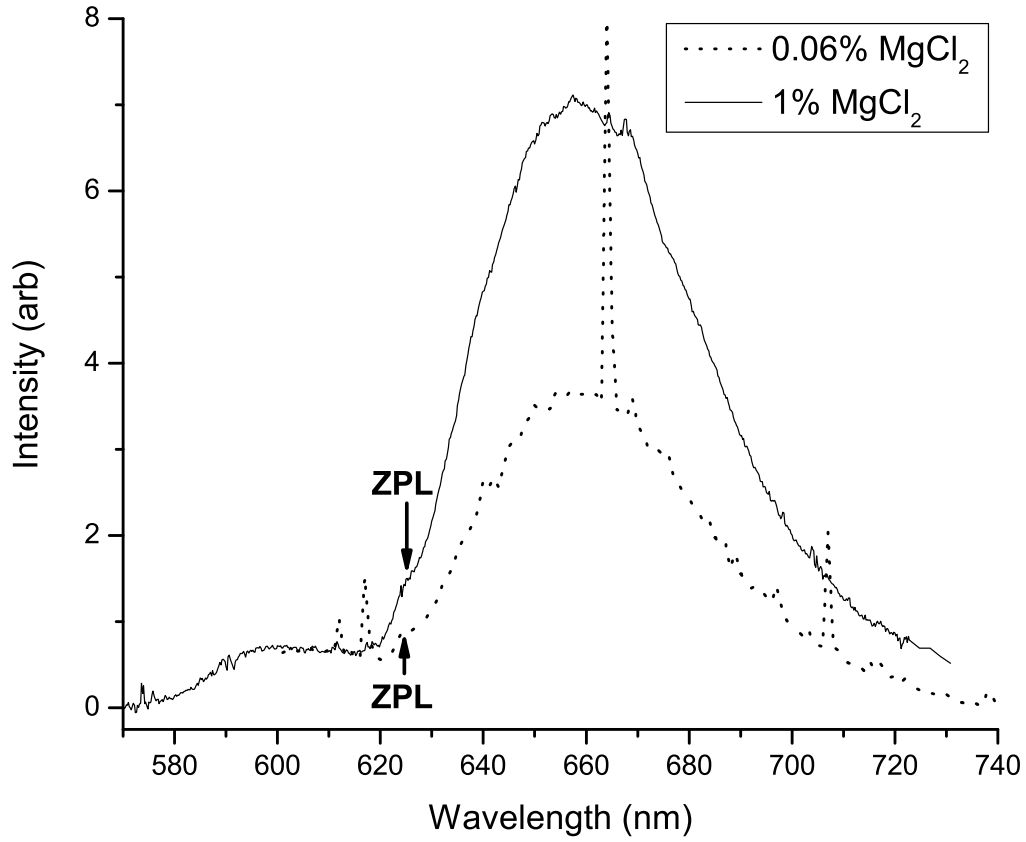

Figure 5.5: CaS:Eu,$MgCl_2$ thin films LIFS spectrum comparison. The broad spectral feature at wavelengths shorter than $\lambda = 620$nm can be attributed to the creation of MgS:Eu optical centers within the CaS:Eu lattice structure. Although the relative integrated intensities of this feature is very similar for both films, the relative integrated intensities of their CaS:Eu vibronic bands differ by over a factor of two.

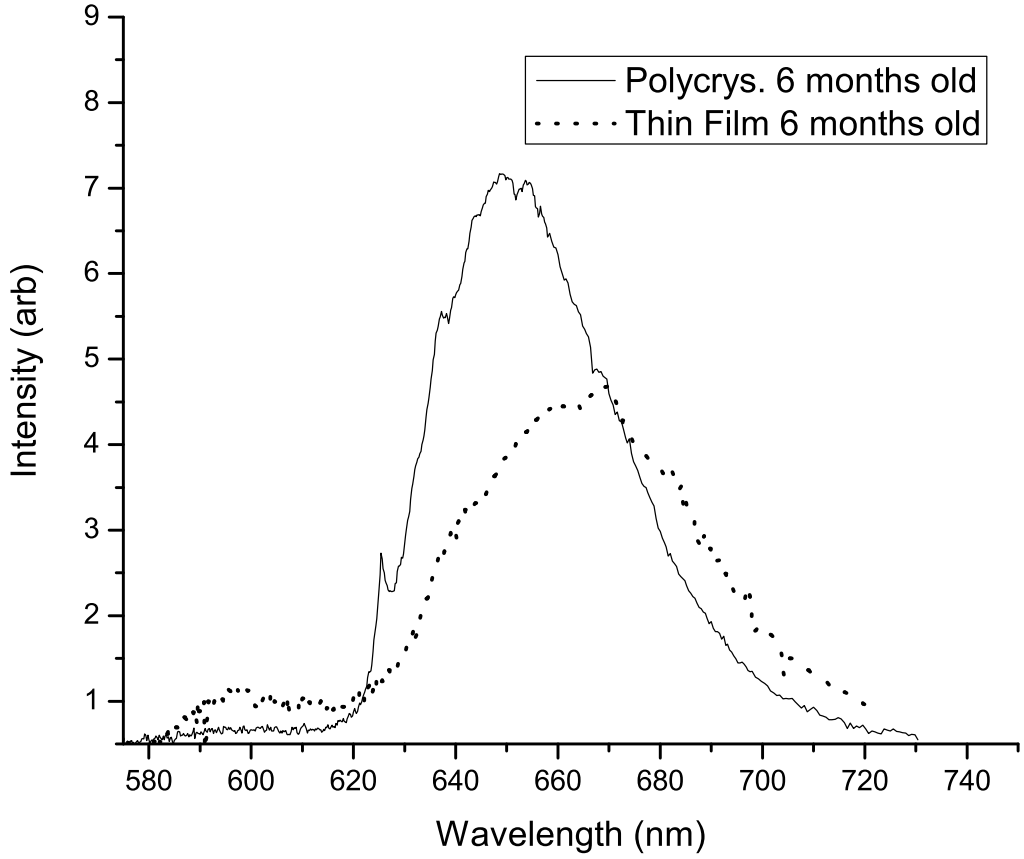

Figure 5.6: CaS:Eu,$MgCl_2$(1%) 6 months old micorparticles and thin films LIFS comparison. The vibronic band of the thin film is clearly shifted approximately 10nm towards the low energy side of its spectrum. Similar effects were observed for the case of MgS:Eu,$MgCl_2$ thin films.

ions to go near Eu^{2+} sites in this material. In other words, figure 5.5 suggests that the concentration of Mg^{2+} ions is significantly higher near Eu^{2+} sites in the lattices of these thin films. This inhomogeneities in concentration may be due to strain energy minimization during their growth. Higher concentration of point defects may create strain in certain regions of the films that can favor relaxation through a mechanism of anisotropic diffusion[29].

Similar results were obtained for the same films when their spectra was recorded after long-term storage, see figures 5.7 and 5.8. For example, in figure 5.7, the spectrum of the 0.06% mol $MgCl_2$-doped CaS:Eu thin film taken after 6 months of its deposition is shown and compared to the spectrum of the same film recorded one day after its deposition. This graph reveals dramatic changes in the optical spectrum of the 0.06% sample. For instance, the ratio of the MgS:Eu integrated emission intensity to the CaS:Eu integrated emission intensity in this film varies from approximately 1:10 to almost 1:1. This behavior can be interpreted as a slow but preferential migration of Mg^{2+} ions towards Eu^{2+} sites over a long period of time. Moreover, figure 5.8 reveals that although the observed long-term anisotropic diffusion is not as pronounced on the 1% mol $MgCl_2$-doped CaS:Eu films, the effect is still significant and correlates with the results obtained for lower concentrations, *i.e.* 0.06% mol $MgCl_2$-doped CaS:Eu thin films. The graph shows that the ratio of the MgS:Eu integrated emission intensity to the CaS:Eu integrated emission intensity in the 1% mol $MgCl_2$ film varies from approximately 1:25 to almost 1:10. This result is expected since in the 1% mol $MgCl_2$-doped CaS:Eu films the Mg^{2+} ion concentration is significantly higher than the Eu^{2+}'s therefore the creation of the Eu optical centers saturates and becomes less efficient. In addition, higher concentration of Mg^{2+} ions will result in a more homogenous crystal field

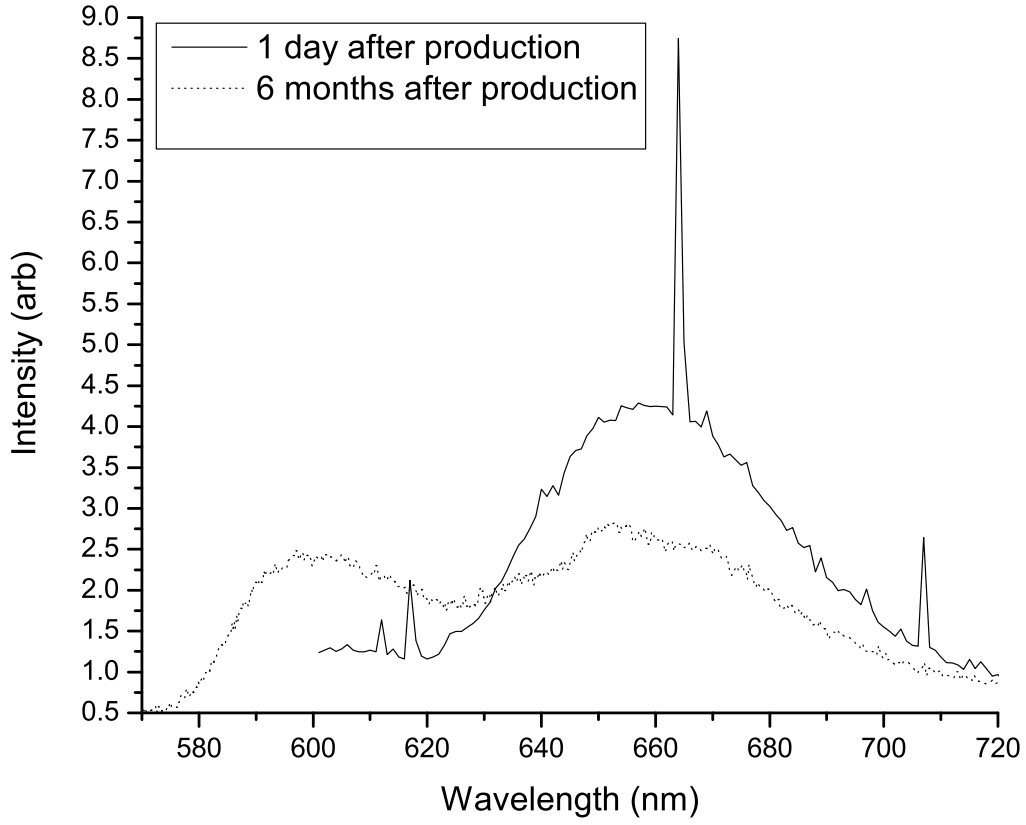

Figure 5.7: CaS:Eu,$MgCl_2$(0.06%) thin films LIFS spectrum comparison. The solid line corresponds to a spectrum taken 1 day after thin film deposition and the dotted line represents the spectrum of the same sample taken 6 months after deposition. The graph shows clear evidence of preferential migration of the Mg^{2+} ions towards Eu^{2+} sites.

environment in the thin films hence the migration probability of impurities and point defects will be correspondingly decreased and, in turn, the optical spectrum of the materials will be less significantly affected.

5.4 MgS:Eu/ CaS:Eu Microparticles

In another set of experiments, a sample consisting of 80% MgS:Eu and 20% CaS:Eu microparicles was prepared for the analysis of its optical spectrum. The purpose of this experiment was to obtain some additional information about the anisotropic diffusion behavior observed in the CaS:Eu,$MgCl_2$ thin films. Given that the data for CaS:Eu,$MgCl_2$ thin films suggested some preferential migration of the Mg^{2+} ions towards Eu^{2+} sites, or vice-versa, changes in the spectrum of MgS:Eu/CaS:Eu could lead to a better understanding of this behavior.

The method used for fabrication of this sample was simply to mix a previously prepared batch of MgS:Eu with another batch of CaS:Eu and heating the mixture up to 800^oC for 8 hours to promote a uniform population distribution of the two materials throughout the sample. A LIFS spectrum of the product was taken and it was then stored in a low humidity environment for 6 months, just as described in the previous section for the CaS:Eu,$MgCl_2$ thin films. After 6 months, another LIFS spectrum of the sample was taken and compared to the spectrum taken 6 months prior. Figure 5.9 shows a comparison between the spectrum of the sample 1 day and 6 months after fabrication. The graph reveals that there was no significant change in the optical spectrum of the material. The only minor difference between the two spectra is that the 6 months old spectrum shows a

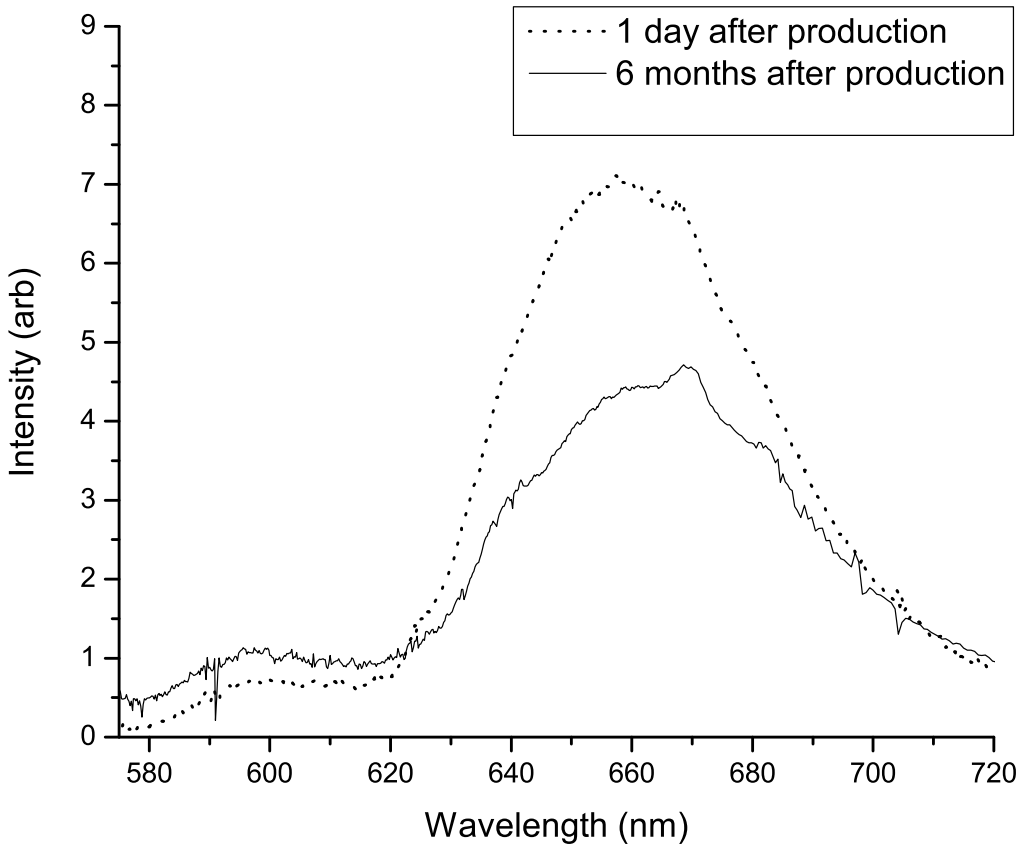

Figure 5.8: CaS:Eu,$MgCl_2$(1%) thin films LIFS spectrum comparison. The dotted line corresponds to a spectrum taken 1 day after thin film deposition and the solid line represents the spectrum of the same sample taken 6 months after deposition.

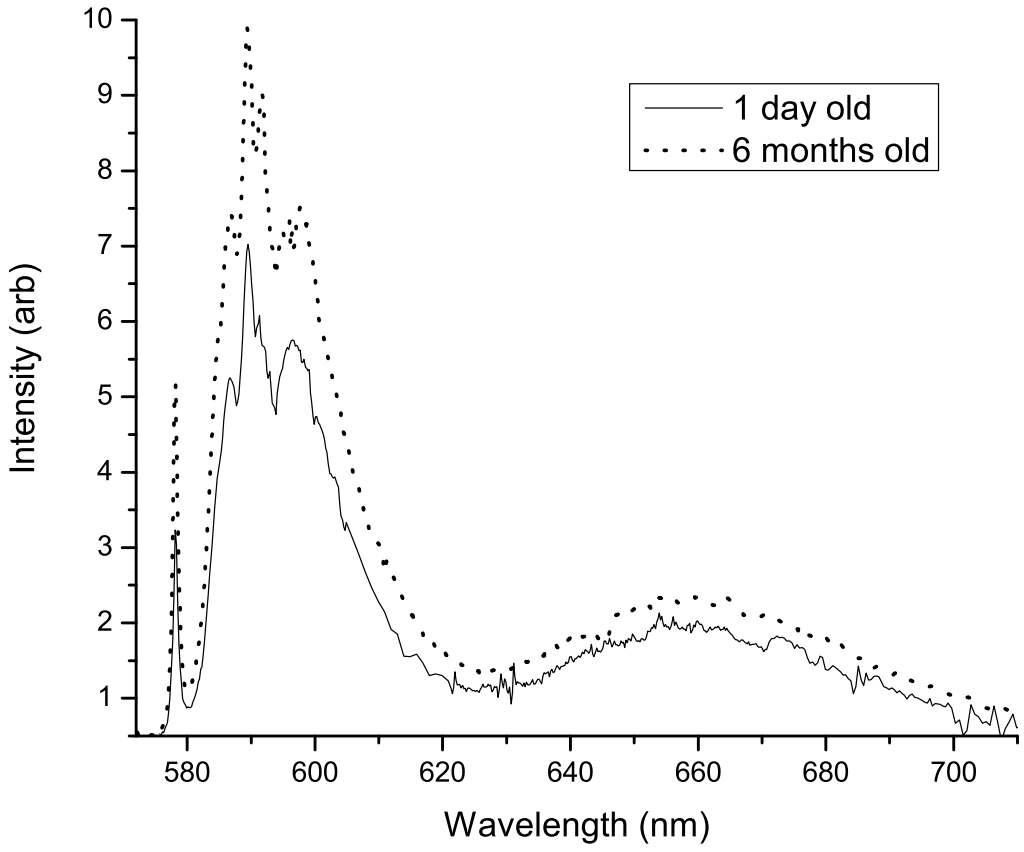

Figure 5.9: MgS:Eu/ CaS:Eu (80%/20%) microparticles LIFS comparison. The solid line corresponds to a spectrum taken 1 day after sample fabrication and the dotted line represents the spectrum of the same sample taken 6 months after deposition. The two spectra do not show much variation in the optical properties of MgS:Eu/ CaS:Eu (80%/20%) microparticles over time.

slight increase, approximately 6%, on its Debye-Waller Factor. That is, the Eu center ZPL became slightly more intense relative to its vibronic band. It shall be mentioned that this type of slight increase in intensity was commonly observed in pure MgS:Eu samples also. This implies that the population distribution of the species in the lattice of MgS:Eu/ CaS:Eu sample remained relatively unchanged 6 months after its fabrication and no structural reordering was observed in this case. This behavior is anticipated. In thin films the growth is quenched condensed and therefore diffusion would be allowed through long term relaxation of a system which is in a non-equilibrium state. On the other hand, in microparticles that are synthetized at high temperature over a long period of time, all strains are relaxed and diffusion reaches an equilibrium state, or a state in which the net diffusion is zero. This is an important finding since it suggests two things; 1) the crystalline nature of the microparticles does not favors anisotropic diffusion and 2) as mentioned earlier, the existence of Mg^{2+} inside amorphous CaS:Eu thin films can favor the creation of point defects throughout the thin films and this in turn can promote preferential optical center migration through some mechanism related to this formation of point defects or vacancies.

It shall be mentioned that although it is still possible that Cl plays a role in the formation of point defects during the PLD growth of amorphous thin films, it is also likely that it tends to migrate preferentially towards the surface of the material during its fabrication and maybe eventually evaporate from it. This has been reported in similar systems by V. Consonni *et al* [30]. In their experiments, they found significant increase in concentrations of Cl residing at the grain boundaries of annealed Cl-doped CdTe microparticles when compared to the same samples before annealing. Furthermore, they found that the total concentration of Cl on

their samples was 20% lower on the annealed samples. This correlates with this work's results of no significant changes in the optical properties of MgS:Eu,$MgCl_2$ microparticles compared to MgS:Eu's and implies that the changes observed in the optical properties of the other $MgCl_2$-doped materials was unrelated to Cl-doping.

CHAPTER 6

OPTICAL STUDIES OF ZnS:Eu AND ZnS

Although not an optically active component of the multilayer thin films studied here, the ZnS capping/ barrier layers were an integral part of their architecture and were essential in preserving the integrity of the optically active thin films and, in turn, its optical properties . The MgS:Eu and CaS:Eu materials are both highly hygroscopic therefore readily absorb water molecules when exposed to air. Hence, capping the produced thin films with a layer of ZnS would isolate these materials from the environment and protect them from species that would otherwise come in contact with them and possibly promote unwanted compositional changes. Furthermore, being a sulfide, ZnS doesn't introduce unwanted cations in the films. The ZnS thin films would at the same time create an interfacial barrier between two layers of different materials thereby preventing the inter-difussion of corresponding species from migrating from one layer to the other hence avoiding degradation of the materials. Also, the bandgap of ZnS (Eg = 3.7eV) is large

enough to allow access of the read and write laser beams in the required orange-red region (E $\sim$ 2eV) when performing PSHB experiments. In addition, the ZnS thin films lattice constant and lattice structure are very similar to both MgS's as well CaS's and therefore it tends to promote stoichiometric growth among successive layers of these materials. Finally, its high refractive index is comparable to the index of the other optically active layers (MgS: 2.27, CaS: 2.14, ZnS: 2.37) therefore reduces the internal reflections within the structure.

In addition to the ZnS layer studies, some effort was put into the synthesis of ZnS:Eu and the study of its optical properties with the intention of evaluating its potential for use in spectral storage applications. This chapter will present a brief discussion on the fabrication of ZnS:Eu and its optical properties. However, most of the chapter focuses on systematic studies of the optical properties of the ZnS capping layer and the effects that slight variations of PLD growth parameters have on these properties.

6.1 ZnS:Eu Thin Films

Although the study of ZnS:Eu thin films had not been part of the original agenda of this work, the idea of finding this system suitable for PSHB was very appealing. Being that the host matrix of the system is the ZnS lattice would very likely make compatibility issues with the capping layer and the optically active sulfides discussed in previous chapters practically non-existent. At the same time, it would provide yet another layer in which PSHB could be performed thereby increasing the storage capacity attainable by a multilayer device made out of these

materials. In addition, the fabrication process of ZnS:Eu is essentially the same as with the other Eu-doped sulfides so the manufacturer is saved from any need of incurring in additional investments, *i.e.* infrastructure and knowledge base development.

One factor to consider was that even though electroluminescence in ZnS:EuF_3 thin films is a well studied and documented phenomena, studies found in the scientific literature in which only Eu had been doped into ZnS reported no fluorescence emission[31]. However, the Eu-doped ZnS experiments found in the literature were conducted for microparticles systems only. This is an important point since plenty of cases have been cited in scientific literature, including this work, in which PLD produced thin films significantly differ in optical properties when compared to the same material in the form of microparticles and nanostructures. Moreover, some research groups have reported that ZnS nanostructures do emit light in the visible range [32, 33]. On their nanoparticles, the bandgap of the host increases with decreasing nanoparticle size due to confinement effects. They claim that the intrashell excited states of the Eu ion are degenerate with the conduction band continuum in microparticles. However, confinement brings the electronic transitions of the luminescent center within the bandgap of the ZnS nanoparticle thus resulting in emission of the optical center.

For those reasons, experiments on the optical properties of ZnS:Eu thin films were found to be of importance and therefore were incorporated into this investigation. A comparison between the spectrum of ZnS:Eu at 18K and at room temperature is shown in figure 6.1. In the graph, the intensity of the emission signal is very weak when compared to MgS:Eu and CaS:Eu thin films. The emission lines are very sharp and match each other very well on both spectra indicating

that the observed spectral features do not belong to the ZnS:Eu thin films but come from laser plasma lines. In fact, both spectra are almost identical to the laser plasma spectrum shown in the previous chapter, see figure 5.3.

In other words, no luminescence was observed from the ZnS:Eu thin films. This suggests that the energy scheme of the Eu ions inside the ZnS:Eu lattice of thin films made via CCPLD is possibly very similar to the case for ZnS:Eu microparticles. The Eu^{2+} excited state transition in particular lies in the conduction band and electron recombination does not yield luminescence in the visible range.

6.2 ZnS Capping Layer

Due to the importance of the ZnS capping layer, special attention was given to the study of its optical properties and the effects that variations in the CCPLD growth parameters had in them. Also, as part of similar experiments, results were obtained that suggest that the bandgap of ZnS thin films is shifted significantly towards lower energies as their thickness increases when grown via CCPLD. This implies that in some cases significant absorption from capping and barrier layers could occur and, in turn, increase the photon budget for reading and writing the optical information in PSHB technique. In addition, excessive absorption may cause heating of the medium, resulting in broad spectral holes and hence poor storage density. As a result, control of the thickness is also an important aspect of CCPLD thin film production. A linear increase of the band gap with reducing the sample thickness suggests that one could use very thin films to ensure a large bandgap. On the other hand, a layer too thin could make diffusion easier or even

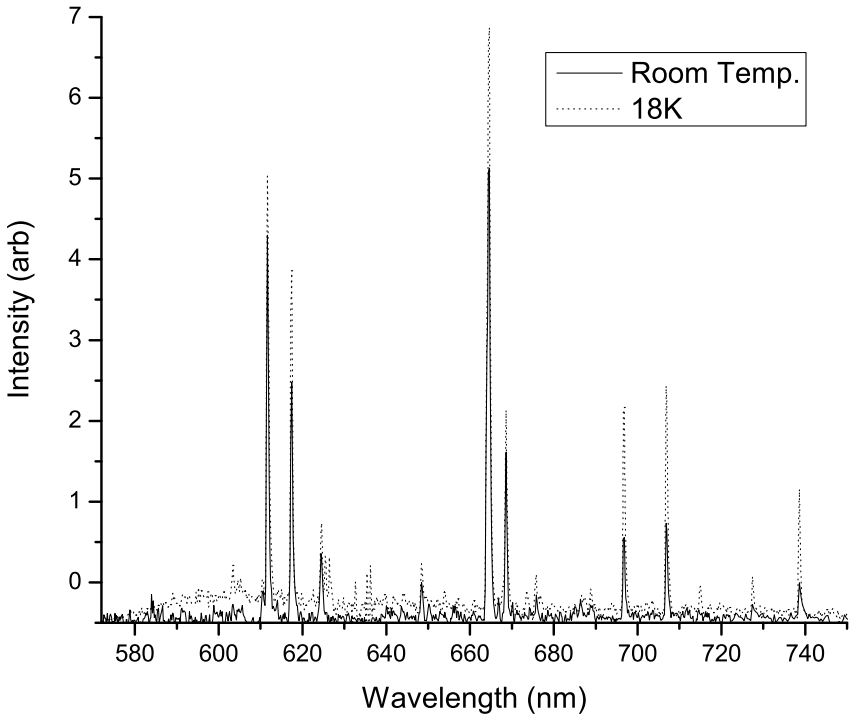

Figure 6.1: ZnS:Eu microparticles LIFS spectrum comparison. The dotted line represents the spectrum of the sample at 18K and the solid line at room temperature. The two spectra are largely the same suggesting that the observed sharp spectral lines correspond to laser plasma lines. Moreover, the two spectra are very similar to the spectrum taken with no sample across the laser beam beam path shown in figure 5.3.

react with the environment if there are nano-pores or structural defects in the film.

6.2.1 Optimization of Deposition Parameter

For any PLD of different material, a completely new set of deposition parameters has to be established. This will be necessary for predictable and reproducible growth. As ZnS is different from the materials previously deposited in thin film form, systematic studies on the effects of different PLD process parameters were conducted in order to achieve the best results possible. As a result, we found that variations of the partial pressure and the composition of the chemically controlled environment inside the chamber resulted in significant changes in the quality and durability of the thin films. For example, by performing PLD deposition at different vacuum pressures ($8.6X10^{-7}$Torr - $1.2X10^{-2}$Torr) or performing it under different chemical environments (400mTorr-500mTorr He instead of H_2S) produced ZnS thin films with different characteristics than the films produced at 500mTorr H_2S partial pressures during the rest of this work . The thin films made under high vacuum would often be "flaky" , brittle and would easily break into pieces when taken out of the PLD chamber. The thin films made under an He environment were relatively transparent but would frequently grow very non-uniformly. The best results in this case were obtained for thin films made under partial pressures of 500mT He but even those film would show rather non-uniform grow around the edges.

It is worth mentioning that 500mTorr H_2S appeared to be the optimal conditions that consistently gave the best results. This is also true for the experiments

in which H_2S's partial pressure was varied from 200mTorr to 800mTorr. There, the thin films made at a partial pressure of 200mTorr would turn out hazy (less transparent) and sometimes would be brittle and chip off at certain parts in the films. The cases for 600mTorr H_2S and higher partial pressures would produce thin films very hazy and yellowish in color. Although higher pressures consistently appeared to give durable samples when first examined, most of this films would tend to crack and chip off from the substrate several days after being removed from the deposition chamber and stored in a de-humidified environment.

6.2.2 ZnS Thin Films Bandgap Energy and the Absorption Spectrum

Calculations of the bandgap energy of a solid-state material are often very difficult, especially when dealing with amourphous materials. In fact, this is not surprising since the absence of long-range order leaves crystalline momentum $\hbar\mathbf{k}$ undefined and renders Bloch's theorem inapplicable. However, LIFS and other experimental techniques have proved that, just as crystals, the electronic states of amorphous solids fall into bands separated by energy gaps [36, 37]. Figure 6.2 compares schematically the density of states (DOS) N(E) between a crystal and an amorphous system. From this illustration we can see three features that are different in amorphous materials; 1) the sharp band edges and tailing of the DOS into the gap. 2) the localization of some energy states in regions where the DOS is low. 3) the existence of broad bands of defect levels in the gap through which hopping conduction may occur.

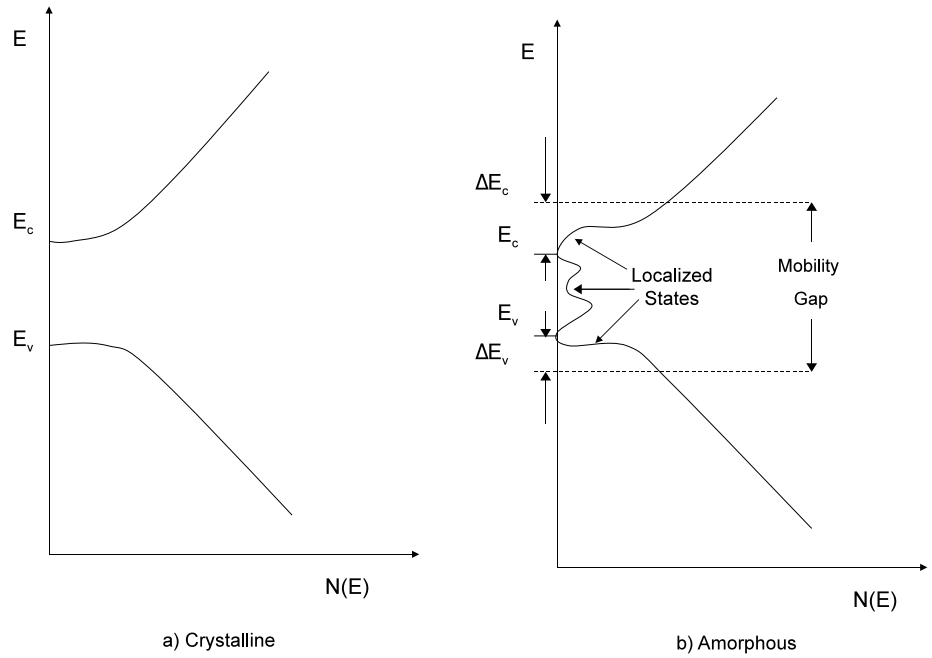

Figure 6.2: DOS N(E) vs. E diagrams for a) crystalline and b) amorphous semiconductors. For the amorphous case, states in energy regions of low DOS tend to be localized. ΔE_C and ΔE_V are band tails arising due to disorder.

The form of the optical absorption edge in ZnS thin films is illustrated schematically in figure 6.3. This diagram separates three different regions in the absorption spectrum of a ZnS film. Each region is defined by specific features in the spectrum that are determined by the density of states within the mobility gap of the sample and arise from the variations in the crystal field throughout the solid [38].

The low absorption region of the spectrum (Region C on figure 6.3) shows an exponential decay proportional to the absorption coefficient α of the material and

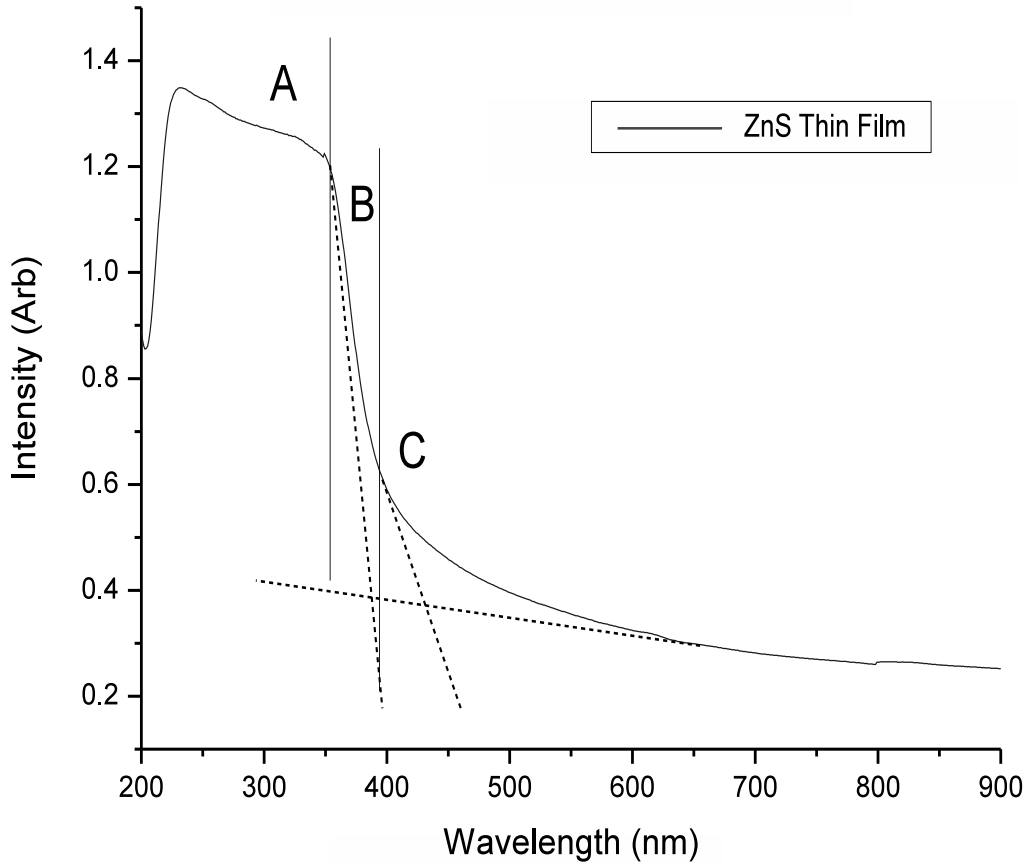

Figure 6.3: Main regions of optical absorption in ZnS thin films. Region A corresponds to strong absorption wavelengths of the film, region B lies around the bandgap and region C corresponds to weak absorption wavelengths. The dashed lines are extrapolations of the curves in regions A, B and C defined by Equations 6.3, 6.2 and 6.1, respectively.

can be described by the equation,

$$\alpha \sim e^{\frac{E}{E_t}} \tag{6.1}$$

where E is the photon energy. This region arises from transitions involving defect states within the bandgap. This region is usually very sensitive to the structure of the sample under study [39].

At higher energies (Region B), α shows an exponential tail that can be written in the form,

$$\alpha \sim e^{\frac{E}{E_u}} \tag{6.2}$$

This region is usually known as the *Urbach* region. It corresponds to absorption involving one or both tails of localized states near the conduction and valence bands and additional broadening is expected from potential fluctuations due to charged defect states and phonon vibrations. The exponential factor E_u indicates the width of the band tails of the localized states and is always smaller than the factor E_t characteristic of Region C.

In the strong absorption region (Region A), α can be described by the equation,

$$E\alpha \sim (E - E_g)^n \tag{6.3}$$

where E_g is the optical bandgap energy and the constant n is equal to $\frac{1}{2}$ for direct allowed transitions such as ZnS's [40]. Equation 6.3 is only semi-empirical since it is not based on a rigid theoretical model. In other words, E_g deduced from experimental data is a vague parameter that has no clear physical meaning. However, its variation with fabrication conditions conveys very valuable information about

the material studied [41].

In an attempt to ensure consistency and validity of results throughout this experiments, the value of E_g was measured for each ZnS thin film made by careful analysis of their corresponding absorption spectra via three different protocols. First, the E_g value of the films were measured by printing a hard copy of the spectrum, as large as possible, and tracing a straight line starting from the end of Region A (strong absorption region) and following smoothly the beginning of the fall of the absroption decay in Region B, see figure 6.3. Another straight line is then traced from the beginning of Region C (low absorbance region) following smoothly the sample's absorption spectrum until the trace intersects with the line previously drawn coming from Region A. The x-axis value at the intersection point of these two lines was taken as the measured value for the bandgap energy of the sample. In a second method, the midpoint between the absorption maximum of the thin film spectrum and the zero-absorbance value was taken as the E_g value of the sample. The third and most empirical method consisted in using computer fitting software to extrapolate to $\alpha^2 = 0$ in the plot of a $(E\alpha)^2$ vs. E graph for each sample. That is, at $\alpha^2 = 0$, $E = E_g$ [42]. Here, α is calculated by using the relation, $\alpha = 2.303A/t$, where A is the absorbance of the film and t is its thickness [43].

The use of all three methods for obtaining the experimental E_g value of the thin films resulted in a proportional change in measured values when comparing results from one method to the other. However, variations were constant among all values measured. For example, when using the method of extrapolation of the $(E\alpha)^2$ vs. E graph, all E_g values obtained would shift approximately the same magnitude when compared to the values obtained using the other graphical analyses. This

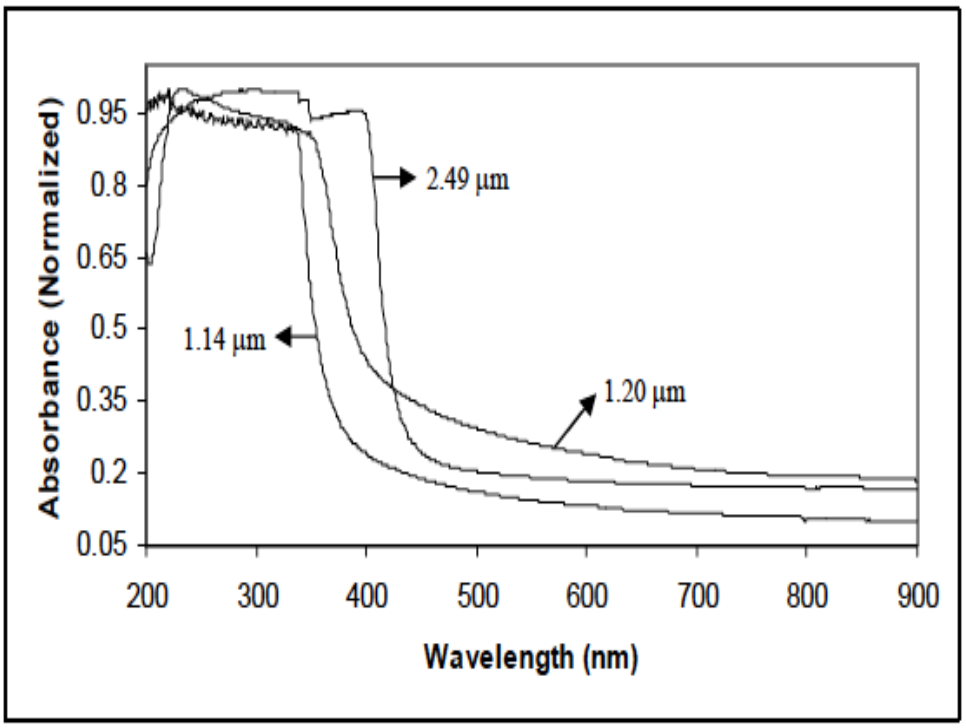

Figure 6.4: ZnS thin films absorption spectrum of three different samples. The graph shows a shift in the bandgap of the film with changes in thin film thickness. The film of thickness 1.14μm has a larger bandgap than the 1.20μm film and the bandgap of the 1.20μm film is larger than the band gap of the 2.49μm film.

fact provided some validation to the findings of energy gap shifting with changes in thin film thickness since the ratio of change in energy to the change in thickness remained essentially the same, independent of the method used to measure the bandgap value of the films.

6.2.3 Bandgap Shift

As stated in the previous section, the results of the ZnS thin films studies suggest that their bandgap was found to gradually shift towards lower energies as

a function of the thickness of the films. This results should then be taken into account in during deposition of the thin films in addition to the recently reported results by M. K. Morozova *et al.* on the effects of temperature and pressure on the bandgap of ZnS [44]. Figure 6.4 shows the shift in E_g of three different ZnS thin films and their corresponding changes in thickness. Region B of the thin film with thickness 1.14μm lies furthest to the left of the graph, towards higher energies, indicating that the E_g value of this film is the largest among the three films. Similarly, Region B of the 1.20μm thin film lies in between region B of the thin films with thicknesses of 1.14μm and 2.49μm, corresponding to an intermediate E_g value.

The values obtained for the measured E_g of each sample were used to plot a ΔE_g vs. thickness graph, where $\Delta E_g = E_{bulk} - E_g$ and E_{bulk} is the bandgap of ZnS in bulk, see figure 6.5. Although there is no difference between the slope of a ΔE_g vs. thickness graph and a E_g vs. thickness graph, a ΔE_g vs. thickness graph allows for a direct comparison to theoretical models describing bandgap variations due to confinement effects in later analyses. A close look at figures 6.4 and 6.5 reveals two types of changes; 1) the shift of the bandgap towards lower energies with higher thicknesses. 2) the extension of the band tail in the low energy range of the thin films. As mentioned in the previous section, the latter effect can be due to the creation of absorbing centers or defect states near the bandgap. One possible source of such defects could be the deficiency of sulfur in the samples or the presence of some other trace impurities. It is worth noticing that the samples grown were compared under different concentrations of H_2S in the chamber but no correlations between the new centers and sulfur deficiency could be clearly established. However, although the purpose of using small amounts of H_2S during thin

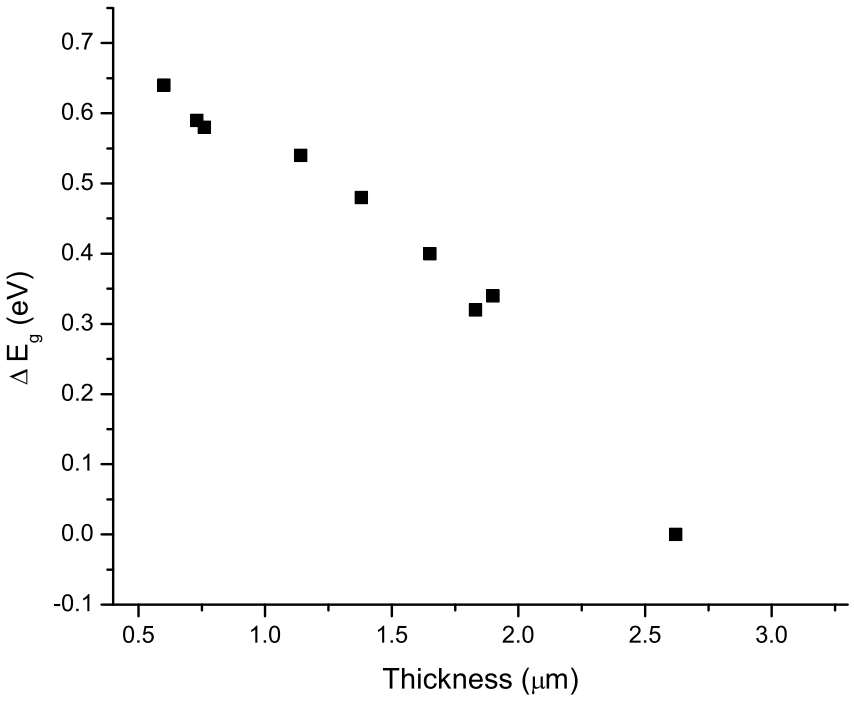

Figure 6.5: ΔE_g vs. thickness plot for ZnS thin films. The change in bandgap ΔE_g decreases with increases in thickness of the films.

film deposition is to avoid sulfur-deficient growth, these defects are still possible and their existence should not be ruled out.

A possible cause for the increase in the bandgap of the thin films may be quantum confinement effects. If the films are nano-compacted, rather than being continuous films of uniform density, such effects could still play a role. In addition, in the case of thin film semiconductors the film thicknesses at which confinement effects become observable are significantly larger than in the analog case for metals where their relatively large Fermi energies result in confinement effects only observable for thicknesses of the order of 10^{-8}cm to 10^{-7}cm [45]. Given that the

effective mass of the charge carriers in semiconductors are usually of the order of $m_{eff} \sim 10^{-2} m_0$, their wavelength,

$$\lambda \sim \frac{h}{\sqrt{2 m_{eff} kT}} \tag{6.4}$$

will be of the order of $\lambda \sim 10^{-5}$cm at T $\sim$ 100K. It may be worth noticing that quantum effects may still be masked due to carrier scattering at the film boundaries which is diffuse in the classical limit.

It follows from the uncertainty principle that, irrespective of the details of the energy spectrum, the continuous spectrum for thin film semiconductors should be shifted by,

$$\Delta E_g \sim \frac{\hbar^2}{2 m_{eff} t^2}. \tag{6.5}$$

where again, t represents the thickness of the film. This should appear in the spectrum of a thin film as an increase in the bandgap with decrease in thickness[46]. However, the nature of Eqn. 6.5 does not correlate with the results obtained for the shift in bandgap of the ZnS thin films under this study. By looking at Equation 6.5 more carefully, one can see that the energy shift due to confinement is inversely proportional to the square of the thin film thickness. The results in figure 6.5 shows a linear relationship between these two quantities.

It is also possible that the bandgap shift observed is related to scattering effects occurring during the measurement of the optical spectrum of the films. If the value of the rms roughness of a film is σ, then we can use the Kirchhoff diffraction integral

to calculate the reflectivity of its rough interface by,

$$R_s = R_0 exp\left[-\left(\frac{4\pi}{\lambda}\sigma n_0\right)^2\right] \tag{6.6}$$

where n_0 represents the index of refraction of air and R_0 the reflectivity of an ideally smooth surface of the material. Similarly, the transmission scattering loss can be expressed by,

$$TSL_t = T_0\left\{1 - exp\left[-\left(\frac{2\pi}{\lambda}\sigma(n_1 - n_0)\right)^2\right]\right\} \tag{6.7}$$

where T_0 is the transmittance of an ideally smooth interface and n_1 is the refractive index of the dielectric. After analyzing Equations 6.6 and 6.7 it becomes clear that the surface morphology of the thin films plays a role on their optical transmission, especially at shorter wavelengths. Thin films with higher values of roughness σ will decrease the amount of light transmitted which will in turn increase the bandgap energy [47].

It should be mentioned that the process used to fabricate the thin films for this study has been optimized to achieve the best quality films possible as defined by the various requirements imposed by the multilayer storage devices that they are grown into. Those deposition parameters will not necessarily produce the most ideal systems to be used for a study designed to establish a relationship between bandgap and thickness in a clear manner. For example, the thickness of the thin films produced was often somewhat flat but never perfectly uniform throughout the films. They typically were slightly thicker near their center and thinner around the edges consistent with theoretical models for PLD and experimental results for

other materials [48]. Conducting a more rigorous study of the relationship between energy gap and thin films thickness would require changing the experimental procedures for film production. However, the purpose of our study was to characterize the optical properties of the capping layers of the Eu-doped sulfide PSHB systems. Further studies on the relationship between bandgap energy and thickness of ZnS thin films grown via CCPLD may be necessary before a final conclusion can be reached.

CHAPTER 7

SCANNING ELECTRON MICROSCOPY

Morphology is an important factor to consider in the study of any type of thin film. The morphological information can prove very useful in establishing correlations between thin film structure and its properties. In fact, the morphological structure of a sample, particularly at nanoscales, can largely affect its optical properties as discussed in the previous chapter. In a similar way that a polycrystalline sample will show some differences in its optical spectrum when compared to a thin film of the same material, a thin film with uniform lattice structure will show a different spectrum when compared to a thin film with less uniform lattice structure. The latter, for example, could be the case encountered when dealing with nano-compacted thin films.

We used SEM and profilometry techniques during this investigation in an attempt to gain a better understanding of the physical properties that determine the optical properties of the thin films produced. We selected a few samples out of

each type of thin film made and looked at them "under the microscope" to characterize their morphological properties individually. The information obtained was very useful and shed new light into the properties of the structures studied. This chapter describes those findings and their effect on the properties of the systems investigated.

7.1 ZnS Capping Layer Morphology

The first type of films studied were the ZnS thin films. As mentioned in the previous chapter, although not an active component of the thin films under study, they were still an integral part of these systems and played a mayor role in maintaining the integrity of the inner layer materials and their composition. A SEM image showing the morphology of the ZnS thin films can be seen in figures 7.1 and 7.2.

Figure 7.1 corresponds to a ZnS capping layer thin film, on an MgO substrate, at a magnification of 2000X. The picture on the left provides a top view of the sample and the picture on the right a tilted view. The surface morphology of the left picture appears smooth, for the most part, with some areas showing minor protuberances and inhomogeneities in its the surface. This protuberances, however, appear more pronounced and some of them even larger on the tilted view picture. In here, the protuberances, or mounds, appear to be areas in the thin film in which the material has agglomerated more significantly and promoted a more vertical growth when compared to the conformal growth of the rest of the surface. The side of the thin film in the tilted view picture appears rough and of irregular

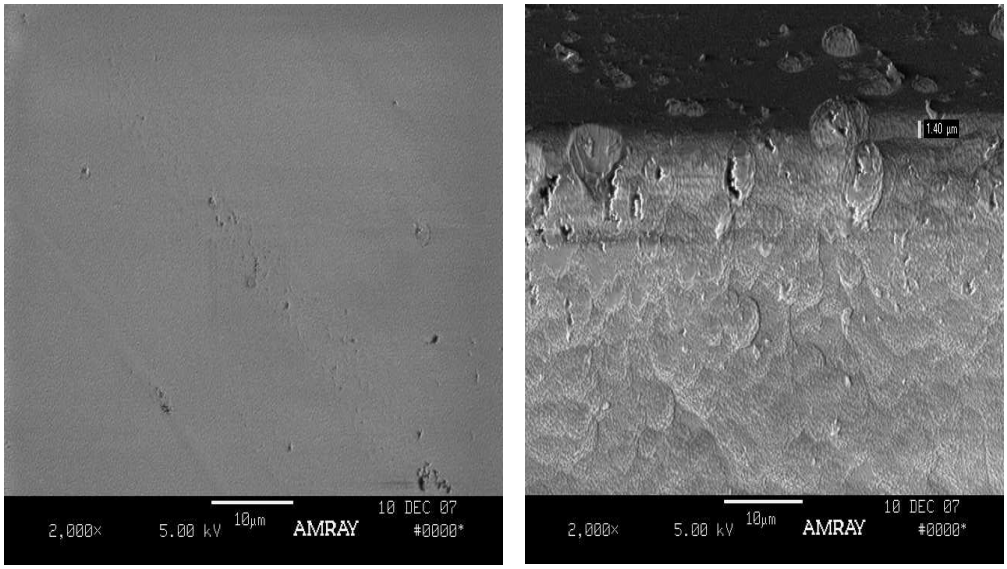

Figure 7.1: 2000X SEM images of a ZnS thin film on a MgO substrate. The image on the left corresponds to a top view scan of the film and the image on the right to a tilted view. the surface morphology of the sample appears smooth but shows some minor protuberances and inhomogeneities throughout the surface.

growth. This may be due to the irregular surface at the edges of the substrate. As explained in chapter 3, the MgO substrates are usually cut into smaller pieces to maximize their use and this causes some of their sides and edges to become very irregular after being cut.

Figure 7.2 shows the same film displayed on the previous figure at magnifications of 5450X on the left picture and 15000X on the right. The left picture provides a tilted view of the ZnS thin film and the right one a top view. In the tilted view, the same mounds seen in the previous picture appear larger and better resolved. Their sizes vary from approximately 1μm to around 10μm. Again, they look like clusters of smaller formations agglomerated together in dome-like structures resembling mounds. The picture on the right, with a magnification of 15000X, shows a smooth surface of the thin film around what appears to be a nanosized gap formed by the lack of deposited material near that area. The ZnS layers of the thin film doesn't seem to have grown conformably and uniformly in this area, approximately a few hundred nanometers across. It is not clear from the picture how deep these nanogaps are in some locations and whether or not they run along the growth axis all the way down into the substrate. This was an important finding because it is critical that the ZnS layers of the thin films grow conformably and continuously along its surface in order to protect and isolate the MgS:Eu and CaS:Eu thin films from the outside environment. An experimenter conducting similar experiments should keep this in mind and take extra precautions to avoid the creation of these nanogaps before and/ or during thin film deposition.

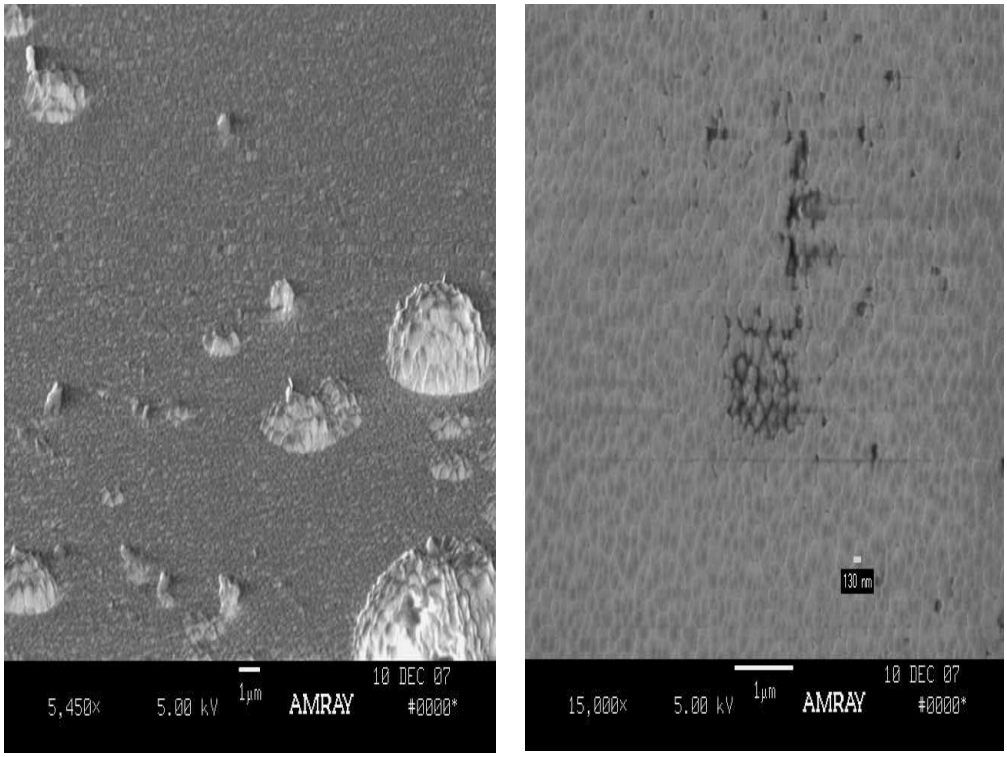

Figure 7.2: ZnS thin film SEM images. The image on the left corresponds to a tilted view with magnification 5000X and the image on the right to a top view with magnification 15000X. On the left, mound areas can be observed throughout the surface of the film. On the right, nanosized gaps show up where the ZnS thin film apparently did not grow conformably and the ZnS material may not completely covers the surface of the substrate.

7.2 MgS:Eu Thin Film Morphology

Given that all MgS:Eu thin films produced during this study were capped with a ZnS layer for protection, the MgS:Eu material could never be imaged directly. The images presented in this section are all indirect images of the MgS:Eu layers mapped through direct imaging of the ZnS layers capping them. Although this might not be the most efficient method of obtaining concise information about the morphology of the MgS:Eu layer, it offered very valuable details about their morphology and structure.

In contrast to the predominantly smooth surface displayed by the ZnS thin films in the previous section, the MgS:Eu thin films showed a very irregular and significantly rougher surface morphology, see figure 7.3. Their surface showed bumps or mound formations all across the thin film and even a relatively larger concentration of nanogaps, similar to the ones described in the previous section. Figure 7.3 shows an MgS:Eu thin film at magnifications of 2000X on the left picture and 1320X on the right. The left picture provides a top view of the thin film and the right one a tilted view. The dimension of the irregularities displayed by the thin film seem to range from hundreds of nanometers in size to more than 10μm in some cases. From the tilted view picture, image on the right, a similar non-uniform growth morphology can be observed. Figure 7.4 is an image of the same MgS:Eu thin film just decribed, this time at a magnification of 5000X. The picture gives a better resolved view of the features of the film. It shows that the now micrometer size mounds are really groups or agglomerations of smaller formations, generally around tens of nanometers in size. In the picture nanogaps can also be observed. In particular, it might be worth noticing the larger nanogap lo-

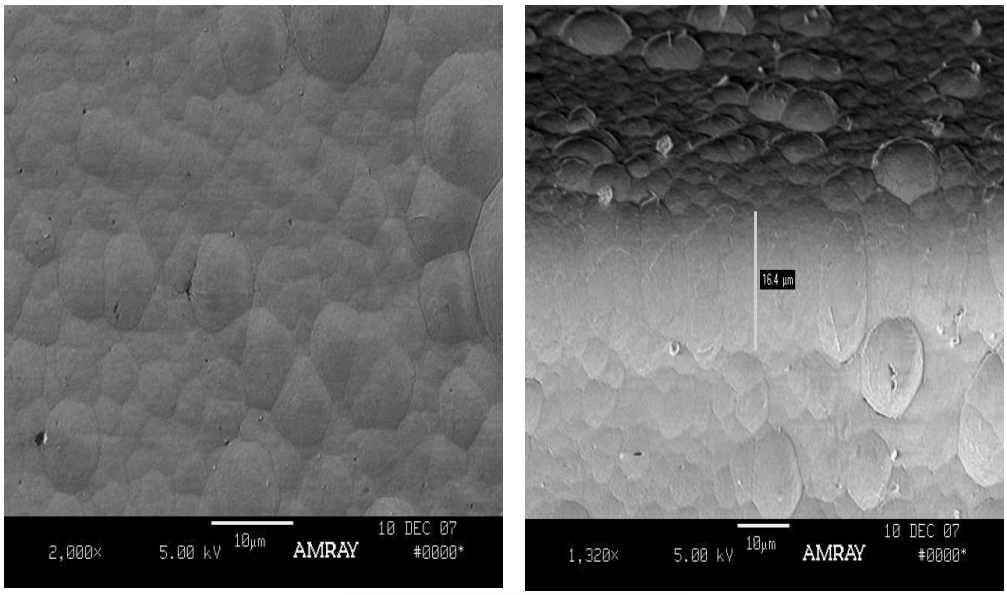

Figure 7.3: SEM images of a ZnS capping layer grown on top of a MgS:Eu thin film. The picture on the left corresponds to a top view at a magnification of 2000X. The picture on the right corresponds to the same sample scanned on a tilted view at 1320X. Cauliflower-like mounds can be observed across the surface of the film. The height of the mounds is more easily appreciated on the tilted view. The side of the film also shows this type of growth.

cated at the mid-left section of the image, dividing three larger mounds of material that would otherwise be displaying a clearly defined interface between them.

The formation of these irregularities along the surface of the MgS:Eu thin films can be caused by several reasons. One reason could be that the nanogaps appearing at the surface of the films are deep enough to allow water molecules to seep through them and eventually be absorbed by the MgS:Eu material. Being that MgS:Eu is highly hygroscopic, it will readily absorb any water molecules that it comes in contact with and this will in turn change the chemical composition of the material. This phenomena may cause the new material to expand and create bulges on the surface of the thin films that may appear as mounds. Another very possible explanation could be that the morphology observed in these thin films could be an inherent result of the CCPLD techniques used to produce them. That is, PLD processes with low adatom mobilities ($T/T_m \lesssim 0.3 - 0.5$, where T is the thin film temperature and T_m the material's melting temperature and with the limit growing lower with bombardment-induced mobility) will result in thin films of similar morphologies to the ones produced here. Given that these thin films were deposited at 550^oC, they are still well below the limit for low adatom mobility growth [49, 50] therefore can very likely experience similar growth conditions and exhibit such behavior.

This phenomena is described in great detail by Messier [51]. According to this explanation, as soon as incoming particles adhere to the surface of a thin film substrate they experience low mobility, are only free to move 1 - 3 atomic positions ($\lesssim$ 1nm) and form nanometer-sized disordered clusters. These clusters then form the building blocks of columnar thin film growth that evolves vertically in a cone-like manner. This columnar thin film growth has the characteristic of resulting in

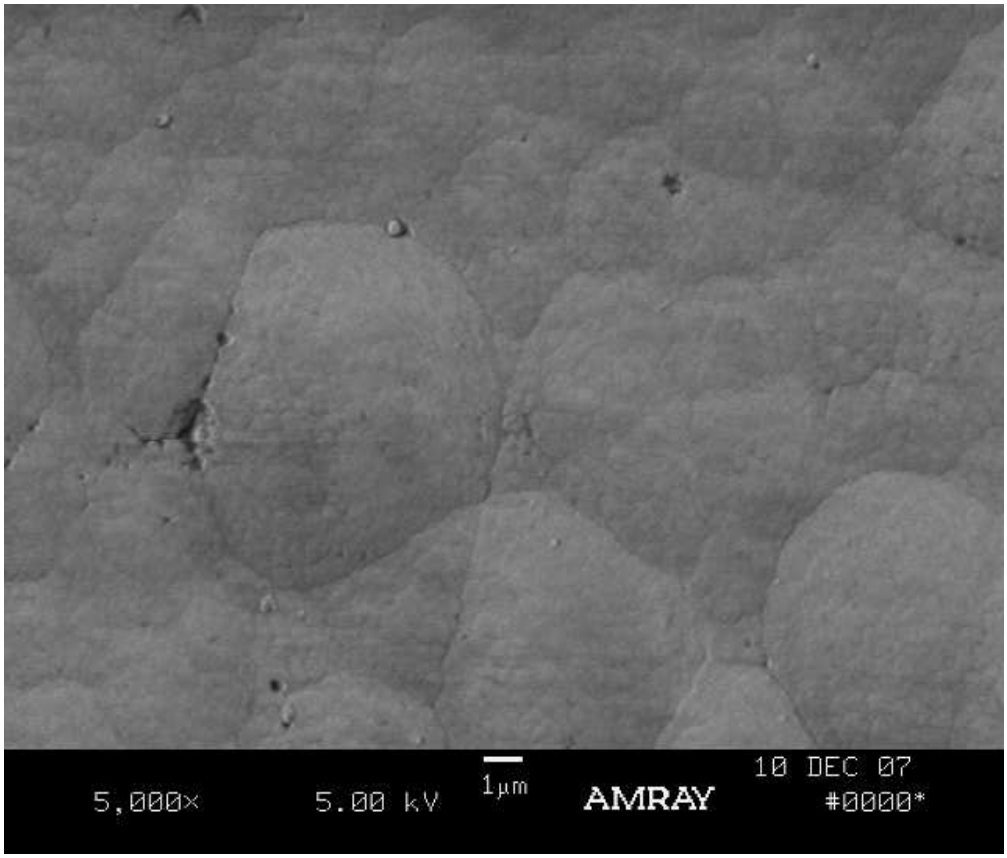

Figure 7.4: SEM images of a ZnS capping layer grown on top of a MgS:Eu thin film at a magnification of 5000X. *Nodular Growth* is evidenced throughout the surface of the film. A nanogap of significant size can be seen around the center-left portion of the image.

a thin film surface covered with what appears to be cauliflower-shaped mounds of various sizes. This is known as *nodular growth*. Nodular growth also becomes more predominant when in addition there exist inherent high bombarment-induced mobilities, very characteristic of CCPLD. In the reference mentioned above, Messier provides electron microscopy images of some of the different morphologies observed in thin films grown under similar conditions to the ones produced during this work. Some of these images show great resemblance in morphological properties to the images obtained from our thin films. These images were taken for materials such as hydrogenated amorphous Si, amorphous Ge and pyrolytic graphite therefore we conclude that this is more likely a general phenomena observed in CCPLD of thin films rather than a special case for our samples.

CHAPTER 8

CONCLUSIONS

This thesis presents a systematic study on the fabrication of MgS:Eu and CaS:Eu doped with various additional impurity ions, their subsequent production in thin film form and the careful characterization of their optical and morphological properties. All the experiments were conducted within a context of evaluation of their suitability for spectral storage applications in the future. The most important finding during this studies can be summarized as follow:

1) Doping MgS:Eu with low concentrations of HCl promoted the creation of O-associated EU centers throughout our thin films thus shifting the spectral position of the material's ZPL to lower energies. This can be caused by the reaction of HCl with adsorbed traces of water molecules at the walls of the CCPLD chamber. O^{2-} ions in water diffuse into the thin films and change the crystal field environment around the Eu^{2+} ion, varying its 4f-5d energy level splitting and changing the energy of the electronic transition. This ZPL spectral shift has potential for application in ultra-high density spectral storage.

2) Doping CaS:Eu with low concentrations of O^{2-} promoted the creation of

O-associated centers throughout the thin film lattice thus shifting the spectral position of the material's ZPL to lower energies. The O^{2-} ions diffuse into the thin film lattice and changes the crystal field environment around the Eu^{2+} ion, varying its 4f-5d energy level splitting and changing the energy of the electronic transition. This ZPL spectral shift has potential for application in ultra-high density spectral storage.

3) Producing thin films of MgS:Eu,$MgCl_2$, results in significant shifts in spectral position of the spectrum's ZPL. This shifts in very dramatic and results in a spectrum with similar features to the spectrum of MgS:Eu,O reported by previous member of our group. A possible cause for this phenomena is that the high energetic nature of the dynamics of the PLD plume is promoting the reaction of Cl with some of the O^{2-} at the surface of the MgO substrate and subsequently migration towards S^{2-} substitutional sites throughout the thin film lattices. This ZPL spectral shift observed in the MgS:Eu,$MgCl_2$ spectrum has potential for application in ultra-high density spectral storage.

4) Producing thin films of CaS:Eu,$MgCl_2$, results in significant shifts in spectral position of the spectrum's ZPL. This shifts is similar in magnitude to the shift observed on the spectrum of CaS:Eu,O. A possible cause for this phenomenon is that the high energetic nature of the dynamics of the PLD plume is promoting the reaction of Cl with some of the O^{2-} at the surface of the MgO substrate and subsequently migration towards S^{2-} substitutional sites throughout the thin film lattices. The LIFS spectrums obtained from this samples strongly suggest preferential migration as well as long term anisotropic diffusion of the Mg^{2+} ion towards Eu^{2+} lattice sites in the thin films. This phenomena was not observed in microparticles of the same material suggesting that the creation of higher concentrations

of point defects and vacancies in the thin film lattice could have a significant role in the observed changes in the optical spectrum of the material.

5) Doping MgS:Eu with low concentrations of NaCl significantly broadened the Eu optical center ZPL and decreases the Debye-Waller factor of the optical spectrum of the films when compared to un-doped MgS:Eu. This suggest that MgS:Eu's lattice structure is favorable for the diffusion of Na^+ ions and this creates inhomogeneities near Eu^{2+} lattice sites. It is not clear, however, whether the Cl^- ions in NaCl have any effect on the variations of the optical properties observed in this thin films.

6) Doping ZnS with low concentrations of Eu did not result in fluorescence of our samples. This suggests that the energy scheme of the Eu ions inside the ZnS:Eu lattice of thin films made via CCPLD is possibly very similar to the case for ZnS:Eu bulk. The Eu^{2+} excited state transition in particular lies in the in the conduction band and electron recombination does not yield luminescence.

7) The energy gap of ZnS thin films produced via CCPLD was observed to increase with decreasing film thickness. It is not clear whether confinement effects and/or scattering losses play a role in this effect. Changes to the CCPLD parameters used here may be required in future attempts of studying this phenomenon.

8) Although SEM images of ZnS thin films show surface morphologies mostly smooth and uniform, SEM images for ZnS-capped MgS:Eu thin films show a very irregular surface morphology with mounds and even nanogaps throughout the films. This behavior can be attributed to *nodular growth* inherent to the production of CCPLD thin films with low adatom mobility and high ion-bombarment energies.

REFERENCES

[1] R. M. Macfarlane, R. M. Shelby, **Measurement of Nuclear and Electronic Zeeman Effects Using Optical Holeburning Spectroscopy**, *Opt. Lett.*, Vol. 6(2), 96 (1981)

[2] W.E Moerner, **Persistent Spectral Hole-buring: Science and Applications**, Springer-Verlag (1988)

[3] T. W. Mossberg, **Time-domain Frequency-selective Optical Data Storage**, *Opt. Lett.*, Vol. 7(2), 77 (1982)

[4] M.S. Shahriar, P.R. Hemmer, S. Lloyd, P.S. Bhatia and A.E. Craig, **Solid-state Quantum Computer Using Spectral Holes**, *Phys. Rev. A*, Vol. 66, 032301 (2002)

[5] F. M. Schellenberg, W. Lenth, G.C. Bjorklund, **Technological Aspects of Frequency Domain Data Storage Using Persistent Spectral Hole Burning**, *Appl. Optics.*, Vol. 25(18), 3207 (1986)

[6] C.B. Harris, **The Origin of Optical Dephasing Times and Line Shape Functions for Electronic Transitions to Localized and Delocalized States in Solids**, *J. Chem. Phys.*, Vol. 67(12), 5607 (1977)

[7] S. M. Seyeddahmadian, M. F. Aly, L. Biyikli, J. L. Park, M. Solonenko, Z. Hasan, **Inhomogenous Broadening and Gated Holeburning in MgS:Eu and CaS:Eu in Plymethylmethacralate (PMMA)**, *J. Luminescence*, Vol. 83-84, 389 (1999)

[8] Z. Hasan, L. Biyikli, P.I. Macfarlane, **Power-gated spectral holeburning in MgS:Eu^{2+}, Eu^{3+}: A case for high-density persistent spectral holeburning**, *Appl. Phys. Lett.*, Vol. 76(26), 3399 (1998)

[9] Z. Hasan, F. Bezares, J. L. Park, M. Camanell, M. F. Ali, **Fabrication and Spectroscopy of Thin Films for Power-Gated Holeburning**, *Proc. of SPIE*, Vol. 6482, 648204-1 (2007)

[10] S. Asano, Y. Nakao, **Analysis of the Absorption Spectra $4f^{N+1} \rightarrow 4f^N5d$-6s of Rare-earth Ions in the Cubic Field: II. Eu^{2+}Ion in Alkali-earth Chalcogenides**, *J. Phys. C: Solid State Phys.*, Vol. 12, 4095 (1979)

[11] A. A. Kaplyanskii, R. M. Macfarlane, **Spectroscopy of Solids Containing Rare Earth Ions**, *North-Holland Physics Publishing*, (1987)

[12] G. Liu, B. Jacquier, **Spectroscopic Properties of Rare Earths in Optical Materials**, *Springer*, (2005)

[13] B. Henderson, G.F. Imbusch, **Optical Spectroscopy of Inorganic Solids**, *Oxford Science Publications*, (1989)

[14] A. Konjhodzic, A. Adamczyk, F. Vagizov, Z. Hasan, E. E. Alp, W. Sturhahn, J. Zhao, J. J. Carroll, **Nuclear Forward Scattering vs. Conventional**

Mössbauer Studies of Atomically Tailored Eu-based Materials, *Hyperfine Interactions*, Vol. 170(1-3), 83 (2006)

[15] O. Sild, Kristjan Haller, **Zero-Phonon Lines and Spectral Hole Burning in SPectroscopy and Photochemistry**, *Springer-Verlag*, (1988)

[16] T.H. Keil, **Shapes of Impurity Absorption Bands in Solids**, *Phys. Rev.*, Vol. 140(2A), A601 (1965)

[17] M. Lax, **The Frank-Condon Principle and its Application to Crystals**, *J. Chem. Phys.*, Vol. 20, 1752 (1952)

[18] E. T. Copson, **Functions of a Complex Variable**, *Oxford University Press*, (1935)

[19] Mohamed F. Aly, **Fabrication and Characterization of Rare Earth Doped Wide Bandgap Semiconductors for Spectral Storage**, *PhD Thesis, 2006*

[20] Aras Konjhodzic, **Nanopatternig and Synchrotron Radiation Driven Mössbauer Spectroscopy of Rare Earth Doped Wide Bandgap Semiconductors Materials**, *PhD Thesis, 2007*

[21] Mikhail Solonenko, **Persistent Spectral Holeburning in Europium and Europium, Samarium Doped Calcium Sulfide**, *PhD Thesis, 1999*

[22] D. B. Chrisey, G. K. Hubler, **Pulsed Laser Deposition of Thin Films**, *Wiley-Interscience*, (1994)

[23] D. Poelman, R. Vercaemst, F. Cardon, **Influence of the Growth Conditions on Properties of CaS:Eu Electroluminescent Thin Films**, *J. Luminescence*, Vol. 75, 175 (1997)

[24] R. W. G. Wyckoff, **Crystal Structure Vol. 1**, *Wiley*, (1963)

[25] M. Mclaughlin, H. F. Sakeek, P. Maguire, W. G. Graham, J. Anderson, **Properties of Thin Films Prepared by 248-nm Pulsed Laser Deposition**, *Appl. Phys. Lett.*, Vol. 63, 1865 (1993)

[26] Y. Nakao, **Luminescence Centers of MgS, CaS and CaSe Phosphors Activated with Eu^{2+}Ions**, *J. Phys. Soc. Japan*, Vol. 48(2), 534 (1980)

[27] Z. Hasan, M. Solonenko, P. I. Macfarlane, and L. Biyikli, **Persistent High Density Spectral Holeburning in CaS:Eu and CaS:Eu,Sm Phosphors**, *Appl. Phys. Lett.*, Vol. 72(19), 2373 (1998)

[28] D. J. Chadi, **Acceptor and donor states of impurities in wide band gap II-VI semiconductors**, *J. Crystal Growth*, Vol. 138, 295 (1994)

[29] C.P. Flynn, **Point Defects and Diffusion**, *Oxford University Press*, (1967)

[30] V. Consonni, G. Feuillet, **Correlated Structural Reordering and Dopant Redistribution in Annealed Polycrystalline CdTe**, *J. Appl. Phys.*, Vol. 105, 083535 (2009)

[31] K. Swiatek, M. Godlewski, D. Hommel, **Deep Europium-bound Exciton in a ZnS Lattice**, *Phys. Rev. B*, Vol. 42(6), 3628 (1990)

[32] L. Shu-man, G. Hai-Qing, Z. Zhi-Hua, L. Feng-Qi, W. Zhang-Guo, **Photoluminescence of Eu^{2+}-doped ZnS Nanocrystals**, *Chin. Phys. Lett.*, Vol. 17(8), 609 (2000)

[33] B. Cheng, Z. Wang, **Synthesis and Optical Properties of Europium-doped ZnS: Long-lasting Phosphorescence from Aligned Nanowires**, *Adv. Func. Mater.*, Vol. 15, 1883 (2005)

[34] E.W. Chase, R.T. Hepplewhite, D.C Krupta, D. Khang, **Electroluminescence of ZnS Lumocen Devices Containing Rare-Earth and Transition Metal Fluorides**, *J. Appl. Phys.*, Vol. 40(6), 2512 (1969)

[35] D.C. Krupta, D.M. Mahoney, **Electroluminescence and Photoluminescence of Thin Films of ZnS doped with Rare-Earth Metals**, *J. Appl. Phys.*, Vol. 43(5), 2314 (1972)

[36] D.T. Pierce, W.E. Spiecer, **Electronic Structure of Amorphous Si from Photoemission and Optical Studies**, *Phys. Rev. B*, Vol. 5, 3017 (1972)

[37] D. L. Wood, J. Tauc, **Weak Absorption Tails in Amorphous Semiconductors**, *Phys. Rev. B*, Vol. 5(8), 3144 (1972)

[38] W. M. Yen, **Laser Spectroscopy of Solids II**, *Springer-Verlag*, (1989)

[39] S. Adachi, **Optical Properties of Crystalline and Amorphous Semiconductors**, *Kluwer Academic Publishers*, (1999)

[40] S. Varghese, M. Iype, E. J. Mathew, C. S. Menon, **Determination of the Energy Band Gap of Thin Films of Cadmium Sulphide,Copper Ph-**

thalocyanine and Hybrid Cadmium Sulphide/ Copper Phthalocyanine from its Optical Studies, *Mat. Lett.*, Vol. 56, 1078 (2002)

[41] J. P. Borah, K. C. Sarma, **Optical and Optoelectronic Properties of ZnS Nanostructured Thin Films**, *Acta Physica Polonica A*, Vol. 114(4), 713 (2008)

[42] E. E. Khawaja, C. A. Hogarth, **The Optical Absorption Edge in Some Semiconductors**, *J. Phys. C: Solid State Phys.*, Vol. 21, 607 (1988)

[43] R. S. Longhurst, **Geometrical and Physical Optics**, *John Wiley & Sons Inc*, (1967)

[44] M. K. Morozova, I.A. Karetnikov, K. V. Golub, E. M. Gavrishchuk, E. V. Yashina, V. G. Plotnichenko, V. G. Galstyan, **Pressure and Temperature Effects on Point-Defect Equilibria and Band Gap of ZnS**, *Inorganic Materials*, Vol. 40(11), 1138 (2004)

[45] V.B. Sandomirskii, **Dependance of the Forbidden-Band Width of Semiconducting Films on their Thicknesses and Temperature**, *J. Exptl. Theoret. Phys.*, Vol. 43, 2309 (1962)

[46] R. Hill, D. Richardson, **Quantum Mechanical Broadening of Optical Absorption in Thin Film Semiconductors**, *Thin Solid Films*, Vol. 16, S3 (1973)

[47] T. Guang-Lei, H. E. Hong-Bo, S. Jian-Da, **Effects of Microstructure of TiO_2 Thin Films on Optical Band Gap Energy**, *Chin. Phys. Lett.*, Vol. 22(7), 1787 (2005)

[48] F. Antoni, C. Fuchs, E. Fogarassy, **Analytical Description of the Film Thickness Distribution Obtained by the Pulsed Laser Ablation of a Mono-Atomic Target: Application to Silicon and Germanium**, *Appl. Surf. Sci*, Vol. 96-98, 50 (1996)

[49] D. Kashchiev, **Growth Kinetics of Dislocation-free Interfaces and Growth Mode of Thin Films**, *J. Crystal Growth*, Vol. 40, 29 (1977)

[50] S. Metev, K. Meteva, **Nucleation and Growth of Laser-plasma Deposited Thin Films**, *Appl. Surf. Sci.*, Vol. 43, 402 (1989)

[51] R. Messier, **The Nano-world of Thin Films**, *J. Nanophotonics*, Vol. 2, 021995 (2008)

BIBLIOGRAPHY

[1] Antoni, F., Fuchs C. and Forgarassy, E., **Analytical Description of the Film Thickness Distribution Obtained by the Pulsed Laser Ablation of a Monoatomic Target: Application to Silicon and Germanium**, *Appl. Surf. Sci.*, Vol. 96-98, 50 (1996)

[2] Babbitt, W. R. and Mossberg, T. W., **Time-domain Frequency-selective Optical Data Storage in a Solid-state Material**, *Opt. Commun.*, Vol. 65(3), 185 (1988)

[3] Blasse, G. and Grabmaier, B.C., **Luminescent Materials**, *Springer-Verlag*, (1994)

[4] Blasse, G., **Luminescence of Inorganic Solid**, *Plenum Press*, (1974)

[5] Bloembergen, N., **The Solved Puzzle of Two-Photon Rare-earth Spectra in Solids**, *J. Lumin.*, Vol. 31-32, 23 (1984)

[6] Chrisey, Douglas B., **Pulsed Laser Deposition of Thin Films**, *John Wiley & Sons, Inc.*, (1994)

[7] Duffey, George H., **Applied Group Theory for Physicists and Chemists**, *Prentice-Hall* (1992)

[8] Eason, Robert, **Pulsed Laser Deposition of Thin Films: Application-Led Growth of Functional Materials**, *Wiley-Interscience* (2007)

[9] Freiser, M. J., Methfessel, S. and Holtzberg, F., **Multiplet Structure in the Absorption Spectrum of Eu^{2+}**, *J. Appl. Phys.*, Vol. 39(2), 900 (1968)

[10] Fukada, H., Sakurai, D., Tokuda, N., Ohmi, K., Tanaka, S., Kobayashi, H. and Takahashi, M., **Effect of Thermally Decomposed H_2S Supply on Electroluminescent Characteristics of Hybrid Devices Having Thick BaTiO3 Dielectric and Thin SrS:Ce Phosphor Films**, *Jpn. J. Appl. Phys.*, Vol. 41, 2150 (2002)

[11] Gorokhovskii, A. A., Kaarli, R. K., and Rebane, L.A., **Holeburning in the Contour of a Pure Electronic Line of a Shpol'skii System**, *JETP Lett.*, Vol. 20, 216 (1974)

[12] Henderson, B. and Imbush, G. F., **Optical Spectroscopy of Inorganic Solids**, *Oxford Science Publications*, (1989)

[13] Huffner, S., **Optical Spectra of Transparent Rare Earth Compunds**, *Academic Press, Inc.*, (1978)

[14] Jia, D., Jia, W., Evans, D. R., Dennis, W. M., Liu, H., Zhu, J. and Yen, W. M., **Trapping Processes in CaS:Eu^{2+},Tm^{3+}**, *J. Appl. Phys.*, Vol. 88(6), 3402 (2000)

[15] Kaplyanskii, A. A., **Spectroscopy of Solids Containing Rare Earth Ions**, *North-Holland*, (1987)

[16] Kharlamov, B. M., Personov, R.I. and Bykovskaya, L. A., **Stable Gap in Absorption Spectra of Solid Solutions of Organic Molecules by Laser Irradiation**, *Opt. Commun.*, Vol. 12, 191 (1974)

[17] Kobayashi, H., Tanaka, S., Sasakura, H. and Hamakawa, Y., **Excitation Mechanism of Electroluminescent ZnS Thin Films Doped with Rare-earth Ions**, *Jpn. J. Appl. Phys.*, Vol. 13(7), 1110 (1974)

[18] Lehmann, Willi, **Activators and Co-activators in Calcium Sulfide Phosphors**, *J. Lumin.*, Vol. 5, 87 (1972)

[19] Macfarlane, R. M. and Shelby, R. M., **Homogeneous Line Broadening of Optical Transitions of Ions and Molecules in Glasses**, *J. Lumin.*, Vol. 36, 179 (1987)

[20] Rao, R. P., **Cathodoluminescence in MgS:RE Phosphors**, *J. Electrochem. Soc.*, Vol. 132(8), 2033 (1985)

[21] Renn, Alois and Wild, Urs P., **Spectral Hole Burning and Hologram Data Storage**, *Appl. Opt.*, Vol. 26(19), 4040 (1987)

[22] Rubio, J., **Doubly-valent Rare-earth ions in Halide Crystals**, *J. Phys. Chem. Solids*, Vol. 52(1), 101 (1991)

[23] Shishkov, Milen S., **Electro-Optical Properties of III-IV Multiple Quantum Well Structures for Light Modulation at Visible Wavelengths**, *PhD Thesis, 1999*

[24] Swiatek, K., Godlewski, M., Niinistö, L. and Leskelä, M., **Optical Recombination Mechanism in Eu^{2+}-doped CaS and SrS Thin Films**, *J. Appl. Phys.*, Vol. 74(5), 3442 (1993)

[25] Szabo, A., **US Patent 3,896,420**, (1975)

[26] Wherrett, Brian S., **Group Theory for Atoms, Molecules and Solids**, *Prentice-Hall International*, (1986)

[27] Tanaka, S., Yoshiyama, H., Nakamura, K., Wada, S., Morita, K. and Kobayashi, H., **Photo-induced Transferred Charge in Rare-earth-doped Alkaline-earth Sulfide Electroluminescent Thin Films**, *Jpn. J. Appl. Phys.*, Vol. 30(6A), L1021 (1991)

[28] Warkentin, M., Bidges, F., Carter, S. and Anderson, M., **Electroluminescence Materials ZnS:Cu,Cl and ZnS:Cu,Mn,Cl Studied by EXAFS Spectroscopy**, *Phys. Rev. B*, Vol. 75, 075301 (2007)